UCLouvain

epl

École polytechnique de Louvain

Influence of PLA thermoplastic nanocomposite on bio-sourced epoxy resin's mechanical properties

Author: **Camille WAGNER**
Supervisor: **Christian BAILLY**
Readers: **Thomas PARDOEN, Bernard NYSTEN**
Academic year 2019–2020
Master [120] in Chemical and Materials Engineering

Acknowledgments

First of all, I would like to thank the people who made this work possible.

To begin with, I would like to thank Professor Christian Bailly, the supervisor of this paper, for welcoming me to his team and making this work possible.

I would particularly like to thank Mr. Wael Ballout and Mr. Pascal Van Velthem, who have greatly helped me in the achievement of this master thesis. I would like to thank them for the time they devoted to this work, their guidance, support and advices which were invaluable.

I would like to thank Mr Vincent Destoop for his availability and help with the tensile test machine. Many thanks also to Mrs. Colette Douchamps for the preparation of SEM samples and SEM pictures. I thank Mr. Rajendar Nutenki for his help with injection moulding and for sharing its results on PLA/Flax and PHBV/Flax blends. Thanks also to Mr. Martial Kuete for his help during processing.

Finally, I would like to thank my family and friends who supported me during the achievement of my research work.

Abstract

Composites have many noteworthy properties and epoxy resins are widely used as matrices enabling them to be essential in many fields of activity such as aerospace, automobile, electronic and painting industry. However due to high cross-linking density, epoxy resin are intrinsically brittle and notch sensitive limiting their use. In addition, most of petrochemical epoxy resins use derivatives of bisphenol A (BPA) which has highly negative health effects [1]. This is why engineers try to replace those petroleum-based composites by bio-sourced ones.

The aim of the work is to study the influence of the addition of thermoplastic nanocomposite in bio-sourced epoxy resin. Semicrystalline and amorphous poly-lactic acid (PLA) based composites with different loading rate of lignin particles are studied. Morphological, thermal and mechanical properties are highlighted thanks to a number of analysis and tests including scanning electron microscopy (SEM), differential scanning calorimetry (DSC), thermogravimetry analysis (TGA), dynamical mechanical analysis (DMA) and tensile test.

PLA/Lignin nanocomposite can be a good candidate to toughen bio-sourced epoxy resin. Indeed, DMA analysis reveals a significant increase of the storage modulus $E^{'}$ with the addition of lignin for both semi-crystalline and amorphous PLA. In addition, tensile test shows an increase in stiffness E_t when the content of lignin in the blend increases however at the same time the maximum strength σ_{max} and the strain at break ε_b decrease significantly. Above $20wt\%$ of lignin, the decrease of those mechanical properties becomes detrimental compare to the profit of the stiffness' increase.
Though glass transition temperature T_g decreases slightly with lignin addition and melting temperature T_m of semi-crystalline PLA is also slightly lowered with lignin addition which is indicative of the existence of a intermolecular interaction between PLA and lignin. Potential lignin agglomerates of different sizes in amorphous PLA/Lignin blends are observed suggesting that the manual mixing and the extrusion do not allow to blend at molecular level the two components.

Contents

1 General Introduction **0**

2 Bibliographic review **2**
2.1 Theory . . . 2
2.1.1 Polylactic acid (PLA) . . . 2
2.1.1.1 Synthesis of PLA and structural composition . . . 3
2.1.1.2 Properties of PLA . . . 5
2.1.1.2.1 Crystallisation . . . 7
2.1.1.2.2 Thermal properties . . . 10
2.1.1.2.3 Physical and Mechanical properties . . . 13
2.1.2 Lignin . . . 14
2.1.2.1 Lignin synthesis . . . 15
2.1.2.2 Types of lignin . . . 17
2.1.2.2.1 Lignosulfonates . . . 17
2.1.2.2.2 Kraft lignin . . . 17
2.1.2.2.3 Soda lignin . . . 17
2.1.2.2.4 Organosolv lignin . . . 18
2.1.2.3 Lignin-based carbon fibres . . . 18
2.1.2.4 Thermal stability of lignin . . . 18
2.1.3 Flax Fibres . . . 20
2.1.3.1 Structure and composition of flax fibre . . . 20
2.1.3.2 Characteristics and properties of flax fibre . . . 21
2.1.4 Epoxy resin . . . 22
2.1.4.1 Properties of epoxy resin . . . 22

2.1.4.2 Crosslinking agent (hardener) . . . 23
2.1.4.3 Curing mechanism/reaction . . . 23
2.1.4.4 TTT diagram . . . 25
2.1.4.5 Bio-sourced resin . . . 27
2.1.4.6 Bio-sourced epoxy resin . . . 27
2.1.4.7 Bio-sourced curing agent . . . 30
2.1.5 Thermodynamics of polymer blends . . . 31
2.1.5.1 Miscibility conditions . . . 32
2.1.5.2 Enthalpy and Entropy of mixing . . . 33
2.1.5.3 Phase diagrams thermoplastic - thermoset (TP-TS) 35
2.1.6 Phase separation and Morphology . . . 38
2.1.6.1 Phase separation mechanisms . . . 38
2.1.6.2 Morphology . . . 40
2.1.7 Thermal and mechanical properties of polymer blends . . . 40
2.1.7.1 Transition glass temperature . . . 40
2.1.7.2 Measurement methods of transition glass temperature 41
2.1.8 Polymer blends . . . 42
2.1.9 Mechanical properties and Fracture mechanics . . . 44
2.1.9.1 Mechanical characteristics from tensile test . . . 44
2.1.9.2 Fracture mechanics . . . 49
2.1.9.2.1 Stress intensity factor K . . . 50
2.1.9.2.2 Energy restitution rate G . . . 51
2.1.9.2.3 Toughness K_{IC} and G_{IC} . . . 51
2.1.9.2.4 Measurement of toughness . . . 52
2.2 Literature review . . . 54
2.2.1 Thermoplastic nanocomposites . . . 54
2.2.1.1 PLA-based nanocomposites . . . 55
2.2.1.1.1 Silica/PLA nanocomposites . . . 55
2.2.1.1.2 Cellulose/PLA nanocomposites . . . 56
2.2.1.2 Lignin-Modified Polyester Materials . . . 56
2.2.1.2.1 Lignin/PCL nanocomposites . . . 56

2.2.1.2.2 Lignin/PHB and Lignin/PET nanocomposites . . . 57
2.2.1.2.3 Lignin incorporation in PLA matix . . . 58
2.2.2 Improvement of epoxy resin with thermoplastic . . . 61
2.2.2.1 Toughening mechanisms . . . 61
2.2.2.2 Thermoplastic-modified epoxy . . . 65
2.2.2.3 Morphology of TS - TP with nanofillers . . . 66
2.2.2.3.1 Nanoparticle distribution in TS/TP nanocomposites . . . 68

3 Experimental part **71**
3.1 Materials . . . 71
3.1.1 Thermoplastics: PLA . . . 71
3.1.2 Charges . . . 72
3.1.2.1 Lignin . . . 72
3.1.2.2 Flax fibres . . . 72
3.1.3 Thermoset system . . . 73
3.1.3.1 InfuGreen 810 resin . . . 73
3.1.3.2 SD 4771 hardener . . . 73
3.2 Samples preparation and processing . . . 74
3.2.1 Drying . . . 74
3.2.2 Extrusion of thermoplastics . . . 74
3.2.3 Injection moulding . . . 76
3.2.4 Epoxy resin - thermoplastic blends preparation . . . 79
3.3 Characterisation techniques . . . 80
3.3.1 Differential Scanning Calorimetry (DSC) . . . 80
3.3.2 Thermogravimetric analysis (TGA) . . . 83
3.3.3 Scanning Electron Microscopy (SEM) . . . 85
3.3.4 Tensile Test . . . 86
3.3.5 Dynamic Mechanical analysis (DMA) . . . 87
3.3.6 Three-point flexural test . . . 89

4 Results and discussion **90**
4.1 Characterisation of thermoplastic nanocomposites . . . 90
4.1.1 Thermal characterisation (DSC and TGA analysis) . . . 90
4.1.1.1 DSC Analysis . . . 90

4.1.1.1.1 Semicrystalline PLA (PLA2500HP) - Lignin nanocomposites . . . 92
4.1.1.1.2 Amorphous PLA (PLA4060D) - Lignin nanocomposites . . . 95
4.1.1.1.3 Semicrystalline PLA (PLA2500HP) - Flax nanocomposites . . . 98
4.1.1.1.4 PHBV - Flax nanocomposites . . . 101
4.1.1.2 TGA Analysis . . . 104
4.1.2 Mechanical characterisation . . . 108
4.1.2.1 Tensile Test . . . 108
4.1.2.1.1 PLA2500HP and PLA4060D - Flax blends . . . 116
4.1.3 Dynamical mechanical analysis . . . 118
4.1.3.0.1 PLA - Lignin nanocomposites . . . 118
4.1.3.0.2 PLA semicrystalline (PLA2500HP) - Flax nanocomposites . . . 120
4.1.3.0.3 PHBV - Flax nanocomposites . . . 121
4.1.3.0.4 Comparison of T_g measured by DSC and DMA . . . 122
4.1.3.0.5 Comparison of E measured by tensile test and DMA . . . 124
4.1.4 Dispersion analysis . . . 126

5 Conclusion and Perspectives 130

6 Appendix 1: Additional graphs 135

List of Tables

2.1 Unit cell's parameters of PLA crystalline structure [2]. 10
2.2 Transition temperatures of selected PLA copolymer [3]. 11
2.3 Effects of stereochemistry and crystallinity on mechanical properties [4]. 14
2.4 Physical properties of PLA [4]. 14
2.5 Lignin fibre's properties [5]. 18
2.6 Flax fibre's properties [6]. 21
2.7 Mechanical properties of PLLA and the blends with lignin [7]. . . . 60

3.1 Properties of *Ingeo^{TM} Biopolymer 2500HP* (PLA) [8]. 72
3.2 Properties of *Ingeo^{TM} Biopolymer 4060D* (PLA) [9]. 72
3.3 Properties of *Protobind^{TM} 1000* lignin. 72
3.4 Properties of *SR InfuGreen 810* resin [10]. 73
3.5 Properties of *SD 4771* hardener [10]. 74
3.6 Extrusion parameters for PLA 2500HP pure and blends with lignin. 76
3.7 Extrusion parameters for PLA 4060D pure and blends with lignin. . 76
3.8 Injection Moulding parameters for PLA 2500HP pure and blends with lignin. 78
3.9 Injection Moulding parameters for PLA 4060D pure and blends with lignin. 78
3.10 Curing cycle parameters for epoxy resin, epoxy resin/PLA and epoxy resin/Lignin blends. 80

4.1 DSC results of First scan of PLA 2500HP - Lignin blends. T^* is the temperature of the exothermic peak before melting and $\Delta H_m^0 = -93.7\,[J/g]$ is the melting enthalpy of a completely (100%) crystalline PLA [3, 11]. 93
4.2 DSC results of PLA 2500HP - Lignin blends from Cooling and Second heating. 94
4.3 DSC results for PLA4060D - Lignin blends. 96
4.4 DSC results of PLA 2500HP - Flax blends from Cooling and First heating. 100

4.5 DSC results of PLA 2500HP - Flax blends from Second heating. . . 101
4.6 DSC results of PHBV - Flax blends from Cooling and Second heating. 103
4.7 DSC results of PHBV - Flax blends from First heating. 104
4.8 TGA results of PLA2500HP - Lignin blends. 107
4.9 TGA results of PLA4060D - Lignin blends. 107
4.10 Tensile test results for PLA semi-crystalline 2500HP - Lignin blends. 113
4.11 Tensile test results for PLA amorphous 4060D - Lignin blends. . . . 114
4.12 Tensile test results for PLA semi-crystalline 2500HP - Flax blends. . 116
4.13 Tensile test results for PLA amorphous 4060D - Flax blends. 116
4.14 DMA results for PLA semi-crystalline 2500HP - Lignin blends. . . . 118
4.15 DMA results for PLA amorphous 4060D - Lignin blends. 119
4.16 DMA results for PLA semicrystalline 2500HP - Flax blends. 120
4.17 DMA results for PHBV - Flax blends. 121
4.18 Comparison of T_g from DSC and DMA analysis for PLA2500HP - Lignin blends. 123
4.19 Comparison of T_g from DSC and DMA analysis for PLA4060D - Lignin blends. 123
4.20 Comparison of E from tensile test and DMA analysis for PLA2500HP - Lignin blends. 124
4.21 Comparison of E from tensile test and DMA analysis for PLA4060D - Lignin blends. 125
4.22 Comparison of E_t with Voigt and Reuss models for PLA2500HP - Lignin blends. 126
4.23 Comparison of E_t with Voigt and Reuss models for PLA4060D - Lignin blends. 126

List of Figures

2.1 Illustration of the two lactic acid enantiomers : L-lactic acid and D-lactic acid. 3
2.2 Synthesis routes of PLA [3, 11]. 4
2.3 Illustration of the three lactide stereoisomers. 5
2.4 Carbon footprint and water usage of oil-based polymers (red points) and biopolymers (green points) [12]. 6
2.5 Embodied energy of oil-based polymers (red points) and biopolymers (green points) [12]. 6
2.6 DSC scans of water quenched, air-annealed (cooled from 220[$^{\circ}C$] to ambient temperature in 5 minutes, quenching), and full-annealed (cooled from 220$^{\circ}C$ to ambient temperature in 105 minutes, slow cooling) PLLA samples. The scans were performed at a heating rate of 10[$^{\circ}C/min$] [3]. 7
2.7 DSC scans at 20[K/min] for PLA with 1.5% (PLA-L), 8.1% (PLA-M), and 16.4% (PLA-H) D-isomers. All samples were cooled quickly from the melt and isothermally crystallized at 145[$^{\circ}C$] for 15 hours. The quenched PLLA sample did not undergo the 15 hours isothermal crystallisation [3]. 8
2.8 DSC scans for 1.5% D-lactide PLA samples cooled from the melt at 10[K/min] and then reheated at different heating rates from 30 to 0.3[K/min] [3]. 8
2.9 Young$'$s modulus E and density ρ of commodity oil-based polymers (red points) and biopolymers (green points), with contours of $\frac{E}{\rho}$ [12]. 13
2.10 Tensile strength and density ρ of commodity oil-based polymers (red points) and biopolymers (green points), with contours of $\frac{\sigma_t}{\rho}$ [12]. . . 13
2.11 Structure of Lignocellulosic Biomass [13]. 15
2.12 Chemical structures of hydroxycinnamyl alcohol monomers [14]. . . 16
2.13 Presumed structure of lignin of conifers [15]. 16
2.14 Pyrolysis curves of hemicellulose, cellulose and lignin in TGA [16]. . 19
2.15 Structure of an elementary flax fibre [17]. 20
2.16 Chemical structure of end epoxy group [18]. 22

2.17 Bidimensionnal scheme of the curing of thermosetting resin. (a) unreacted components; (b) linear growth and chain branching; (c) gel formation; (d) fully crosslinked material [19]. 24
2.18 Chemical reactions taking place during curing [19]. 25
2.19 TTT diagram, showing the states of the polymer and the critical temperatures: T_{g0} the initial glass transition temperature, $T_{g(gel)}$ the intersection between vitrification and gelation and $T_{g\infty}$ the maximum glass transition achievable [19]. 26
2.20 Structure of a typical triglyceride molecule [20]. 27
2.21 Representative structures of linseed oil [21]. 28
2.22 Structures of D-isosorbide and its epoxidized form DGEDAS [21]. . 29
2.23 Cardanol is a derivative of cash nut shell liquid. 30
2.24 Structures of curing agents: diethylenetriamine (DTA) known to be toxic; diaminodiphenylsulfone (DDS); D-lysinol; methylenedianiline known to be toxic; tetrahydrophthalic anhydride (THPA); and tannic acid which is a natural polyphenol [21]. 31
2.25 Evolution of g_v^0 and g_v as a function of the volume fraction of one of the component [22]. 32
2.26 Positive curvature case - $\Delta g_{v,m}$ as a function of the volume fraction of one of the constituents [22]. 33
2.27 Negative curvature case - $\Delta g_{v,m}$ as a function of the volume fraction of one of the constituents [22]. 33
2.28 Representation of possible configurations for (a) small molecules and (b) macromolecules [22]. 34
2.29 (a) Evolution of the free energy of mixing with the temperature when $\chi_{12,enthalpic} < 0$. (b) Temperature - composition diagram when $\chi_{12,enthalpic} < 0$ [22]. 36
2.30 (a) Evolution of the free energy of mixing with the temperature when $\chi_{12,enthalpic} > 0$. (b) Temperature - composition diagram when $\chi_{12,enthalpic} > 0$ [22]. 36
2.31 Temperature-composition diagram when $\chi_{12,enthalpic} >> 0$ [22]. . . . 37
2.32 Evolution with the crosslinking rate α of temperature-composition diagram in the case of TP-TS blend (a) for a LCST behaviour and (b) for a UCST behaviour [22]. 38
2.33 Different morphologies for a binary polymer blend [22]. 38
2.34 Compositions evolution during demixing by nucleation and growth [22]. 39
2.35 Compositions evolution during demixing by spinodal decomposition [22]. 39

2.36 Illustration of the increase of "compositional contrast" during spinodal decomposition [22]. 40
2.37 Representation of the glass transition temperature in the case of (a) a miscible blend (b) a partially miscible blend (c) an immiscible blend [22]. 43
2.38 Evolution of the glass transition temperature of a partially miscible blend as a function of the composition [22]. 44
2.39 Typical tensile specimen, showing a reduced gauge section and enlarged shoulders [23]. 45
2.40 Tensile true stress-strain ($\sigma - \varepsilon$) curves for typical plastics [24]. . . 46
2.41 Stress-whitening phenomena for a bar of (a) P-E block copolymer and (b) 80/20 PP/PE blend [25]. 48
2.42 Dependence of mechanical response of polymers on the external conditions [26]. 48
2.43 Definition of axis around a crack in LEFM. 49
2.44 Definition of the three modes of crack opening [27]. 50
2.45 Geometry of a SENB specimen [28]. 52
2.46 Force-displacement curve obtained with a three-points bending test on a SENB specimen [28]. 53
2.47 DSC second heating scans of PCL and its blends with various lignin content (prepared by mechanical mixing). Amplification of the area near T_g on left side [29]. 57
2.48 DSC second heating scans of PLLA and its blends with various lignin contents. The samples have been aged at $80°C$ for more than 2 weeks [7]. 59
2.49 TGA curves of (A) PLLA and its blends with various lignin contents and of (B) lignin [7]. 61
2.50 Shematic representation of toughening mechanisms for thermoplastic-modified epoxy resins: (1) crack pinning, (2) particle bridging, (3) crack path deflection, (4) particle yielding, (5) particle-yielding-induced shear banding and (6) microcracking [30]. 62
2.51 Scheme of crack pinning [31]. 63
2.52 SEM picture of fracture surface of a thermoplastic modified resin with crack pinning [32]. 63
2.53 Scheme of crack bridging [33]. 64
2.54 SEM picture of fracture surface of a thermoplastic modified resin with crack bridging [32]. 64
2.55 Scheme of crack path deflection [33]. 64
2.56 SEM picture of fracture surface of a thermoplastic modified resin with crack path deflection [32]. 64

2.57 Illustration of (a) the spinodal decomposition (SD) and (b) the nucleus growth (NG) mechanisms in an epoxy/thermoplastic binary system [34]. 67
2.58 Illustration of possible nanoparticle distribution situation in TS/TP blend nanocomposites: nanofillers located (i) and (ii) in one of the polymer phase, (iii) at the interface between them [34]. 68
2.59 TEM images of PA12/EA blend with 1.8$wt\%$ carbon nanotubes, obtained by premixing CNTs with EA next blending with PA12 [35]. 69
2.60 TEM picture of epoxy resin/PKHH (5%) with CSRs [36]. 70
2.61 TEM picture of epoxy resin/PKHH (10%) with CSRs [36]. 70

3.1 Vacuum pump chamber used for drying. 74
3.2 Typical geometries of a screw for single-screw extruder [3]. 75
3.3 Picture of the *Thermo Scientific Process 11 Twin-screw Extruder* used. 76
3.4 Picture of the *VariCut Pelletizer* used. 77
3.5 Picture of the *Thermo Scientific^{TM} HAAKE^{TM} MiniJet Pro* used. . 77
3.6 Schematic representation of the mould used. 77
3.7 Curing cycle applied for resin/PLA blends. 79
3.8 Schematic principle of a DSC. 1 - Furnace lid; 2 - Crucible on the DSC Sensor; 3 - Silver furnace; 4 - Pt100 temperature sensor of furnace; 5 - Flat heater between two insulating disks; 6 - Thermal resistance for cooler; 7 - Cooling flange; 8 - Compression spring construction; 9 - Cooling flange Pt100; 10 - DSC raw signal for amplifier; 11 - Purge gas inlet; 12 - Dry gas inlet [37]. 81
3.9 Method applied to each sample for the DSC analysis. 82
3.10 Schematic principle of TGA. 1 - Gas outlet; 2 - Furnace heater; 3 - Sample support; 4 - Reactive gas capillary; 5 - Baffles; 6 - Parallel-guided ultramicro balance; 7 - Thermostated balance chamber; 8 - Protective gas inlet; 9 - Reactive gas inlet; 10 - Purge gas inlet; 11 - Motor for opening sample chamber; 12 - Cooling circuit; 13 - Furnace temperature sensor [38]. 83
3.11 Method applied to each sample for the TGA analysis. 84
3.12 Generalised illustration of interaction volumes for various electron-specimen interactions [39]. 85
3.13 Tensile bar ISO527-2-5A (measurements in mm). 86
3.14 Scheme of Dynamic Mechanical Analysis (DMA). 1 - 4-axis alignment; 2 - Force sensor (piezoelectric); 3 - Displacement sensor (LVDT); 4 - Clamping assembly and sample holder; 5 - Furnace; 6 - Drive motor; 7 - Z-axis table [40]. 88

3.15 Zoom on the measuring head (elongation) of Dynamic mechanical analyzer (Mettler-Toledo) [41]. 88
3.16 Method applied for the DMA analysis for each (a) PLA2500HP (+ Lignin) (b) for PLA4060D (+ Lignin). 89

4.1 DSC scan of PLA 2500HP semicrystalline neat extruded and identification of the different peaks. 91
4.2 DSC Cooling heating scans curves of PLA 2500HP - Lignin blends. 94
4.3 DSC First heating scans curves of PLA 2500HP - Lignin blends. . . 95
4.4 DSC Second heating scans curves of PLA 2500HP - Lignin blends. . 95
4.5 DSC Cooling heating scans curves of PLA 4060D - Lignin blends. . 97
4.6 DSC First heating scans curves of PLA 4060D - Lignin blends. . . . 97
4.7 DSC Second heating scans curves of PLA 4060D - Lignin blends. . . 98
4.8 DSC Cooling scans of PLA 2500HP - Flax blends with different weight percentage realised by *Rajendar Nutenki*. 99
4.9 DSC First heating scans of PLA 2500HP - Flax blends with different weight percentage realised by *Rajendar Nutenki*. 100
4.10 DSC Second heating scans of PLA 2500HP - Flax blends with different weight percentage realised by *Rajendar Nutenki*. 101
4.11 DSC Cooling scans of PHBV - Flax blends with different weight percentage realised by *Rajendar Nutenki*. 102
4.12 DSC First heating scans of PHBV - Flax blends with different weight percentage realised by *Rajendar Nutenki*. 103
4.13 DSC Second heating scans of PHBV - Flax blends with different weight percentage realised by *Rajendar Nutenki*. 104
4.14 TGA curve of pure lignin. 105
4.15 TGA curves of PLA 2500HP - Lignin blends. 106
4.16 TGA curves of PLA 4060D - Lignin blends. 108
4.17 Brittle fracture in thermoplastics [42]. 109
4.18 Cold-drawing of a linear polymer [42]. 110
4.19 Schematic description of the true stress[Pleaseinsertintopreamble]strain relationship of semi-crystalline polymers and the evolution of microstructure [43]. 111
4.20 Crazing in a linear polymer [42]. 112
4.21 Stress-strain curves of the different PLA2500HP - Lignin blends drawn with Matlab illustrating the evolution of the mechanical properties. Curves have been deliberately shifted by 0.001 to the right with respect to each other to compare them easily. 114

4.22 Stress-strain curves of the different PLA4060D - Lignin blends drawn with Matlab illustrating the evolution of the mechanical properties. Curves have been deliberately shifted by 0.001 to the right with respect to each other to compare them easily. 115
4.23 Stress-strain curves for PLA2500HP - 5wt%Flax blend. 117
4.24 Stress-strain curves for PLA2500HP - 10wt%Flax blend. 117
4.25 Stress-strain curves for PLA4060D - 5wt%Flax blend. 117
4.26 Stress-strain curves for PLA4060D - 10wt%Flax blend. 117
4.27 DMA curves of PLA 2500HP - Lignin blends. 119
4.28 DMA results for PLA 4060D - Lignin blends. 120
4.29 DMA results for PLA2500HP - Flax blends. 121
4.30 DMA results for PHBV - Flax blends. 122
4.31 Drawing of a 2D projection of a spherulite formed from radially grown lamellae with a small degree of branching [26]. 127
4.32 SEM pictures of semicrystalline PLA 2500HP with 5% of lignin. . . 128
4.33 SEM pictures of amorphous PLA 4060D with 5% of lignin. 129

5.1 Comparative plot of the main properties of the modified semi-crystalline PLA relative to the values for the reference material. . . 131
5.2 Comparative plot of the main properties of the modified amorphous PLA relative to the values for the reference material. 132

6.1 Evolution of (a) the glass transition temperature T_g, (b) the melting temperature T_m and (c) the degree of crystallinity χ_c of modified PLA2500HP with addition of lignin. 136
6.2 Evolution of glass transition temperature T_g of modified PLA4060D with addition of lignin. 137
6.3 Evolution of he starting point of thermal degradation T_s of (a) modified PLA2500HP and (b) modified PLA4060D the melting temperature T_m with addition of lignin. 137
6.4 Evolution of (a) the storage modulus $E^{'}$, (b) the loss modulus $E^{''}$, (c) $tan\delta$ and (d) the glass transition temperature T_g of modified PLA2500HP with addition of lignin. 138
6.5 Evolution of (a) the storage modulus $E^{'}$, (b) the loss modulus $E^{''}$, (c) $tan\delta$ and (d) the glass transition temperature T_g of modified PLA4060D with addition of lignin. 139
6.6 Stress-strain curves for PLA2500HP neat extruded. 140
6.7 Stress-strain curves for PLA2500HP - 1wt%Lignin blend. 140
6.8 Stress-strain curves for PLA2500HP - 5wt%Lignin blend. 140
6.9 Stress-strain curves for PLA2500HP - 10wt%Lignin blend. 140
6.10 Stress-strain curves for PLA2500HP - 20wt%Lignin blend. 140

6.11 Stress-strain curves for PLA2500HP - 30wt%Lignin blend. 140
6.12 Stress-strain curves for PLA4060D neat extruded. 141
6.13 Stress-strain curves for PLA4060D - 1wt%Lignin blend. 141
6.14 Stress-strain curves for PLA4060D - 5wt%Lignin blend. 141
6.15 Stress-strain curves for PLA4060D - 10wt%Lignin blend. 141
6.16 Stress-strain curves for PLA4060D - 20Lwt%Lignin blend. 141

List of Acronyms

AIER	acid ion exchange resin
ASTM	american society for testing and materials
BC	bacterial cellulose
BPA	bisphenol A
CN	cellulose nanocrystal
CNF	cellulose nanofibril
CNT	carbon nanotube
CRIPS	cure-reaction-induced phase separation
DDS	diaminodiphenylsulfone
DGEBA	bisphenol A diglycidyl ether
DGEBF	bisphenol F diglycidyl ether
DICY	dicyandiamide
DMA	dynamical mechanical analysis
DSC	differential scanning calorimetry
DTA	diethylenetriamine
EA	acrylate-ethylene
ELO	epoxidized linseed oil
EPN	epoxidized phenol novolac
ESO	epoxidized soybean oil

FTIR	fourier-transform infrared spectroscopy
HDKLF	hardwood kraft lignin fiber
ISO	international standards organisation
LCF	lignin-based carbon fiber
LCST	lower critical solution temperature
LEFM	linear elastic fracture mechanics
MAF	mobile amorphous fraction
MCDEA	methylenechlorodiethylaniline
MDA	methylenedianiline
MFC	microfibrillated cellulose
NFC	nanofibrillated cellulose
NG	nucleation and growth
OGLF	organosolv lignin fiber
OP	optical purity
PA12	polyamide 12
PKHH	polyhydroxyether of bisphenol-A
PLA	polylactic acid
PLLA	poly-L-lactic acid
PP	polypropylene
PE	polyethylene
PS	polystyrene
PET	polyethylene terephtalate
PCL	polycaprolactone
PHB	polyhydroxybutyl

PHBV	polyhydroxybutyratevalerate
PHA	polyhydroxyalcanoate
PGMA	polyglycidyl methacrylate
PES	polyethersulphone
PEI	polyetherimide
PSF	polysulfone
RAF	rigid amorphous fraction
ROP	ring opening polymerisation
SD	spinodal decomposition
SEM	scanning electron microscopy
SENB	single edge notched bending
TAG	triacylglycerol
TGA	thermogravimetric analysis
TGAP	triglycidyl aminophenol
TGDDM	tetraglycidylether diaminodiphenylmethane
THAP	tetrahydrophtalic anhydride
TP	thermoplastic
TPS	starch-based polymers
TS	thermoset
TTT	time temperature transformation
UCST	upper critical solution temperature

List of Symbols

Thermal Properties

ΔH_c	Cold crystallisation enthalpy
ΔH_m	enthalpy of fusion
ΔH_f°	Melting enthalpy of a completely crystalline material
c_p	Specific heat
T_m	Melting temperature
T_g	Glass transition temperature
T_g^∞	Glass transition temperature for a molecule of infinite molar mass

Mechanical - Physical Properties

ν	Poisson's ratio
ρ	Density
σ_b	Strength at break
σ_u	Ultimate tensile strength
σ_y	Yield strength
$\tan\delta$	Damping factor
ε	Relative strain
ε_b	Strain at break
ε_t	Nominal strain
E	Young's modulus

E'	Storage modulus
E''	Loss modulus
G_{Ic}	Energy release rate
K_{Ic}	Stress intensity factor

Thermodynamics Symbols

χ_{12}	Flory-Huggins parameter
ΔG_m	Free energy of mixing
ΔH_m	Enthalpy of mixing
ΔH_m^{ns}	Enthalpy of mixing due to non-specific interactions
ΔH_m^s	Enthalpy of mixing due to specific interactions
ΔS_m	Entropy of mixing
ΔS_m^C	Combinatorial entropy of mixing
ΔS_m^{NC}	Non-combinatorial entropy of mixing
g_v	Volume free energy

Other Symbols

α	Crosslinking rate
$\bar{M_n}$	Average molar mass in number
$_c$	Degree of crystallisation of a polymer
η_i	Viscosity of polymer i
ϕ_i	Volume fraction of phase i
a	Crack length
D	Diffusion coefficient
f_i	Volume fraction of phase i
k	Boltzmann constant

L	Clamping distance
L_0	Gauge length
L_t	Displacement of the crosshead
w_i	Weight fraction of polymer i
X_D	Amount of D-enantiomer
X_i	Degree of polymerisation

Chapter 1

General Introduction

Climate changes and environmental questions are more and more important for the society and thus for the compagnies. Reduction of environmental impacts, CO_2 footprint and water consumption are now main concerns for engineers from the beginning of the design to the end of life of a product. Engineers have to take into account the entire life cycle of the object when choosing the most appropriate materials for an application. The choice of the most eco-friendly material becomes a main issue while it must be compatible with the constraints of the application. In this respect composites are considered as ideal candidate materials to replace heavy and pollutant ones. Indeed they possess many outstanding properties and therefore are used in many industrial fields. Epoxy resins are widely used today as composite matrices because of their excellent properties that enable them to be essential in many fields of activity such as aerospace, automobile, electronic and painting industry. Bi-component epoxy resins present excellent mechanical properties, low density, good chemical and thermal resistances and their processing is easy.

Nonetheless, due to high cross-linking density, epoxy resin are intrinsically brittle and notch sensitive limiting their use. To compensate those drawbacks several approaches exist and they can be classified in two categories [30]: chemical modifications and addition of a second phase. On one hand chemical modifications decrease the cross-linking density by increasing the molecular mass of the monomer and/or by decreasing the hardener functionality. On the other hand the second phase added can be a rubber or a thermoplastic one. This second phase will limit the propagation of cracks due to different toughening mechanisms.

Even if composites allow to reduce the environmental impact by reduction of object's weight, difficulties of recycling and toxicity of some of their components push researchers to develop bio-sourced epoxy resins and composites. As a matter of fact the energy needed for the recycling, when it is possible, can cancel all the

advantages gained by choosing this material. Most petrochemical epoxy resins use bisphenol A diglycidil ether (DGEBA) as monomer derived from bisphenol A (BPA) which has highly negative health effects [1]. This is why engineers try to replace those petroleum-based composites by bio-sourced composites.

It is in this context that this work is being carried out. As indicated by the title, the aim of this work is to study the influence of a thermoplastic nanocomposite on an epoxy resin. Semicrystalline polylactic acid (PLA) based composites and amorphous polylactic acid (PLA) based composites with different loading rate of lignin particles are studied. The following step consist to study the influence of the addition of such nanocomposite in a bio-sourced epoxy resin on its mechanical properties. Unfortunately this second part could not be carried through the end. This work is part of the european MACOBIO project developped at the Institute of Condensed Matter and Nanosciences at UCLouvain in the Bio- and Soft Matter department [44].
After a bibliographic review resuming the theory about the subjects covered in this work and a literature review about thermoplastic nanocomposites, epoxy resin and toughening mechanisms, the experimental part presents the material investigated, the processing techniques and characterisation techniques used. The next chapter describes the results obtained and is divided in three main parts. The first and second ones cover the thermal and mechanical characterisation of the nanocomposites. The third part presents the analysis of charges' dispersion.

Chapter 2

Bibliographic review

This chapter presents a literature review about the theory related to the notions and concepts specific to the achievement of this work. In a first part, Polylactic acid, its synthesis and some of its properties are first described. Then lignin synthesis and its characteristics as natural filler are described. Epoxy resin and bio-sourced epoxy resin are also presented. In a second theoretical part, a brief description of the thermodynamics, phase separation, morphology and properties of polymer blends is given. An additional theoretical part describes mechanical properties measurements and fracture mechanics.
Finally a literature review about thermoplastic nanocomposites and more specifically lignin incorporation in PLA is done as well as a review of some studies about improvement of epoxy resin with thermoplastic addition.

2.1 Theory

2.1.1 Polylactic acid (PLA)

Polylactic acid also called polylactide is a biodegradable bio-sourced thermoplastic polymer made of lactic acid and belonging to the family of aliphatic polyesters. PLA was discovered in the 1920s by Carothers, the scientist who invented nylon and is usually synthesised from α-hydroacids [3, 11, 45].
Building block of PLA, lactic acid or 2-hydroxypropanoïc acid is produced by the fermentation of sugars or starch derived from renewable agro-ressources such as corn, sugar-cane, potato or beet.

PLA can be either amorphous or semi-crystalline according to the stereochemistry of the carbon backbone. The lactic acid molecule is indeed chiral. Two distinct stereoisomers exist: the L-lactic acid and the D-lactic acid. They are illustrated in Figure 2.1. The enantiomer L is the most abundant in nature and the proportion of the enantiomers determines PLA's material properties.

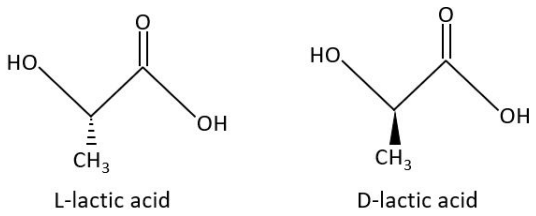

Figure 2.1: Illustration of the two lactic acid enantiomers : L-lactic acid and D-lactic acid.

2.1.1.1 Synthesis of PLA and structural composition

Different synthesis routes to obtain PLA with high molar mass are illustrated in Figure 2.2: condensation/coupling of pre-polymers, azeotropic distillation and polymerisation by opening the lactide ring.

In the first method, the PLA is synthesised by direct polycondensation of lactic acid. Unfortunately, the polycondensation only allows to obtain low molar mass polymers due to the presence of water and impurities in the reactor. Therefore, one can use coupling agents or additives favouring the esterification but increasing the costs [11, 45].

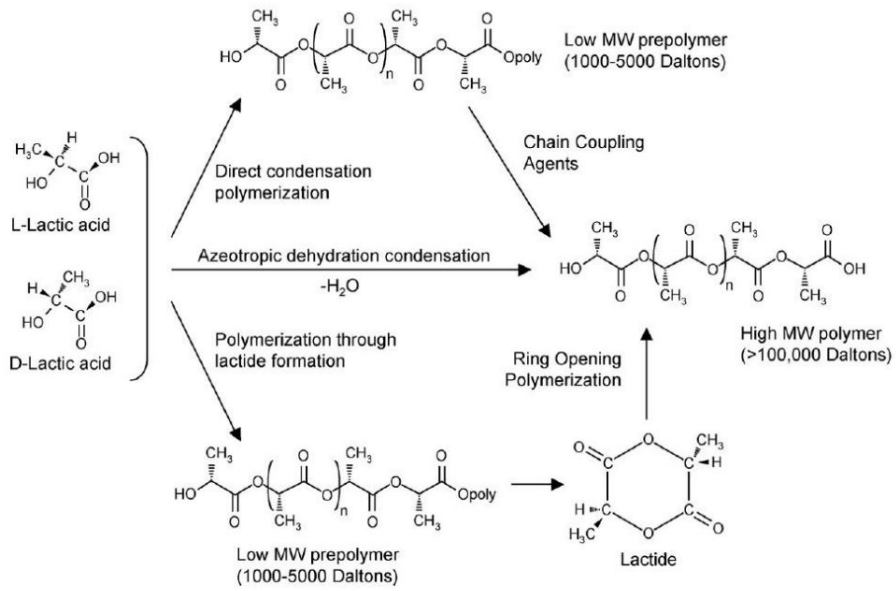

Figure 2.2: Synthesis routes of PLA [3, 11].

The polymerisation by azeotropic condensation allow to obtain directly high molar mass polymers without the use of chains extensors. In this method, the lactic acid is distilled at low pressure during 2 to 3 hours at $130°C$ in order to remove the major part of water produced by the condensation reaction. This process has the disadvantage of using a quite high amount of catalyst which is find back in the final product and which can be the source of problems for further processing [11, 45]. Though the most industrially used method to synthesised PLA is the polymerisation by ring opening of the lactide also known as ROP. This method, used by *NatureWorks* among others, has a better throughput and allows a good control of the molar mass. First a pre-polymer is produced by polycondensation, under vacuum and at high temperature. Next the lactide is obtained by a catalysed depolymerization of short chains of PLA at low pressure [11, 45]. A mix of different cyclic dimers is obtained : the L-lactic acid, the D-lactic acid and the meso-lactide as shown in Figure 2.3. The ring opening is a reversible reaction. Consequently depolymerisation can occurs by inter-molecular and intra-molecular (called back-bitting) trans-esterification.

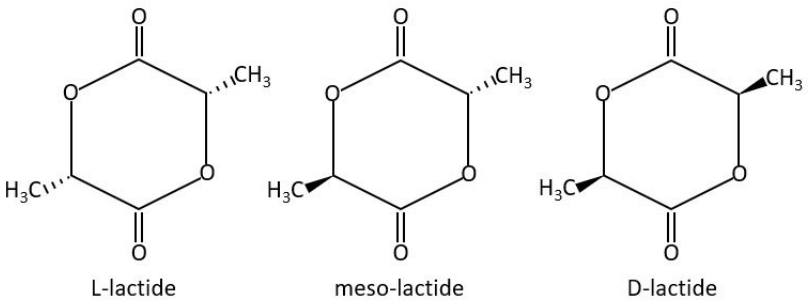

Figure 2.3: Illustration of the three lactide stereoisomers.

The processing, the crystallisation and the degradation of PLA are influenced by the (stereochemical) structure, by the composition of the chains and particularly by the ratio of enantiomers L- and D- of lactic acid. The enantiomers L is the natural form and is thus the most abundant. Therefore, copolymers of PLA contain mainly the L form [11, 45].
The isotactic homopolymer PLLA, synthesised exclusively from L-lactide, is semi-crystalline and has the highest melting temperature that can be obtained whereas the PLA copolymers with high content of the D-isomers have a lower melting temperature and a slower crystallisation speed. The synthesised PLA are thus either semi-crystalline or amorphous. PLA with more than 93% of L-lactic acid are semi-crystalline polymers while PLA containing between 50% and 93% of L-lactic acid are considered as completely amorphous (content of D isomer higher or equal to 17%). The quantity of the D-form can be determined by the optic purity OP defined as the amount of L-form in the sample and given by the following Equation 2.1 [3, 11, 45].

$$OP = \frac{[L] - [D]}{[L] + [D]} \tag{2.1}$$

2.1.1.2 Properties of PLA

The properties of polylactide are diverse due to the chirality of the lactic acid molecule. By varying the composition and the molar mass of PLA, a large variety of physical and mechanical properties can be obtained. In comparison with existing petroleum-based polymers, PLA's optical, physical, mechanical and barrier properties are reasonably good [3, 11, 45].

The major advantages of PLA are listed below:

- its transparency for amorphous or slightly crystalline PLA;
- it is an eco-friendly material;
- its biocompatibility;
- its processability : PLA can be processed in various techniques such as extrusion, injection moulding, blow moulding, thermoforming,...

However ploylactic acid presents several drawbacks: its brittleness, its slow degradation rate, its fast hydrolysis rate and its poor thermal resistance as well as its hydorphobic nature and its chemically passive character [46]. In addition, the water demand of biopolymers, especially for PLA, is high, as shown in Figure 2.4, due to the fact that they derive from plant or animal feedstock. In comparison with commodity plastics (PP, PE or PS), PLA is about 25% more expensive per unit volume and only starch-based polymers (TPS) have significantly lower embodied energy due to fermentation and/or processing as depicted in Figure 2.5 [12].

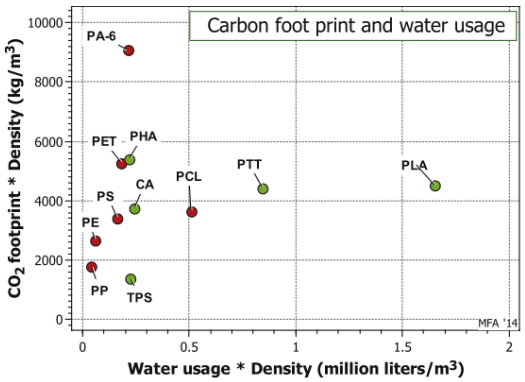

Figure 2.4: Carbon footprint and water usage of oil-based polymers (red points) and biopolymers (green points) [12].

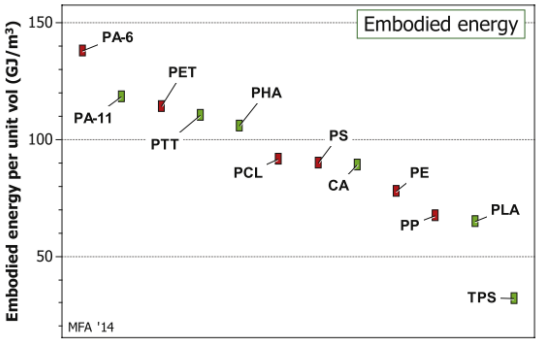

Figure 2.5: Embodied energy of oil-based polymers (red points) and biopolymers (green points) [12].

2.1.1.2.1 Crystallisation

PLA can be either amorphous or semicrystalline depending on its thermal history and stereochemistry. The amorphous and slightly crystalline PLA are light and transparent materials whereas highly crystalline PLA are white and opaque.
Depending on the end-use, the desired crystallinity of PLA can vary. For instance, increased crystallinity will be desirable for injection molded items for which good thermal stability is important. One of the strategy to increase the crystallinity of PLA is to add nucleating agent in the polymer during extrusion. Incorporating nucleating agent lowers the surface free energy barrier for nucleation and therefore allows crystallisation at higher temperature to take place upon cooling. Crystallisation of PLA can also be initiated by annealing at temperatures between T_g and T_m owing to improve thermal stability [3]. When quenched from the melt phase like during injection molding, the optically pure PLA polymer becomes quite amorphous. Cooling polylactic acid at a slow cooling rate will result a highly crystalline polymer with a lower enthalpy of crystallisation whereas when quenching it at high cooling rate, an exothermic crystallisation peak during reheating will appear in the DSC thermogram as shown in Figure 2.6. Moreover the tendency for PLA to crystallise upon reheating depends on the optical purity of the polymer (Figure 2.7) and on the heating rate (Figure 2.8).

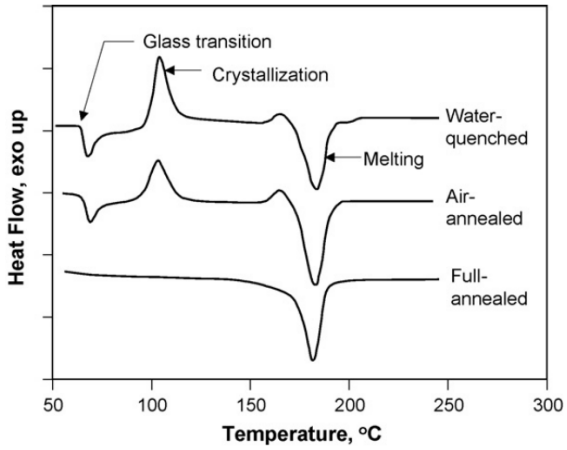

Figure 2.6: DSC scans of water quenched, air-annealed (cooled from 220[$°C$] to ambient temperature in 5 minutes, quenching), and full-annealed (cooled from 220$°C$ to ambient temperature in 105 minutes, slow cooling) PLLA samples. The scans were performed at a heating rate of 10[$°C/min$] [3].

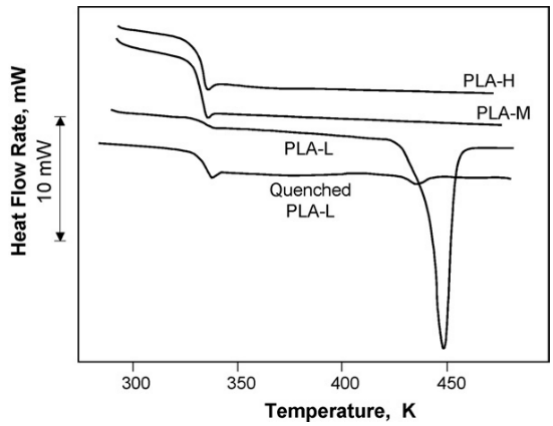

Figure 2.7: DSC scans at 20$[K/min]$ for PLA with 1.5% (PLA-L), 8.1% (PLA-M), and 16.4% (PLA-H) D-isomers. All samples were cooled quickly from the melt and isothermally crystallized at 145$[°C]$ for 15 hours. The quenched PLLA sample did not undergo the 15 hours isothermal crystallisation [3].

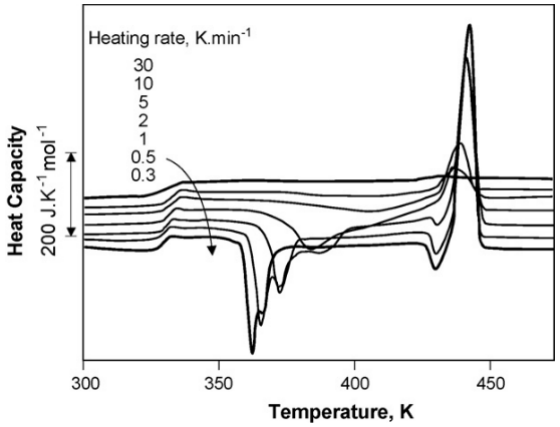

Figure 2.8: DSC scans for 1.5% D-lactide PLA samples cooled from the melt at 10$[K/min]$ and then reheated at different heating rates from 30 to 0.3$[K/min]$ [3].

Degree of crystallinity In general for the homopolymer PLLA which is the most crystalline form, the maximum degree of crystallinity $\chi_{c,max}$ can reach up to 40%. This is smaller than the maximum degree of crystallinity of other polyesters, such polyethylene terephthalate (PET). This low value can be explained because of more flexible macromolecules and easier macromolecule rearrangements compared to other polyesters such PET [47, 48]. The addition of D enantiomer to obtain a copolymer PDLLA, causes a drop of the degree of crystallinity until $OP < 0.75$:

the PLA is thus considered as amorphous.
The degree of crystallinity χ_c of PLA can be determined from the enthalpy of fusion ΔH_m and the cold crystallization enthaply ΔH_c measured using differential scanning calorimetry (DSC):

$$\chi_c(\%) = \frac{\Delta H_m - \Delta H_c}{\Delta H_f^0} \times 100 \tag{2.2}$$

The value of the melting enthalpy of a completely crystalline material found in the literature, is $\Delta H_f^0 = 93.1[J/g]$ [3, 11, 47, 48].
When charges are added in a PLA matrix, the equation above has to take into account the percentage of charges in the blend, with W_{PLA} the matrix weight fraction [49]:

$$\chi_c(\%) = \frac{\Delta H_m - \Delta H_c}{\Delta H_f^0 \ W_{PLA}} \times 100 \tag{2.3}$$

The enthalpy of fusion ΔH_m corresponds experimantally in a DSC scan to the fusion of the whole crystal part of the sample, i.e. the fusion of the crystalline phase developped during the heating scan measured by the peak of cold crystallisation and the fusion of the crytalline phase already present before the DSC scan or formed during the cooling scan [47].

Crystalline structures The polylactic acid (PLA) is a polymorph : the PLA can adopt four different structural crystalline forms according to the applied crystallisation conditions. They are characterised by different helix conformations and cell symmetries. The four main crystalline forms of PLA are: α,α' or δ, β, γ. The most common form, the α form is obtained with normal crystallisation conditions :it grows upon melt or cold crystallisation. It is characterised by a chain conformation as a left-handed 10_3 helix packed into an orthorhombic unit cell [2, 45].
The β form is obtained from solution-spinning at high temperatures, or by mechanical stretching (drawing of PLLA fibres at high speed) of the more stable α phase. Studies conducted by Puiggali et al [50] determined that the β form is a frustrated structure of three three-fold helices in a trigonal unit cell able to accommodate the random orientation of neighbor chains associated with rapid crystallisation conditions [2, 45].
The disordered $\alpha^{'}$ structure is obtained for a crystallisation temperature below $90°C$, while the PLLA crystallises in the α form for a temperature higher than $120°C$. The γ structure develops upon epitaxial crystallisation on a substrate of hexamethylbenzene. The γ phase is composed of two antiparallel helices packed in an orhtorhombic unit cell [2, 11, 45]. The parameters of the unit of the α, β and γ

phases are reported in Table 2.1.
In addition, a blend of PLLA and PDLA allows to obtain a stereo-complex which has higher thermal properties than a classical PLLA due to a crystalline structure more compact [11, 45].

Table 2.1: Unit cell's parameters of PLA crystalline structure [2].

	Unit cell	a $[nm]$	b $[nm]$	c $[nm]$
α	orthorhombic	1.06	1.737	2.88
β	trigonal	1.052	1.052	0.88
γ	orhtorhombic	0.995	0.625	0.88

Moreover, several authors have identify the presence of a rigid amorphous fraction (RAF) in several polymers such PET and PLA. The PLA can thus be described as a three phases model: a crystalline phase and two amorphous phases, the mobile (MAF) and the rigid amorphous fraction (RAF). The RAF fraction does not participate in the glass transition of the mobile amorphous phase. However, according to Wunderlich [51], the RAF seems to decrease and disappear gradually above the glass transition T_g of the MAF and does not remain rigid up to the melting temperature [11, 45, 47]. The amount of RAF can be considered as a measure of the coupling between the amorphous and the crystalline phases as stated by Andorsch [52].
Concerning PLLA, the RAF can reach 13% for highly crystallised PLLA which is low. The coupling between the crystalline and the amorphous phase is weaker than for PET for instance. Moreover, the coupling between MAF and RAF is also weak [47]. The material remains a "fragile" material.

2.1.1.2.2 Thermal properties

PLA can be completely amorphous or semicrystalline with a degree of crystallinity that can reach 40% and those characteristics will influence the thermal transition of PLA.

Glass transition In general, the glass transition temperature T_g of PLA is about $60[^\circ C]$. Nevetherless, the T_g of PLA is dependant both on the molecular weight and on the optic purity of the polymer [3].
The variation of the glass transition temperature with the molecular weight is given by the Flory-Fox equation (Equation 2.4): with T_g^∞ the glass transition temperature

for a molecule of infinite molar mass, K a constant and $\bar{M}_n$ the average molar mass in number. Values of T_g^∞ and K are reported to be around $57 - 58[^\circ C]$ and $(5.5 - 7.3) \times 10^4$ respectively [3]. One can say that T_g increases with the molar mass.

$$T_g = T_g^\infty - \frac{K}{\bar{M}_n} \tag{2.4}$$

To illustrate the dependence of T_g on the optic purity, the Table 2.2 shows the glass transition and melting temperatures of different PLA polymers with different ratios of copolymers.

Table 2.2: Transition temperatures of selected PLA copolymer [3].

Copolymer ratio	$T_g\,[^\circ C]$	$T_m\,[^\circ C]$
100/0 (L/D,L)-PLA	63	178
95/5 (L/D,L)-PLA	59	164
90/10 (L/D,L)-PLA	56	150
85/15 (L/D,L)-PLA	56	140
90/20 (L/D,L)-PLA	56	125

One can observe that the amount of D-enantiomers influences the glass transition temperature. Indeed, the T_g of polymer is linked to the molecular movement; the addition of imperfections (segment of D-enantiomer) along the chain can disturb the molecular dynamic. Empirical equations (Equation 2.5 and Equation 2.6) have been proposed to link T_g^∞ and K to X_D the amount of D-enantiomer [11, 48]. As a matter of fact, T_g increases with the amount of L isomers.

$$T_g^\infty = \frac{13.36 + 1371.68 X_D}{0.22 + 24.3 X_D 0.42 X_D^2} \tag{2.5}$$

$$K = 52.23 + 791 X_D \tag{2.6}$$

The glass transition behavior of PLA also depends on the thermal history of the polymer. Quenching PLA from the melt at a high cooling rate (as during injection molding) will result in a highly amorphous polymer. Rapid ageing occurs for PLA polymers with low crystallinity under ambient conditions. This phenomenon has a significant contribution to the embrittlement of PLA [3].

Melting temperature The melting temperature for a semi-crystalline PLA can take value in the range $120°C < T_m < 180°C$ according to the molar mass and the amount of D-isomer as shown in Table 2.2.
The optic purity influences strongly the lamellar structure during the crystallisation. For a given molar mass, a decrease of the optic purity will generate a drop of the melting temperature.
In general, the melting temperature of semi-crystalline polymers evolves in function of the lamellar thickness according to the equation of Gibbs-Thomson [11, 48]. The Flory equation (Equation 2.7) gives the melting temperature of a statistic copolymer T_m^c in function of the amount of the major specie X and intrinsic parameters T_m^0 and ΔH_m^0.

$$\frac{1}{T_m^c} = \frac{1}{T_m^0} - \frac{k}{\Delta H_m^0} lnX \tag{2.7}$$

The molar mass is also an important parameter influencing the melting temperature. However, the molar mass effect is less important than the one of the optic purity on T_m. Indeed, T_m decreases significantly only for a molar mass below $20000[g/mol]$. The variation of T_m with the molar mass can be described empirically by Equation 2.8 [11]: with $T_m^0 = 181.3[°C]$ the melting temperature for a polymer with an infinite molar mass and $A = 1.02 \times 10^5[g°C/mol]$.

$$T_m = T_m^\infty - \frac{A}{M_n} \tag{2.8}$$

Thermal stability Polylactic acid as the majority of aliphatic polyesters has a poor thermal stability in the molten state. Indeed several reactions decreasing the molar mass can occur due to thermal, residence time and shear stresses effects while processing: hydrolysis due to remaining water, depolymerisation through a back-bitting mechanism, random oxidative main-chain scission, intermolecular and intramolecular trans-esterification reactions forming cyclic lactic acid oligomers or low-molar mass lactide [3, 45]. In addition, PLA is higlhy hydrolasable due to the presence of a C-O bond.
For the processing, the formation of lactide due to depolymerization is undesirable. Besides reducing PLA elasticity and melt viscosity, the volatile lactide formed can lead to fuming and/or fouling of the processing equipment such as molds and tooling surfaces (building up of layer of lactide).
The hydrolysis kinetics depends on the water and remaining catalyst (used for the polymerisation) concentrations. Consequently, PLA must be dried sufficiently before processing it in order to reduce the thermal degradation and avoid excessive hydrolysis. Moreover the removal of residual catalyst and monomer molecules allow

to improve the stability of PLA. Stabilisers can also be added to prevent PLA degradation [3, 45].

2.1.1.2.3 Physical and Mechanical properties

Mechanical characteristics of PLA are more or less comparable to the one of polyethylene terephthalate as depicted in Figure 2.9 and Figure 3.13 [12, 46].

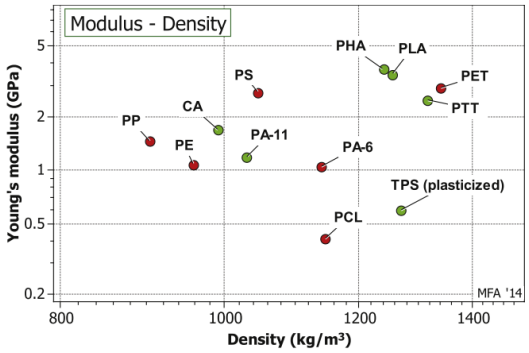

Figure 2.9: Young's modulus E and density ρ of commodity oil-based polymers (red points) and biopolymers (green points), with contours of $\frac{E}{\rho}$ [12].

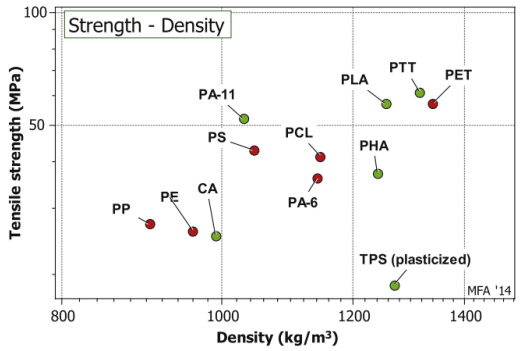

Figure 2.10: Tensile strength and density ρ of commodity oil-based polymers (red points) and biopolymers (green points), with contours of $\frac{\sigma_t}{\rho}$ [12].

PLA exhibits a Young's modulus on the range of $3-4[GPa]$, a tensile strength from 50 up to $70[MPa]$ [53] and an impact strength to $2.5[kJ/m^2]$. However its use is limited due to its low elongation at break which is around $2-10[\%]$. Table 2.3 and Table 2.4 present physical and mechanical properties of PLA depending on stereochemistry and crystallinity.

The mechanical properties of semi-crystalline PLLA are quite attractive in comparison with other common polymers such as polyethylene (PE), polyethylene terephtalate (PET), polystyrene (PS) and polypropylene (PP) especially its Young's modulus. Nevertheless, PLA exhibits a brittle behavior with low impact strength which constitutes one of its main limitations [53].

Table 2.3: Effects of stereochemistry and crystallinity on mechanical properties [4].

Properties	Unit	PLLA annealed	PLLA	PDLLA
Tensile strength	$[MPa]$	59	66	44
Elongation at break	[%]	7	4	5.4
Young's modulus	$[MPa]$	3750	4150	3900
Yield strength	$[MPa]$	70	70	53
Flexural strength	$[MPa]$	106	119	88
Unnotched izod impact	$[J/m]$	195	350	150
Notched izod impact	$[J/m]$	26	66	18
Rockwell hardness	/	88	88	76
Heat deflection temperature	$[°C]$	55	61	50

Table 2.4: Physical properties of PLA [4].

Properties	Unit	PLA	PLLA	PDLLA
Polymer density ρ	$[g/cm^3]$	1.21-1.25	1.24-1.30	1.25-1.27
Tensile strength σ	$[MPa]$	21-60	15.5-150	27.6-50
Tensile modulus E	$[GPa]$	0.35-3.5	2.7-4.14	1-3.45
Ultimate strain ϵ	[%]	2.5-6	3.0-10.0	2.0-10.0
Specific tensile strength σ^*	$[Nm/g]$	16.8-48.0	40.0-66.8	22.1-39.4
Specific tensile modulus E^*	$[kNm/g]$	0.28-2.80	2.23-3.85	0.80-2.36
Glass transition temperature T_g	$[°C]$	45-60	55-65	50-60
Melting temperature T_m	$[°C]$	150-162	170-200	/

2.1.2 Lignin

Lignin is the second most abundant natural filler after cellulose, it is composed of aromatic moieties. Lignin is a characteristic component of higher plants with a well developed vascular system. Actually lignocellulosic materials are made of 3 components as depicted in Figure 2.11: a polysaccharide derived from glucose called cellulose, an heteropolysaccharide hemicellulose and a complex phenolic heteropolymer called lignin [15, 54].
Since lignin is one of the most hydrophobic components in plant cell walls, its presence enables the waterproofing of vascular tissue allowing the transport of

water and nutrients and providing protection for plants against pathogens. In addition lignin plays an important role in the cellular wall rigidity and in the plant longevity as the phenolic group of lignin can capture free radicals [14, 15].

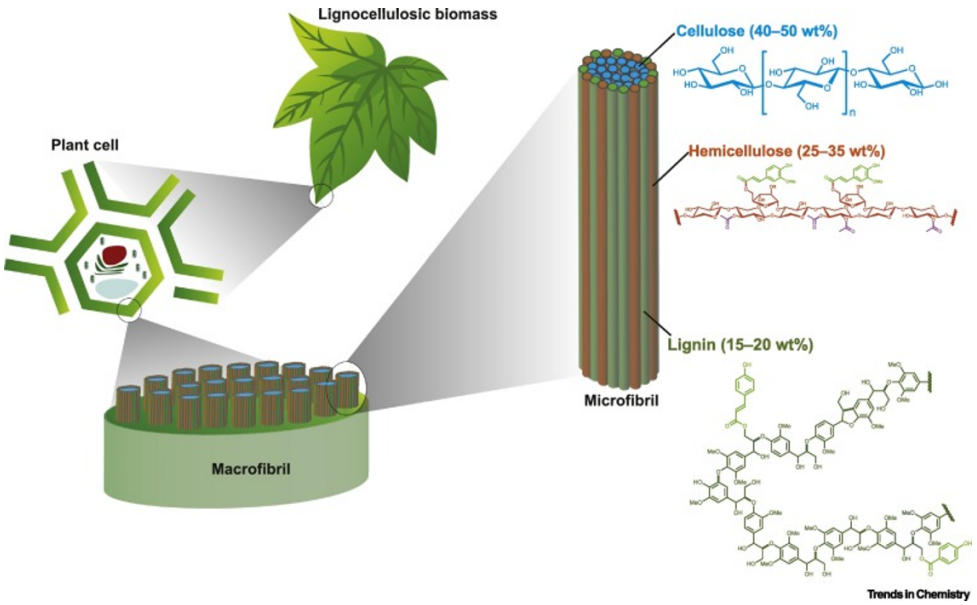

Figure 2.11: Structure of Lignocellulosic Biomass [13].

2.1.2.1 Lignin synthesis

The biosynthesis of lignin occurs through the dehydrogenative polymerization of 3 hydroxycinnamyl alcohol monomers or monolignols: the p-coumaryl (H) alcohol, the coniferyl (G) alcohol and the sinapyl (S) alcohol. The three monolignols are represented in Figure 2.12). The composition and content of lignin differ among tissues and species.
The biosynthesis of lignin involves 3 steps : the biosynthesis of monolignols, the transport of monolignols to the cell wall and finally the enzymatic dehydrogenative polymerization of monolignols in the cell wall [14, 15]. This monolignols polymerisation occurs by covalent bonding between $C_4 - O$, C_5, C_α and C_β positions.

Lignins can be considered as amorphous polymers, however they are very different from synthetic polymers due to the complexity of inter-units bondings and the heterogeneity of monomers as shown in Figure 2.13 [15]. Moreover, lignin is totally biodegradable.

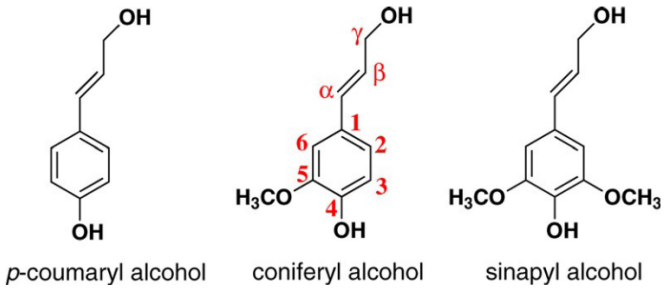

Figure 2.12: Chemical structures of hydroxycinnamyl alcohol monomers [14].

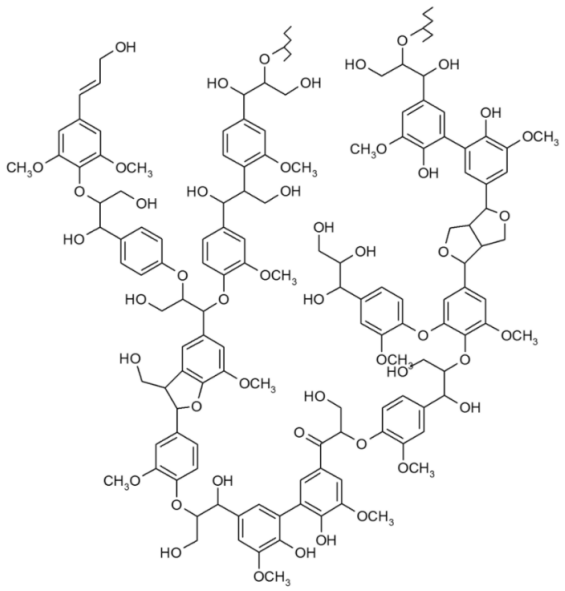

Figure 2.13: Presumed structure of lignin of conifers [15].

Lignin is isolated from lignocellulosic biomass either by removing carbohydrates using enzymatic hydrolysis or by dissolving lignin through chain scission. Lignin isolation processes can be enzymatic, chemical or mechanical. All of them can lead to chain scission or chemical structure alterations due to the reaction conditions (high temperatures, high pressures, high or low pH) of those processes. Industrial lignins are distinguished according to the pulping processes [14, 15].

2.1.2.2 Types of lignin

2.1.2.2.1 Lignosulfonates

Lignosulfonates have a high sulphur content around $5wt\%$ with a degree of sulfonation of $0.4 - 0.5$ per phenylpropanoid unit. Lignosulfonates are usually water-soluble anionic polyelectrolytes and are recovered as byproducts from sulfite pulping process. Lignin is extracted from wood chips under high pressure at $140 - 160°C$ thanks to the addition of sulphurous acid and/or its alkali salts. Ultrafiltration is used in industrial scale process to recover lignosulfonates. The bisulfite process is performed at pH around $4.0 - 5.0$ while the acid sulfite process is usually conducted at pH around $1.5 - 2.0$. The main reactions involve in a sulfite process are the following: sulfonation at the C_α carbon atom of the lignin which makes lignosulfonates soluble in water, fragmentation through aryl ether bond cleavage and condensation between the lignin fragments [14, 15].

2.1.2.2.2 Kraft lignin

In paper and pulp industry, the kraft process is the dominant process. In this process, lignin is fragmented through cleavage of α-aryl ether and β-aryl ether bonds by the anions (hydroxide and hydrosulfide) in the cooking liquor. The cleavage leads to increased phenolic hydroxy groups in kraft lignin [14].
The molecular size of the resulting lignin fragments increases due to the formation of alkali-stable $C - C$ bonds due to condensation reactions such as crosslinking and repolymerization between lignin molecules. During those condensation reactions, trace amounts of sulphur are added into kraft lignin because of the use of external nucleophiles in the cooking liquor, $-SH$ groups for instance. Precipitation under acidic conditions or ultrafiltration allows to recover kraft lignin from the black liquor. Kraft lignin is soluble at high pH and has a low level of sulphur (around $1.5 - 3\%$. Difference of kraft lignin compared to other natural lignins are the $\beta - O - 4$ bond scission and the ionisation of phenolic functions [14, 15].

2.1.2.2.3 Soda lignin

Soda lignin is extracted from a soda pulping process. Soda process is usually used to process easily pulped materials like bamboo, flax, straws and some hardwoods. In order to solubilize lignin, soda pulping employs sodium hydroxide or sodium hydroxide-anthra-quinone as cooking chemicals. The athraquinone / anthrahydro-quinone redox system in the process significantly improves cleavage of $\beta-$aryl ether bonds and hinders condensation of the resulting lignin segments. Soda lignin has a relatively high carboxylic acid content because of the oxidation of the aliphatic hydroxy groups. However soda lignin is sulphur free [14, 15].

2.1.2.2.4 Organosolv lignin

Organosolv lignin is recovered under moderate conditions from wood chips with water with a small amount of base or acid as a catalyst and with organic solvents such as alcohols, ketones and glycols. In the paper-making industry, the organosolv process is not often used but this process has been considered as increasingly interesting as a pretreatment for biofuel production owing to its environmental characteristics. In the organosolv process, cleavage of $\alpha-$ and $\beta-$aryl ether bonds results in the fragmentation of lignin. In addition, condensation reactions involving aquinone methide intermediate or carbocations occur. Organosolv lignin has a better solubility in organic solvents, high purity, a low sulphur content and low molecular weight with a narrow molecular-weight distribution compared to other technical lignins. The low molecular mass of organosolv lignin makes it interesting in the biomaterial field [14].

2.1.2.3 Lignin-based carbon fibres

In order to produce lignin-based carbon fibres (LCFs), pre-treatments are needed: purification, refining, modification and blending. Then lignins are often pelletised before spinning to improve their spinnability. Next lignins are spun into fibres by extrusion techniques such melt-spinning, wet-spinning, dry-spinning, gel-spinning and electrospinning. Thereafter lignin fibres are stabilised at $200 - 280°C$ and carbonised at temperatures higher than $800°C$ under inert atmosphere. Additional graphitization or activation can be done to enhance mechanical properties or increase surface area [55].
Mechanical properties of two kinds of lignin fibres studied in 2002 [5] are listed in Table 2.5: hardwood kraft lignin fibres (HDKLF) and Organosolv lignin fibres (OGLF).

Table 2.5: Lignin fibre's properties [5].

	Diameter $[\mu m]$	Tensile strength σ $[MPa]$	Young's modulus E $[GPa]$	Elongation at break ε [%]
HDKLF	46 ± 8	422 ± 80	40 ± 11	1.12 ± 0.22
OGLF	31 ± 3	388 ± 123	40 ± 14	1.00 ± 0.23

2.1.2.4 Thermal stability of lignin

Lignin is moderately stable at elevated temperatures due to its highly aromatic backbone. Indeed, lignin decomposes slowly and over a broad range of temperatures

$200 - 500°C$, slower and over a broader range of temperatures than cellulose and hemicellulose components of biomass (see Figure 2.14). Lignin thermally decomposes over a broad temperature range, because of the various oxygen functional groups from its structure have different thermal stabilities and their scission occurs at different temperatures.
Literature shows that during thermogravimetric analysis (TGA) under a nitrogen atmosphere, lignin loses only 40% of its intial mass below $700°C$ upon heating. Heated up at a rate of $10°C/min$, lignin decomposes at a rate slightly slower than $0.15wt\%/°C$. The degradation rate slightly increases to $0.3wt\%/°C$ above $750°C$, the mass loss at $850°C$ being about $67wt\%$. It is reported that the maximum mass loss is observed around $400°C$ for kraft lignin and that about 15% of the mass loss is observed below $300°C$ [54, 56].

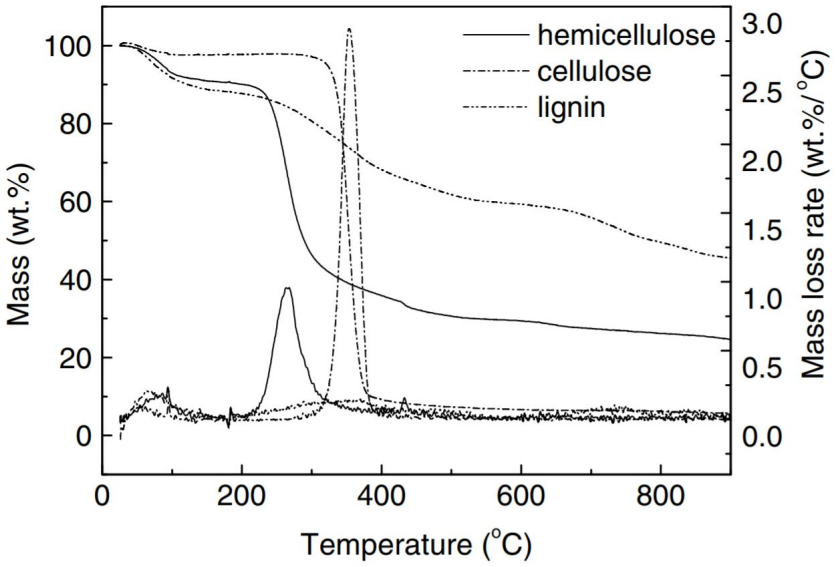

Figure 2.14: Pyrolysis curves of hemicellulose, cellulose and lignin in TGA [16].

2.1.3 Flax Fibres

Natural fibres have the advantages of being renewable, biodegradable and recyclable. In addition, they can form light composites offering competitive strength-to-weight ratio compared to mineral-based fibres. They also offer CO_2 emission reduction. Several studies have already examined lignocellulosic fibres as promising substitutes of the synthetic fibres in polymeric composites [17, 57]. Flax fibres are one of the strongest natural fibres.

2.1.3.1 Structure and composition of flax fibre

Flax fibre is formed by a series of elementary fibres with a polyhedron shape overlapping. Those fibres are held by a matrix consisting mainly of pectin and hemicellulose. Each of them is composed of a central hollow cavity called *lumen*, a very thin primary cell wall and a secondary cell wall (see Figure 2.15). The size and the shape of the lumen depends on the fibre's source and on the thickness of the cell wall. Elementary flax fibre's diameter is typically of $10 - 15\mu m$ compared to $35 - 150\mu m$ for technical flax fibre's diameter [6, 17, 57]. Flax fibres also contain cellulose, lignin, water solubles, moisture, fat and wax. The fibre's proportion of those components depends on the source, the age of the fibre and the extraction conditions [6].

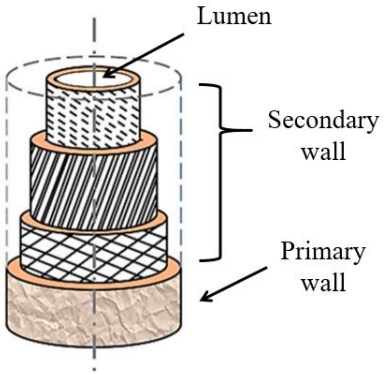

Figure 2.15: Structure of an elementary flax fibre [17].

2.1.3.2 Characteristics and properties of flax fibre

The presence of the lumen decreases the bulk density of flax fibre.
Due to its high cellulose content, flax exhibits a high tensile strength even if an exact correlation can not be established because of the complex structure of natural fibres. Properties of fibres can vary widely depending on the age, the extraction technique, the source, the moisture content, etc leading to high heterogeneity. The wax content affects the wettability and the adhesion of the fibre while the lignin content influences its morphology, structure and properties [6]. The Table 2.6 presents several flax fibre's properties.

Table 2.6: Flax fibre's properties [6].

Density ρ $[g/cm^3]$	Tensile strength σ $[MPa]$	Young's modulus E $[GPa]$	Elongation at break ε [%]
1.50	345-1100	27.6	2.4-3.2

2.1.4 Epoxy resin

Epoxy resins contain at least one epoxy groups per molecule on average. An epoxy group consists of an oxygen atom bridging two adjacent carbon atoms forming an epoxide ring. When this functionnal group is an end-group, it possess the chemical structure shown in Figure 2.16. This ether has a form close to the one of an equilateral triangle which distinguish it from other ethers. This particular form implies strong stresses and the cycle can open in the presence of an nucleophile; due to the difference of electronegativity between oxygen and carbon, carbon atoms are electrophile. According to the number of epoxide function possessed by the polymer, it is said to be bi-, tri-, tetra-functionnal [58, 59].

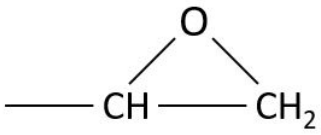

Figure 2.16: Chemical structure of end epoxy group [18].

Epoxy resins belong to the family of thermosetting materials which have a 3D network structure. Unlike thermoplastic resins that soften at high temperature and solidify reversibly during cooling, once the crosslinked 3D network is formed, the thermosetting material is insoluble and infusible [18, 58, 59].

2.1.4.1 Properties of epoxy resin

The properties of epoxy resins depend on the specifc combination of the type of resins and curing agents used. When epoxy resins react with suitable curing agent, the three-dimensional crosslinked structure formed gives them excellent mechanical properties, thermal stability and chemical resistance. They possess a high adhesivness to many substrates and they show low shrinkage. Because of those properties and ease of processing, epoxy resins are used in a wide range of fields. Unfortunately, due to the high-crosslinking density, epoxy resins are, at room temperature, inherently brittle material with low fracture toughness and poor crack resistance [18, 58, 60]. Poor crack resistance and brittle behavior limit their structural application. Indeed, the curing reaction decreases the chains mobility and induces a local stresses concentration. Therefore, they present low stress and strain at break.

2.1.4.2 Crosslinking agent (hardener)

For single-component epoxy resins which harden under heat, the prepolymer and the hardener are already mix and degas while multi-component resins need to be mixed with a crosslinking agent, also called hardener to promote polymerisation under heat. The curing agents control the epoxy resin curing reaction. The curing reaction induces irreversible changes in the epoxy resin leading to the formation of a tri-dimensionnal network [18, 59].
Curing agents are small molecules with low viscosity. There are several types of hardeners such as amines type, alkali type or anhydrides. The choice of one compared to another depends on the desired physical and chemical properties, on the polymerisation conditions and on the processing methods [18, 58].
One important step is the determination of the dosage of curing agent needed for curing. Knowing the resin's weight containing exactly one mole of epoxy group and the stoechiometric ratio between the resin and the curing agent allow to determine the amount of curing agent needed.
Solvents, plastifiers or diluents can be added to facilitate processing or modify properties.

2.1.4.3 Curing mechanism/reaction

The Figure 2.17 describes schematically the reticulation of a thermoset resin. The mechanism of such reaction differs according to the type of curing agent used. In addition, the T_g of the system and reticulation kinetics are influenced by the molecular structure of the curing agents [18, 19].
In the case of curing with an amine type curing agent, the mechanism includes three steps.

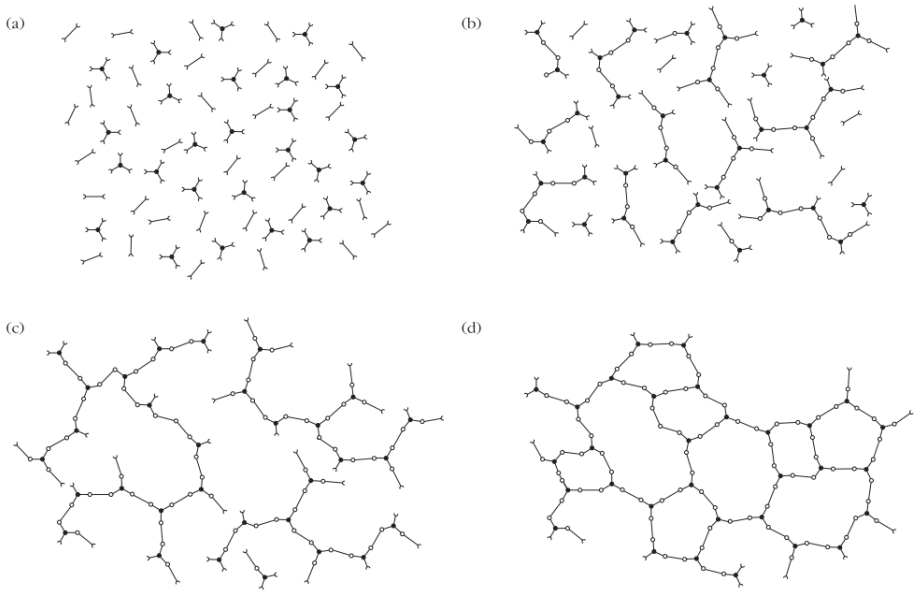

Figure 2.17: Bidimensionnal scheme of the curing of thermosetting resin. (a) unreacted components; (b) linear growth and chain branching; (c) gel formation; (d) fully crosslinked material [19].

Reaction of epoxide group with amines

First, the epoxide group of the resin reacts with the primary amine of the curing agent to form a secondary alcohol and a secondary amine. Indeed, the less crowded carbon of the epoxy function is an electrophile due to the non-biding electrons on the oxygen and the nitrogen of the amine is a nucleophile because of its non-binding electrons. The epoxy cycle thus opens due to this nucleophilic attack of the nitrogen on the carbon, creating a positive charge on the nitrogen and a negative charge on the oxygen. This negatively charged oxygen will then extract an hydrogen coming from the amine.

The secondary amine in turn reacts with an epoxide group to produce a tertiary amine and two secondary alcohols [19, 58].

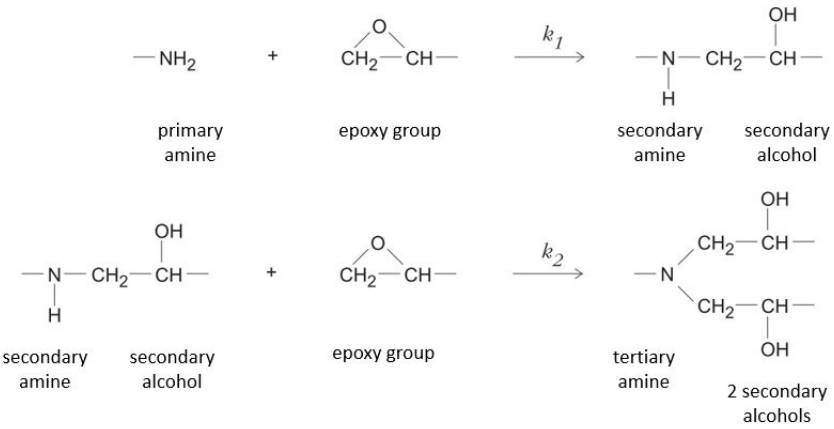

Figure 2.18: Chemical reactions taking place during curing [19].

Network formation

If the curing agent contains two amine functions, addition of epoxy group on the second amine group occurs. Quickly, a highly crosslinked network is formed.

2.1.4.4 TTT diagram

Different physical phenomenons occur during the reticulation reaction: the gelation, the vitrification and the degradation.
Time-Temperature-Transformation diagram or TTT diagram of thermoset shows the occurence of the different phenomenons occuring during curing. Furthermore the TTT diagram presents the states of a polymer and the critical temperatures associated to the transformation. An example of such diagram is shown in Figure 2.19 [19, 58, 59]. Full curing implies that the network is completely reticulated and corresponds to the time for which T_g reachs T_g^∞ for each curing temperature.

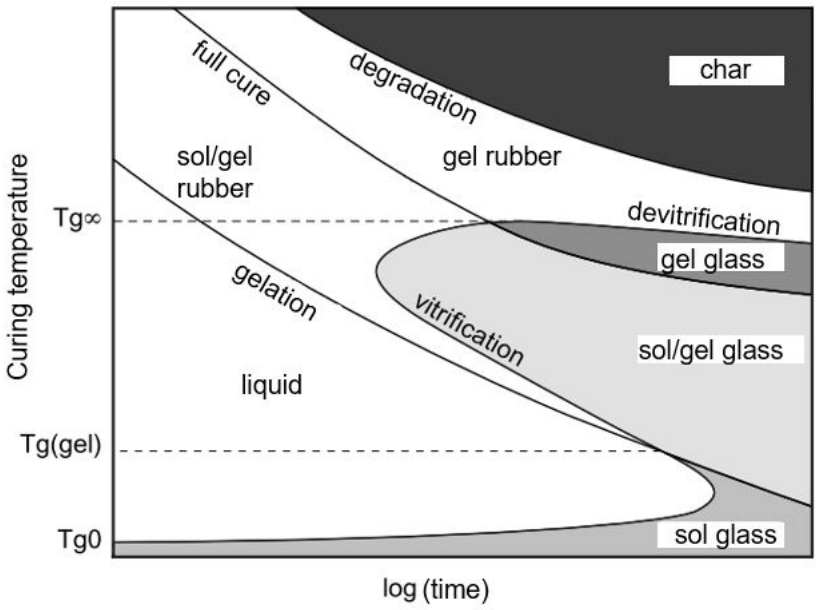

Figure 2.19: TTT diagram, showing the states of the polymer and the critical temperatures: T_{g0} the initial glass transition temperature, $T_{g(gel)}$ the intersection between vitrification and gelation and $T_{g\infty}$ the maximum glass transition achievable [19].

Gelation

Gelation is irreversible transformation during which the viscous, soluble and fusible liquid resin transfroms into a rubbery system composed of a insoluble viscoelastic gel and a soluble fraction called sol. The creation of an infinite unimolecular network is at the origin of this gelation and induces a sudden increase of viscosity [19, 58, 59].

Vitrification

Vitrification is the transformation of a liquid or rubbery state to a vitreous (or glassy) state. The vitrification occurs when the glass transition temperature T_g of the gel reaches the curing temperature. The reaction kinetics, controlled by the diffusion, is slow down due to the vitrification; the chain mobility is reduced because of the molar mass increase of the system. By increasing the temperature above T_g, devitrification can occur and reticulation can proceed further [19, 58, 59].

Degradation

Thermal degradations occur at elevated temperature and can hinder curing. Such

reactions lead to the formation of char which increases T_g due to densification or volatilization of low molar mass plastizicers [19, 58, 59].

2.1.4.5 Bio-sourced resin

More than 90% of petrochemical epoxy resins use usually bisphenol A (BPA) as precursor because its aromatic ring confers good thermal resistance to epoxy networks. BPA exhibits several negative health effects. Indeed, it is known to be an endocrine disruptor that mimic the body's own estrogen hormones [1, 61]. Endocrine disruptor can lead to negative health effects including alterations in immune and reproductive systems accompanied by modification in brain chemistry. In addition, while exhibiting advantageous properties, petrochemical based resins present significant drawbacks concerning biodegradability, energy consumption (fossil energy), health issues and initial processing cost [1, 20]. Therefore, the substitution of petroleum by vegetable oils as alternative feedstock has been studied by several researchers [20]. Available in large quantities, vegetable oils are the most abundant and the cheapest bioligical feedstock.
Multiple studies try to replace BPA by compound derivated from soybean oil, cardanol (carshew nut), furan (from cellulose and hemicellulose), rosin (from coniferous tree), lignin, itaconic acid, gallic acid, vanillin, isosorbide, cinnamic acid, catechin, eugenol or sugar [1, 62].

2.1.4.6 Bio-sourced epoxy resin

Vegetable oils are mainly composed of triglyceride molecules (or triacylglycerol, TAG): glycerol is attached to three fatty acid chains of unsaturated and saturated fatty acids (see Figure 2.20). Fatty acids from vegetable oils contain a large variety

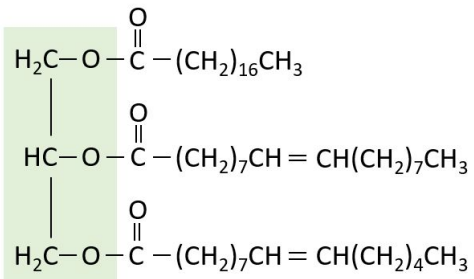

Figure 2.20: Structure of a typical triglyceride molecule [20].

of unsaturations sites ($C-C$ double bonds) which can be epoxidized. Epoxidation

can be performed by conventional chemical treatment, using acid ion exchange resin (AIER), enzymes, metal catalyst, ... The epoxidized vegetable oils are very attractive due to low cost and renewability. Indeed, plant oils are a popular choice for use in thermoset resins due to the abundance of carbon-carbon double bonds as those provide useful sites where polymerization can occur. Vegetable oils can be transformed in three different ways [18, 20, 21]:

- through direct polymerisation of the double bonds present in the triglycerides;
- through transformation of the double bonds into functional groups that can be polymerised;
- through transformation of oils into simple fatty acids or diglycerides that can serve as base monomers for polymer synthesis.

Soybean oil Soybean oil is one of the cheapest renewable product in the world. Epoxidized soybean oils (ESO) are commercially available and attractive for the replacement of petroleum-based polymers. However soybean oil based products possess long aliphatic chains resulting in lower stiffness and mechanical properties compared to petrochemical polymers. To overcome those drawbacks, renewable/non-renewable products blends are made to obtain good properties. Nevertheless, it is important to note that soybean intensive cultures have a terrible impact for the primary forests of South America [21, 62].

Linseed oil Linseed oil contains many of the following fatty acid chains: oleic acid, linoleic acid, and a-linolenic acid (see Figure 2.21) and is the most commonly epoxidized oil due to the surplus of double bonds available in the linolenic acid chains. Epoxidized linseed oil (ELO) are combined with hardeners such as dicarboxylic acids or anhydrides to creat highly crosslinked networks and obtain thermally and mechanically stable materials [21].

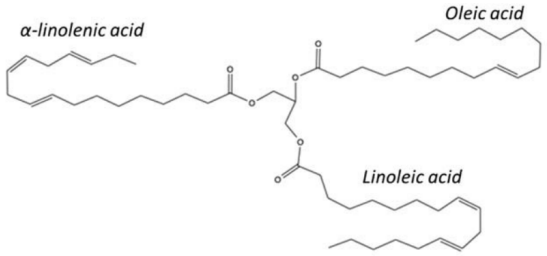

Figure 2.21: Representative structures of linseed oil [21].

Karanja oil Karanja oil is derived from the seeds of the karanja tree. The karanja tree grows across the coasts and river banks of Japan, India and Sri Lanka. The progress of industrial uses of karanja oil is not so advanced as for canola oil. However karanja oil can be epoxidized with sulfuric acid using acetic acid and hydrogen peroxide [21, 62].

Saccharides Saccharides or carbohydrates are the most common source of energy in most plants and animals and is inexpensive. Those compounds contain oxygen, hydrogen, and carbon. They possess hydroxyl groups allowing the formation of epoxy groups [21, 62].

Isosorbides The sugar-derived molecule isosorbide is water soluble and nontoxic. Isosorbide is a rigid organic diol with similar strucutre of bisphenol-A (BPA) (see Figure 2.22). It is an interresting molecule to replace BPA in epoxy polymers since it does not present endocrine disrupting effect.

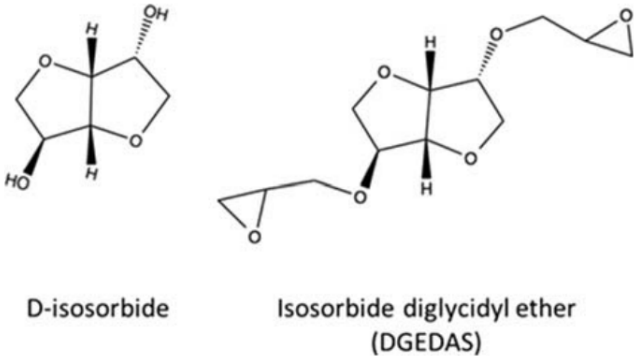

Figure 2.22: Structures of D-isosorbide and its epoxidized form DGEDAS [21].

To make an epoxy resin monomer with similar properties of diglycil bisphenol-A, isosorbide react with glycidyl ether or allyl ether to form a crosslinked network [21, 62].

Cardanol Cardanol is obtained from anacardic acid extracted from cashew nut shell liquid (see Figure 2.23). It naturally contains phenol and is therefore an excellent substitute in the preparation of petroleum phenol-based epoxy resins [21, 62].

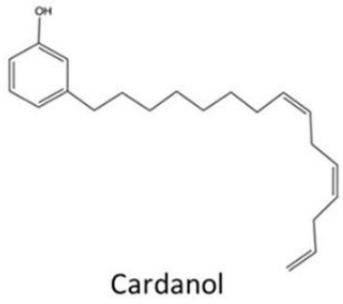

Figure 2.23: Cardanol is a derivative of cash nut shell liquid.

Lignin and lignin derivatives As already said before, lignin is highly abundant and has aromatic functionality (Figure 2.13). It shows attractive properties such as low weight and biodegradable nature. Lignin has been considered in the literature as an alternative of bisphenol-A (BPA) in the production of bio-based epoxy resins due to its aromatic structure with hydroxyl, carboxylic and phenolic groups which can react easily with epichlorohydrin [21, 62, 63].

Bio-based epoxy resins can also be synthesized from itaconic acid, rosin, furan, gallic acid, vanillin, cinnamic acid, catechin, eugenol, ...

2.1.4.7 Bio-sourced curing agent

Popular curing agents include amines, amides, hydroxyls, acid anhydrides, phenols, and polyphenols as shown in Figure 2.24. Usually most of the curing agents used are petroleum-based. However numerous bio-sourced curing agents have been developed over the past years. Bio-sourced hardeners are synthesized from modified plant oil, imidoamine from rosin and tung oil, bio-based acid (citric acid) and anhydride, bio-based phenol, lignin, rosin acid and terpenes [21, 62].

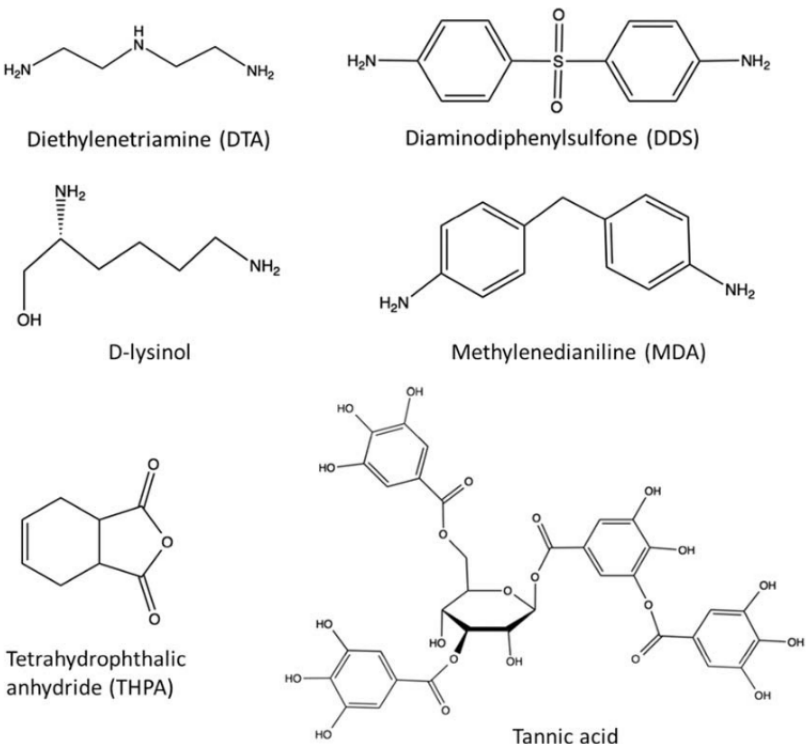

Figure 2.24: Structures of curing agents: diethylenetriamine (DTA) known to be toxic; diaminodiphenylsulfone (DDS); D-lysinol; methylenedianiline known to be toxic; tetrahydrophthalic anhydride (THPA); and tannic acid which is a natural polyphenol [21].

2.1.5 Thermodynamics of polymer blends

To improve the properties of polymer, one can make a polymer blend. In this case the obtained morphology plays a dominant role. To obtain a synergistic effect, the compatibility between the two polymers of the blends needs to be increased and the morphology of the blend needs to be optimised.
Polymers blends can be miscible when the system obtained is monophasic, or immiscible when at least two phases of different composition are present. Between these two states, different levels of miscibility can be obtained as a partial miscibility.

This part mainly based on [22] will describe briefly the polymer blend's thermodynamics, the miscibility conditions and the different morphologies that can be obtained.

2.1.5.1 Miscibility conditions

In most cases polymer blends are immiscible. This phenomenon can be explained by considering the free energy of mixing ΔG_m:

$$\Delta G_m = \Delta H_m - T\Delta S_m \tag{2.9}$$

Where ΔH_m is the enthalpy of mixing, ΔS_m the entropy of mixing and T the temperature. ΔG_m, ΔH_m and ΔS_m express respectively the difference of free energy, enthalpy and entropy after and before mixing.

As any system evolves spontaneously towards a decrease of its free energy, one necessary condition of miscibility is that $\Delta G_m \leq 0$. In other words in order for the system to be miscible ΔG_m must be negative. Otherwise the system reduces its free energy by phase separating.
However looking at the shape of g_v^0 and g_v the volume free energies before and after mixing represented at Figure 2.25, one can see that the necessary condition is not sufficient. Even if $\Delta g_{v,m} = g_v - g_v^0$ is always negative, in the grey zone the system phase separates in two phases of compositions ϕ_a and ϕ_b. The minimum volume free energy of the system is located between ϕ_a and ϕ_b on the common tangent to the local minima of g_v and thus after phase separation the free energy is reduced.

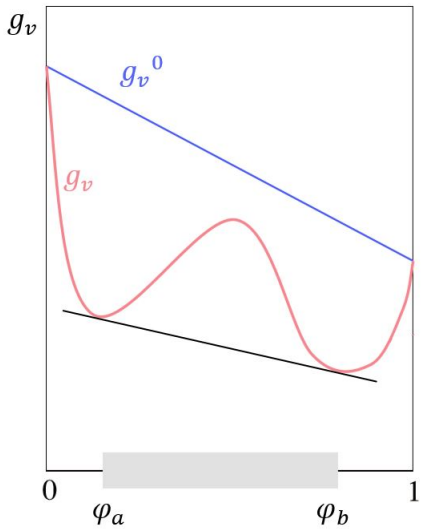

Figure 2.25: Evolution of g_v^0 and g_v as a function of the volume fraction of one of the component [22].

In fact if the curvature of $\Delta g_{v,m}$ is positive as depicted in Figure 2.26, the system is either stable or metastable whatever the absolute value of $\Delta g_{v,m}$. Hence in this

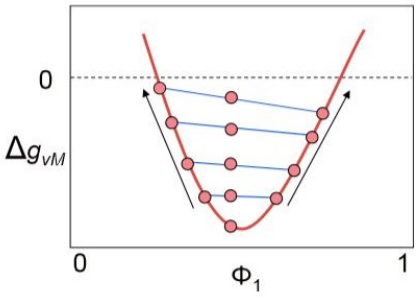

Figure 2.26: Positive curvature case - $\Delta g_{v,m}$ as a function of the volume fraction of one of the constituents [22].

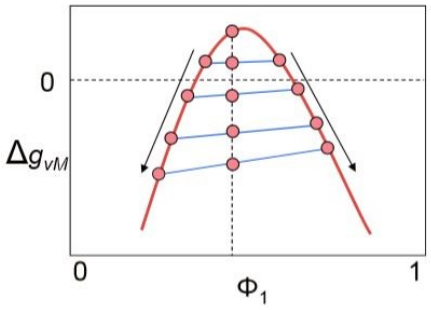

Figure 2.27: Negative curvature case - $\Delta g_{v,m}$ as a function of the volume fraction of one of the constituents [22].

situation the system cannot reduce its free energy by demixing by small fluctuations : $\frac{\partial^2 g_v}{\partial \phi^2} > 0$ if g_v^0 is linear in ϕ. On the contrary if the curvature of $\Delta g_{v,m}$ is negative (Figure 2.27), the system can reduce its free energy by demixing by small fluctuations whatever the absolute value of $\Delta g_{v,m}$. In this case the system is stable and if g_v^0 is linear in ϕ : $\frac{\partial^2 g_v}{\partial \phi^2} < 0$.

In brief the **necessary** and **sufficient miscibility condition** is expressed as:

$$\Delta G_m \leq 0 \text{ and } \frac{\partial^2 g_v}{\partial \phi^2} \geq 0 \tag{2.10}$$

2.1.5.2 Enthalpy and Entropy of mixing

As the sign of the free energy ΔG_m is decisive for the polymer blend miscibility, it is interesting to look at the entropy of mixing ΔS_m and the enthalpy of mixing ΔH_m: $\Delta G_m = \Delta H_m - T\Delta H_m$.

ΔS_m is expresses as the sum of a combinatorial mixing entropy ΔS_m^C and a non combinatorial mixing entropy ΔS_m^{NC} : $\Delta S_m = \Delta S_m^C + \Delta S_m^{NC}$. On one hand the combinatorial entropy of mixing is linked to the number of possible conformations for macromolecules and disorder. Indeed chain connectivity in macromolecules drastically reduces the number of configurations with respect to the small molecules. ΔS_m^C is given by the Flory-Huggins equation (Equation 2.11). Since the number of possible arrangements of macromolecules decreases when the length of the chain increases as shown in Figure 2.28, ΔS_m decreases when the length of the chains increases which makes a negative ΔG_m less probable. However the contribution of ΔS_m^C to ΔS_m is small [22].

$$\Delta S_m = -kN\left[\phi_A \ln \phi_A + \phi_B \ln \phi_B\right] \tag{2.11}$$

On the other hand the non combinatorial entropy ΔS_m^{NC} takes into account compressibility and thermal expansion of polymers and has a larger contribution to ΔS_m than ΔS_m^C. The non combinatorial entropy is negative and can be calculated with the help of a state equation [22].

Consequently ΔG_m increases with the temperature because the entropy favors demixing at high temperature. This phenomenon explains the shape of phase diagrams.

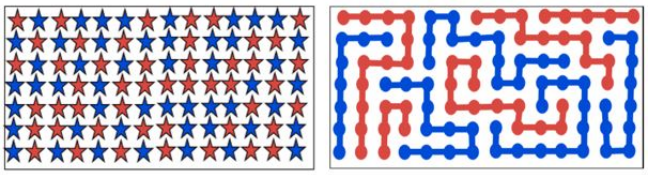

Figure 2.28: Representation of possible configurations for (a) small molecules and (b) macromolecules [22].

The mixing enthalpy ΔH_m results from an "exchange" term and originates from the intermolecular interactions. Those interactions can be either non-specific ones i.-e. that they exist between all types of macromolecules segments such as Van der Waal forces or specific ones that only exist between specific types of spegments such as hydrogen-bonds. $\Delta H_m^{non\ specific}$ is positive and thus non-specific interactions never favor mixing while specific interactions favor mixing or not depending if $\Delta H_m^{specific}$ is negative or positive [22].

Frequently the mixing enthalpy ΔH_m is positive and the system is said to be endothermic. Polymer blends demix at high temperature and are usually poorly miscible (or immiscible) due to a positive enthalpy of mixing and a small mixing entropy.

The free energy of mixing is generally expressed by the Flory-Huggins equation (Equation 2.12):

$$\frac{\Delta G_m}{N_s kT} = \chi_{12}\ \phi_1\phi_2 + \left[\frac{\phi_1}{X_1}\ln\phi_1 + \frac{\phi_2}{X_2}\ln\phi_2\right] \tag{2.12}$$

Where N_s is the number of sites, k the Boltzmann constant, ϕ_i the volume fraction of polymer i, X_i the degree of polymerisation and χ_{12} the Flory-Huggins parameter.

This Flory-Huggins parameter is given by:

$$\chi_{12} = \chi_{12_{enthalpic}}^{non\ specific} + \chi_{12_{enthalpic}}^{specific} + \chi_{12_{entropy}}^{non\ combinatorial} \tag{2.13}$$

According to previous considerations:

- $\chi_{12_{entropy}}^{non\ combinatorial}$ varies as ΔS_m^{NC}, is positive and increases with the temperature;
- $\chi_{12_{enthalpic}}^{non\ specific}$ is positive;
- $\chi_{12_{enthalpic}}^{specific}$ can be either positive or negative;
- $\chi_{12_{enthalpic}} = \chi_{12_{enthalpic}}^{specific} + \chi_{12_{enthalpic}}^{non\ specific}$ is inversely proportionnal to the temperature and can be positive or negative.

The Equation 2.12 can now be written as:

$$\frac{\Delta G_m}{N_s kT} = \chi_{12_{enthalpic}}\ \phi_1\phi_2 + \chi_{12_{entropy}}\ \phi_1\phi_2 + \left[\frac{\phi_1}{X_1}\ln\phi_1 + \frac{\phi_2}{X_2}\ln\phi_2\right] \tag{2.14}$$

Where the first term is the enthalpic contribution, the second one the entropic contribution and the third one is negative and temperature independent.

2.1.5.3 Phase diagrams thermoplastic - thermoset (TP-TS)

Phase diagrams present the domains where the system is either miscible or immiscible. Two curves are distinguished: the binodal cuvre and the spinodal curve. Those curves mark regions with different kinetics of phase separation. Moreover the form and position of those curves depend on molecular masses ratio of the two polymers present in the system. In the domains where the solution of polymers is stable, only one phase exists. On the contrary in domains where the solution is unstable, the system is immiscible and phase separation occurs. In the regions where the solution is metastable, an energy barrier exists and large fluctuations of composition happen [22].
Different cases exist according to the absolute value of the enthalpic term in Equation 2.14:

1. If the term is negative, the blend of the two polymers is only possible at low temperature because above a certain temperature, demixing is unavoidable despite the favourable enthalpic interactions. Indeed the free energy of mixing becomes positive above this temperature. In this case the phase diagram (Figure 2.29) presents a lower critical solution temperature (LCST). The LCST corresponds to the critical temperature below which the components are miscible whatever the composition.

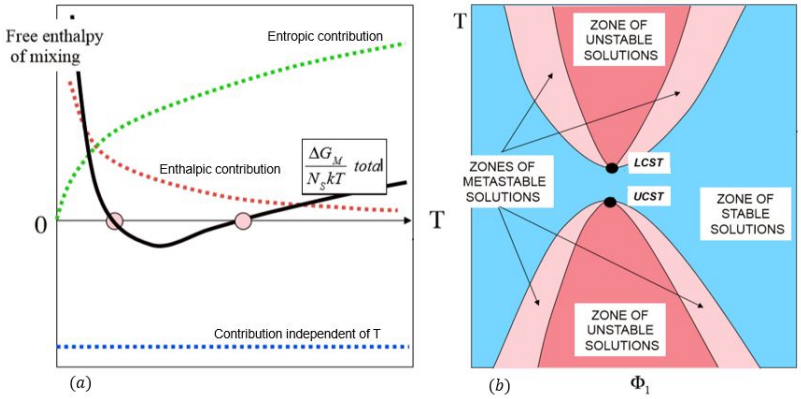

Figure 2.29: (a) Evolution of the free energy of mixing with the temperature when $\chi_{12,enthalpic} < 0$. (b) Temperature - composition diagram when $\chi_{12,enthalpic} < 0$ [22].

2. If the term is positive, demixing occurs inevitably at low and high temperatures. Depending on the equilibrium between entropic and enthalpic terms, a region of miscibility can exist at intermediate temperatures due to a negative free energy of mixing in this range of temperatures. In this case the phase diagram (Figure 2.30) presents a LCST and an upper critical solution temperature (UCST).

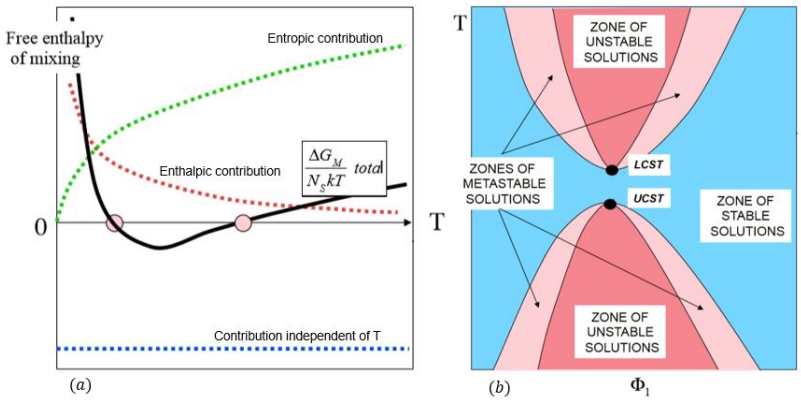

Figure 2.30: (a) Evolution of the free energy of mixing with the temperature when $\chi_{12,enthalpic} > 0$. (b) Temperature - composition diagram when $\chi_{12,enthalpic} > 0$ [22].

3. There is a limiting case where the value of the term is large and povitive. This is the most common situation. Figure 2.31 illustrates the phase diagram for this case.

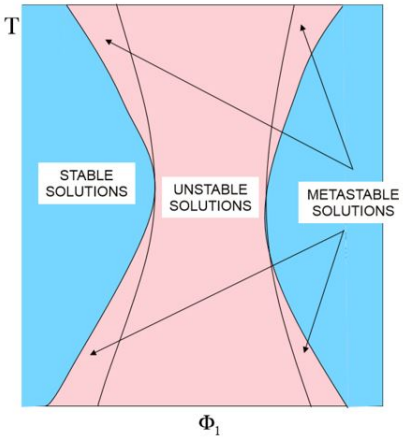

Figure 2.31: Temperature-composition diagram when $\chi_{12,enthalpic} >> 0$ [22].

The discussion above is valid for blends of two thermoplastic polymers or thermoplastic/thermoset blends. Nonetheless in the case of TP/TS polymer blends, other parameters need to be taken into consideration.

During cross-linking of the epoxy/TP composites, the TP is firstly required to be initially miscible with the epoxy monomers for fine dispersion. For thermoplastic-thermoset blends, phase diagrams change with the crosslinking rate as shown in Figure 2.32. First the blend is miscible before crosslinking and then beyond a certain conversion of thermoset, phase separation occurs. The system is in the biphasic domain and there is a resin-rich phase and a thermoplastic-rich phase. Before crosslinking the molecular mass of the resin is small. During crosslinking the molecular mass increases leading to an decrease of ΔS_m (being less and less favorable to miscibility) and thus an increase of ΔG_m.

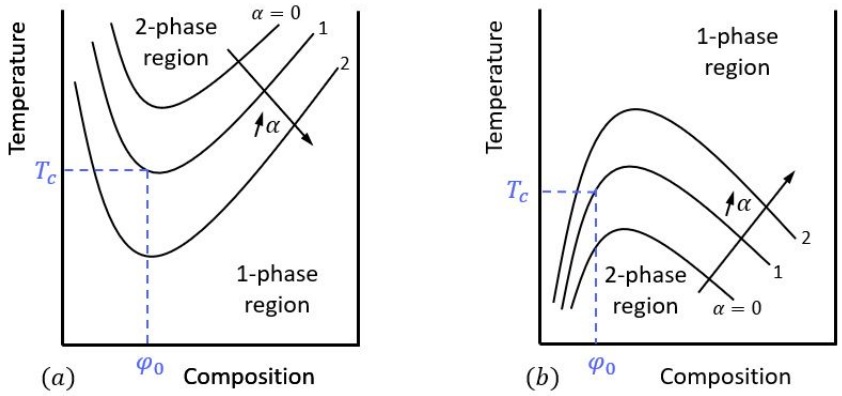

Figure 2.32: Evolution with the crosslinking rate α of temperature-composition diagram in the case of TP-TS blend (a) for a LCST behaviour and (b) for a UCST behaviour [22].

2.1.6 Phase separation and Morphology

When the polymer blend is immiscible and two phases exist, different morphologies can be obtained. They are reprensated in Figure 2.33. The resulting morphology depends on several parameters such as the composition or the viscosity ratio.

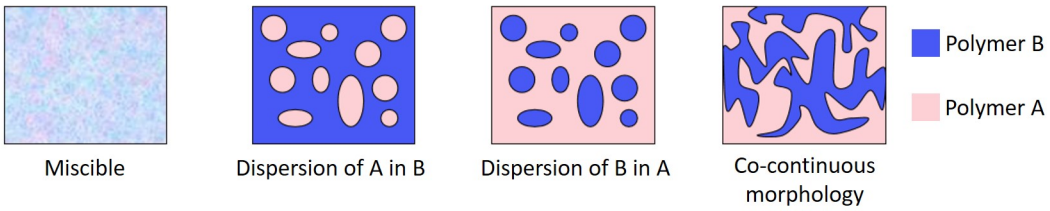

Figure 2.33: Different morphologies for a binary polymer blend [22].

2.1.6.1 Phase separation mechanisms

The thermodynamic equilibrium state is rarely achieved owing to very slow diffusion. The diffusion coefficient D is proportional to the second derivative of the free energy G which means that the sign of D depends on the curvature of G. Consequently one can distinguish two mechanisms by which the components of a solution can phase separate according to the region of miscibility in which the system is: demixing by *nucleation and growth* in the metastable region and demixing by *spinodal decomposition* [22].

1. Nucleation and growth occurs when $\frac{\partial^2 G}{\partial \phi^2} > 0$, the diffusion is normal and the diffusion coefficient is positive: $D > 0$. The new phases appear by nucleation and the nuclei starts to grow when they reach a critical size. As shown in Figure 2.34 the system phase separates in two widely separated compositions (close to equilibrium). This is due to the existence of an activation energy barrier for the nucleation of the « far away » composition. The morphology is usually a dispersed nodular one and coarsens with time [22].

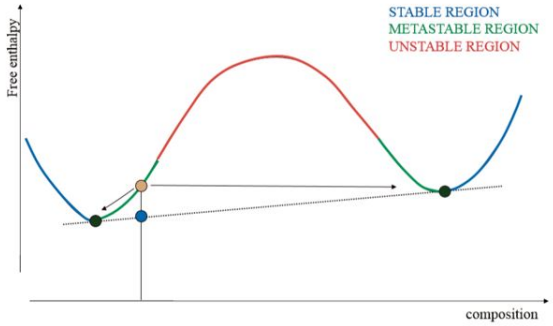

Figure 2.34: Compositions evolution during demixing by nucleation and growth [22].

2. Spinodal decomposition occurs when $\frac{\partial^2 G}{\partial \phi^2} < 0$, the diffusion is abnormal and the diffusion coefficient is negative: $D < 0$. The initial composition is in the unstable region therefore the system demixes in two progressively separated compositions (see Figure 2.35). There is no activation energy for phase separation. The new phases appear by gradual increase of "compositional contrast" as illustrated by Figure 2.36. The morphology is usually co-continuous [22].

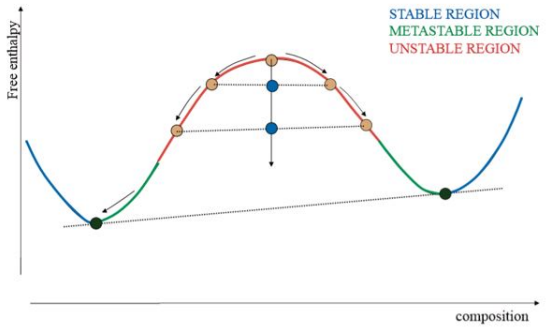

Figure 2.35: Compositions evolution during demixing by spinodal decomposition [22].

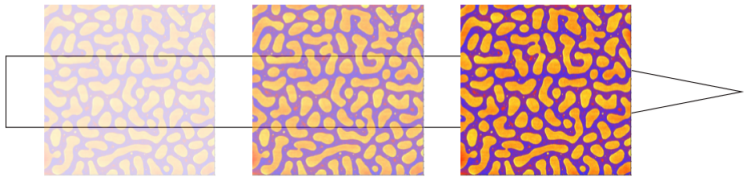

Figure 2.36: Illustration of the increase of "compositional contrast" during spinodal decomposition [22].

2.1.6.2 Morphology

The way the polymer blend is produced in other terms the processing steps, play an significant role in the resulting morphology. During injection moulding or extrusion polymers are sheared and the obtained morphology is not at equilibrium but is quenched.
In the case of a dispersed morphology, blend properties depend on which phase is the dispersed one and which phase is the continuous one. Two parameters determine which phase is the continuous one; the volume ratio of phases $\frac{f_1}{f_2}$ and the viscosity ratio $\frac{\eta_1}{\eta_2}$. Indeed the phase with the higher volume fraction tends to form the continuous phase. Furthermore the less viscous phase tends to form the continuous phase [22]. The simplest used model consists to compare the two ratios:

- If $\frac{\eta_1}{\eta_2} < \frac{f_1}{f_2}$ then the phase 1 is the continuous one;
- If $\frac{\eta_1}{\eta_2} < \frac{f_1}{f_2}$ then the phase 2 is the continuous one;
- If $\frac{\eta_1}{\eta_2} \approx \frac{f_1}{f_2}$ then the two phases are continuous.

The size of nodules is in turn the result of a dynamic equilibrium between shear forces that deform the droplet of polymer during the process and the interfacial energy opposed to the deformation.
According to previous studies, TP loadings and curing temperature, i.e., volume fraction and quench depth, are the key factors to construct the final morphology.

2.1.7 Thermal and mechanical properties of polymer blends

2.1.7.1 Transition glass temperature

For non crystalline polymers, the glass transition temperature T_g is may-bye the most important parameter which determines the application of the polymer. T_g determines indeed the mechanical behavior of polymers. At a temperature above its

T_g, an amorphous polymer is in a molten and rubbery state. When the temperature decreases below its T_g, a transformation from this molten state to a hard and tough form occurs. This transformation is accompanied by a significant increase of Young's modulus and thus of stiffness. Actually the glass transition proceeds in a relatively small range of temperatures and the glass transition temperature T_g corresponds to the average temperature when the glass transition occurs [22, 41]. Polymer materials used below their T_g are called vitreous polymers and belong to the organic glasses group. When they are used above their T_g, crosslinking is needed for those polymers in order for them not to flow: they are elastomers [41]. The internal structure of the amorphous polymer does not change during the glass transition transformation: the polymer stays liquid. As a matter of fact when performing a scattering X-rays analysis, the spectrum shows broad halos which indicates an amorphous state. Thus the increase of stiffness is not due to crystallisation of the polymer but it becomes hard and is not able to flow anymore [41].
Occurrence of glass transition can be explained by considering the presence of free volume which allows molecular movements. This excess volume comes from the irregular positioning of atoms in amorphous polymers and results in lower densities compared to a crystal of the same material if it exists [41]. When cooling a polymer melt, the amount of free volume decreases progressively by small scale molecular motion. This decrease makes segmental movements more and more difficult and the progressive elimination of free volume results in a state where molecular movements are so slow that the material effectively freezes. The material keeps an excess of free volume compared to the liquid at equilibrium. The glass transition is thus a kinetic transition and not a thermodynamic one [41]. In brief, the glass transition intrinsically results from increased hindrances to motion because of a decrease of free volume.

2.1.7.2 Measurement methods of transition glass temperature

The glass transition approaches a second order phase transition. Unlike first order thermodynamic phase transitions which experience abrupt changes in the first derivatives of the free energy such as the volume, the enthalpy and the entropy while the free energy remains continuous, it is the second derivatives of the free energy that sharply changes during glass transition. Moreover, such transition happens homogeneously throughout the sample, not through the process of nucleation and growth as in crystallization. T_g can thus be determined by the occurrence of second order abrupt changes. However, glass transition is not a thermodynamic transition because it is regulated by kinetics and thus the glass formed is not a stable phase [41].

Differential scanning calorimetry (DSC)

When performing DSC the amount of heat required to increase or decrease continuously the temperature of the sample compared to a reference is measured according to the evolution of temperature. Two different configurations exist. In the first one, the sample and the reference are placed in the same furnace and are heated at the same speed. In the second configuration, the two crucibles are placed in different furnace but are maintained at the same temperature. The heat flux is determined based on the electrical power needed. The specific heat c_p is a second derivative of the free energy therefore the plot of c_p as a function of the temperature shows an expected jump of specific heat c_p at T_g which allows to determine T_g [41].

$$c_p = -T\frac{\partial^2 g}{\partial T^2} \tag{2.15}$$

Dynamic mechanical analysis (DMA)

Dynamic mechanical analysis allows to test samples in different configurations such as torsion, shear or elongation. A sinusoidal deformation of small amplitude and controllable frequency is applied while controlling the temperature. According to the frequency of this variation, the material behaves as a liquid or a solid. This technique allows to measure the storage modulus E' representing the elasticity of the material and its ability to store energy and the loss modulus E'' or viscous modulus which measures the capacity of the material to dissipate energy. The damping factor $tan\ \delta = \frac{E''}{E'}$ is also calculated. T_g is determined as the temperature corresponding to the inflection point of the E' vs T curve which also corresponds to the maximum of the loss modulus E'' vs T. T_g can also be considered as the temperature corresponding to the maximum of the damping factor $tan\ \delta$ vs T curve [41].

For a binary blend, the ratio of damping factor peaks' heights corresponding to each phase can give information on the blend morphology [64].

2.1.8 Polymer blends

For a binary polymer blend, the resulting glass transition temperature(s) depend(s) on the miscibility of the blend, the glass transition temperature of the polymer-1 T_{g1} and the glass transition temperature of the polymer-2 T_{g2}.

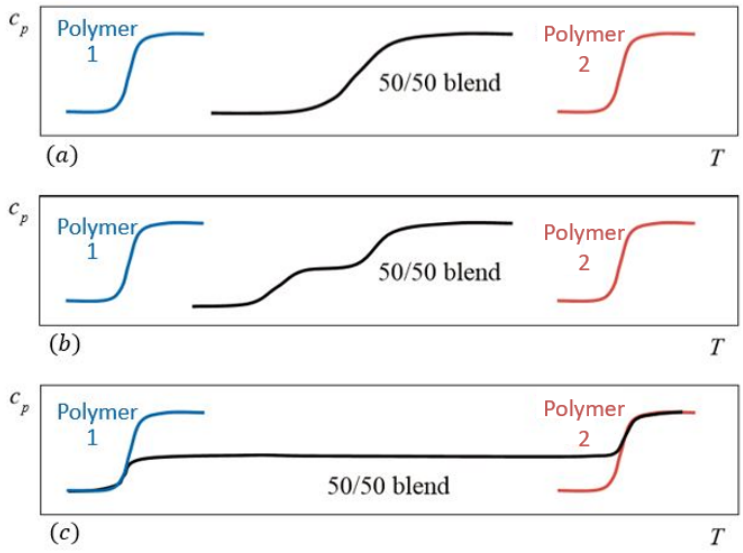

Figure 2.37: Representation of the glass transition temperature in the case of (a) a miscible blend (b) a partially miscible blend (c) an immiscible blend [22].

Miscible blends For a miscible blend with only one phase, a single often broadened glass transition temperature T_g is observed at intermediate location with respect to the T_g of components as shown in Figure 2.37(a). The Fox empirical Equation 2.16 can predicted this T_g:

$$\frac{1}{T_g} = \frac{w_1}{T_{g1}} + \frac{w_2}{T_{g2}} \tag{2.16}$$

Where w_i is the weight fraction and T_{gi} the glass transition of the component i [22].

Partially miscible blends In the miscibility gap two glass transitions closer and broader than those of the components are observed for partially miscible blends as represented in Figure 2.37(b). While outside of this miscibility gap, a single T_g is measured.

Immiscible blends For an immiscible blend, two glass transitions are observed at the same temperature T_{g1} and T_{g2} as the components glass transition temperatures as shown in Figure 2.37(c).

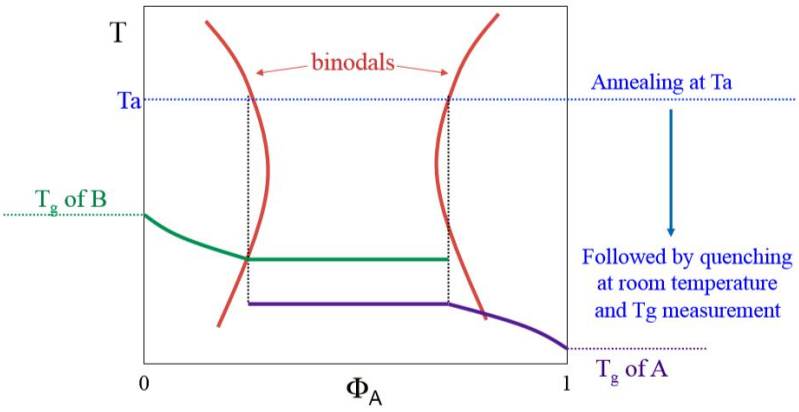

Figure 2.38: Evolution of the glass transition temperature of a partially miscible blend as a function of the composition [22].

2.1.9 Mechanical properties and Fracture mechanics

2.1.9.1 Mechanical characteristics from tensile test

During a tensile test, the force is measured and registered meanwhile the elongation increased until the specimen breaks. A sudden drop in force indicates break and implies the end of test. The measurement can also be stop when the force drops down by a chosen percent or at a chosen elongation. The elongation is measured by measuring probe. The displacement of the crosshead or gripping unit (generated by the tensile testing machine) is also registered [65, 66].
The reproducibility of the tensile test is a crucial parameter, therefore standard specimens are used. The general shape of polymeric specimen is a dumbbell (or dog-bone) shape as shown in Figure 2.39. The large shoulders can be readily gripped, while the gauge section has a smaller cross-section so that the deformation and failure can occur in this area. Indeed, the dumbbell feature is used to avoid the break of the specimen too close to the clamps (gripping units) [23, 65, 66, 67].

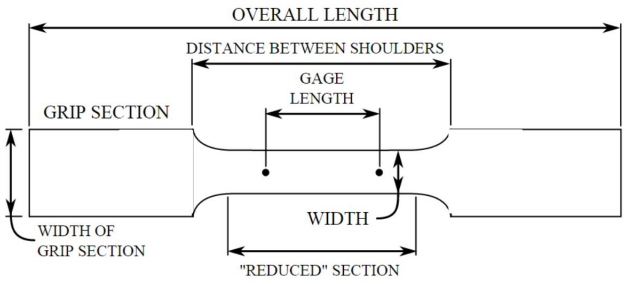

Figure 2.39: Typical tensile specimen, showing a reduced gauge section and enlarged shoulders [23].

For the given measurement conditions, the force-displacement ($F - \Delta l$) curve of the material is obtained as result of the tensile test. One can parametrise this curve to obtain a stress-strain ($\sigma - \varepsilon$) curve as shown on Figure 2.40. Engineering or normal stress σ_{eng} is obtained by dividing the measured force F by the initial cross-sectional area of the specimen A_0 (Equation 2.17) while the true stress σ_t experienced by the material is given by the ratio of the measured force F by the current cross-sectional area of the specimen A (Equation 2.18). The engineering or normal strain ε_{eng} is the ratio between δl the displacement between the knifes of the extensometer used and l_0 the initial length (see Equation 2.19) while the true strain ε_t is given by Equation 2.20 with l the current length of the specimen [27, 67].

$$\sigma_{eng}\,[MPa] = \frac{F}{A_0}\left[\frac{N}{mm^2}\right] \tag{2.17}$$

$$\sigma_t\,[MPa] = \frac{F}{A}\left[\frac{N}{mm^2}\right] \tag{2.18}$$

$$\varepsilon_{eng}\,[\%] = \frac{\delta l}{l_0} \times 100\left[\frac{mm}{mm}\right] \tag{2.19}$$

$$\varepsilon_t\,[\%] = ln\left(\frac{l}{l_0}\right) \times 100\,[\%] \tag{2.20}$$

If the current section A is not measured during the tensile test, the true stress and strain can be related to the engineering ones using volume conservation:

$$\sigma_t = \sigma_{eng} \times (1 + \varepsilon_{eng}) \tag{2.21}$$

$$\varepsilon_t = ln\,(\varepsilon_{eng} + 1) \tag{2.22}$$

One can consider that plasticity occurs at constant volume which is not the case in elasticity:

$$Al = A_0 l_0 \tag{2.23}$$

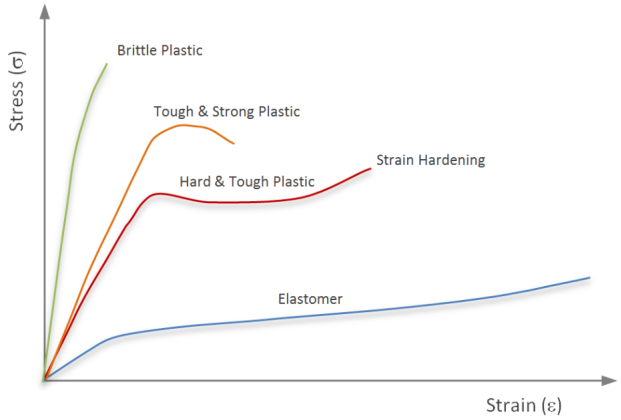

Figure 2.40: Tensile true stress-strain ($\sigma - \varepsilon$) curves for typical plastics [24].

From this stress-strain curve, the following mechanical properties can be extracted and calculated.

Elastic Properties: When a solid material undergoes a small stress, the bonds between atoms are stretched. Once stress is removed, bonds relax and the material returns to its original shape: stress induces a reversible deformation called an elastic deformation. In the elastic region (only elastic deformation appears), the Hooke's law describes the linear relationship between stress σ and strain ε (Equation 2.24) characterized by Young's modulus E and Poisson's ratio ν which gives the magnitude of the lateral contraction strain to the axial strain (Equation 2.25). ν is the negative ratio of the strain increment along one of the axes perpendicular to the elongation direction and the strain increment in the elongation direction in the linear part of the stress-strain curve [65, 67].

$$\sigma = E_t \varepsilon \tag{2.24}$$

$$\nu = -\frac{\Delta\varepsilon_n}{\Delta\varepsilon_l} \tag{2.25}$$

The elastic modulus E_t, expressed in MPa also called Young's modulus is the slope of the stress-strain curve in the interval of strain between $\varepsilon_1 = 0.05\%$ and

$\varepsilon_2 = 0.25\%$ according to ISO527 standard. It can be calculated in different way [65, 66, 67]:

- *Secant modulus* E_t given by the slope of the line connecting the ε_1 and ε_2 points of the $\sigma - \varepsilon$ curve (Equation 2.26);
- *Tensile modulus* E given by the slope of the regression line at least squares in the interval (Equation 2.27).

$$E_t\,[MPa] = \frac{\sigma_2 - \sigma_1}{\varepsilon_2 - \varepsilon_1} \tag{2.26}$$

$$E\,[MPa] = \frac{d\sigma}{d\varepsilon} \tag{2.27}$$

Tensile strength and Elongation at maximum force: The maximum tensile strength σ_{max} is the greatest stress a material can withstand without failing [68, 27]. It is given by the ratio of the maximum force F_{max} over the current cross section of the specimen A (Equation 2.28). According to ISO527 standard tensile strength must be calculated at the first local maximum of the tensile curve [67].

$$\sigma_{max} = \frac{F_{max}}{A} \tag{2.28}$$

$$\varepsilon_{max} = ln\left(\frac{l_{max}}{l_0}\right) \times 100\,[\%] \tag{2.29}$$

Elongation at maximum force ε_{max} is the strain at which tensile strength is reached and can be calculated with the Equation 2.29 where l_{max} is the elongated length of the reduced section of the specimen at maximum force and l_0 is the unloaded length of the examined part of the specimen [67].

Yield strength: The yield strength corresponds to the stress at which plastic deformation (or yielding) is observed to begin. From this point the material will elongate further without any further stress. Indeed, the yield strain coincides with the first point where there is an increase of strain without an increase of stress. In case of polymers, yield can be revealed by stress whitening (see Figure 2.41). Actually, for some polymers it does not occur, however for other materials neck formation can occur preceding 100% yield strain accompanied by structural transformation [66, 67]. Yield strength depends both on strain rate $\dot{\varepsilon}$ and temperature T as illustrated in Figure 2.42.

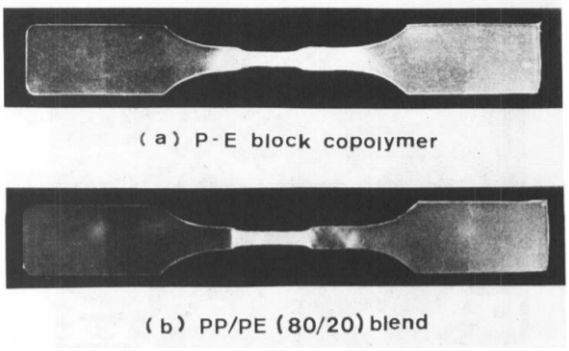

Figure 2.41: Stress-whitening phenomena for a bar of (a) P-E block copolymer and (b) 80/20 PP/PE blend [25].

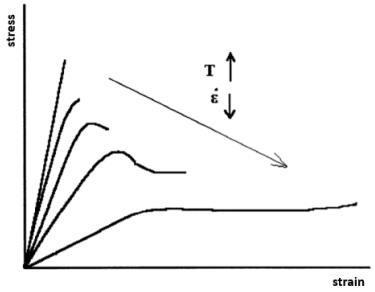

Figure 2.42: Dependence of mechanical response of polymers on the external conditions [26].

Breaking strength and Breaking strain: The strain at break can not be considered as the breaking strain on the $\sigma_{eng} - \varepsilon_{eng}$ because after the ultimate tensile stress, the specimen undergoes necking. As the stress localises itself, the strain becomes not uniform. The breaking strain is thus considered as the one on the $\sigma_{true} - \varepsilon_{true}$. As σ_{true} is calculated based on σ_{eng}, the true stress at breaking can not be obtained.
The elongation at break ε_b is the strain at the last registered point prior to the reduction of stress to a value lower than or equal to 10% of the strength when the breaking occurs before yielding [67]. The engineering strain at break ε_b is also given by the ratio between the difference of the elongated length at break l_b and the initial length l_0 of the reduced section over the initial length l_0 (Equation 2.31).

$$\sigma_b = \frac{F_b}{A} \tag{2.30}$$

$$\varepsilon_b = \times 100\,[\%] \tag{2.31}$$

2.1.9.2 Fracture mechanics

Fracture mechanics concerns crack propagation in materials in order to design components and processes avoiding later crack propagation. The aim of fracture mechanics is to answer a number of questions such as what is the maximal load that a material with a crack can sustain according to the crack's size or what is the maximum size of a crack that a material can handle to maintain its function. Fracture mechanics is truly important during designing because any material possesses defects or geometrical discontinuities as crack created during processing for instance [69].
The material toughness is a significant parameter and is defined as the material capacity to withstand the propagation of a crack. Toughness is usually weak for epoxy resins which are brittle. The final aim of this work was try to evaluate if the modification of a bio-sourced resin will enhance its toughness. When studying this property, the material is considered as elastic and linear according to the linear elastic fracture mechanics (LEFM). The crack produce a stress singularity in purely elastic solids. In fact the stress can not be infinite due to the occurence of non-linear mechanisms. However the non-linear zone can be small enough to apply LEFM principles [27]. LEFM theory considers a plane and straight crack perpendicular to the y-axis whose side is along the z-axis and which propagates along the x-axis as shown in Figure 2.43.

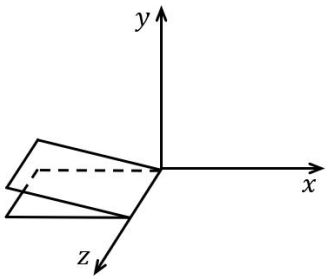

Figure 2.43: Definition of axis around a crack in LEFM.

Three different modes of crack opening exist as a function of the orientation of the applied forces and every configuration can be obtained by a linear combination of those three modes which are illustrated in Figure 2.44. In mode I, the crack undergoes a tensile force in the y direction. A shearing force is applied in the x direction in the (x,z) plan in mode II while the mode III corresponds to a shearing force in the z direction in the (x,z) plan [27].
The analysis considers a plane strain, that is the case for a very thick plate where the plastic zone is smaller than the plate's thickness. On the contrary a plane

stress situation is considered when the plate is very thin [27].

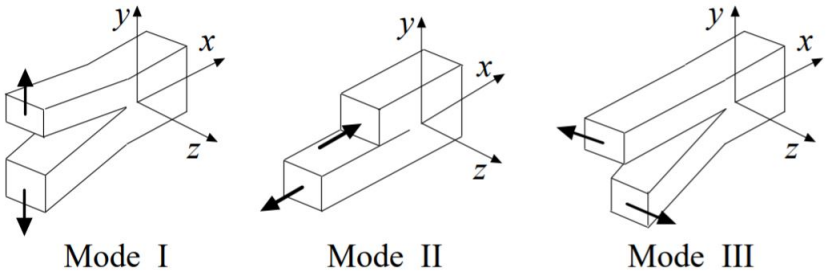

Figure 2.44: Definition of the three modes of crack opening [27].

2.1.9.2.1 Stress intensity factor K

A geometrical discontinuity as a crack lead to a non uniform stress distribution around it. Analytical solutions in LEFM can be derived for each opening mode. By considering polar coordinates r and θ, the stress in the case of mode I is given by:

$$\sigma_{ij}^{I} = \frac{K_I}{\sqrt{2\pi}}\ f_{ij}^{I}(\theta) + \sum_{n=2,\dots}^{\infty} C_n^I(K_I, a, geometry)\ r^{\frac{n}{2}-1}\ f_{nij}^{I}(\theta) \tag{2.32}$$

Where $i, j = r$ or θ, $f_{ij}^{I}(\theta)$ and $f_{nij}^{I}(\theta)$ are functions of θ, K_I and C_n^I are constants dependent on the geometry and the load.

Those analytical solutions indicate that the stresses near the crack are only influenced by one parameter called the stress intensity factor K. K depends on the load applied and the geometry, its units are $MPa\sqrt{m}$. The crack length is in fact the most important characteristic dimension influencing K. For instance for a crack of length $2a$ in an infinite plate submitted to a stress σ^{∞} in the perpendicular direction to the crack's plan, the stress intensity factor K^I is given by $\sigma^{\infty}\sqrt{a\pi}$ [27]. The general form of K is given by Equation 2.33, where Y is a non-dimensional factor that depends only on the geometry of the specimen:

$$K = \sigma^{\infty}\ Y\ \sqrt{a} \tag{2.33}$$

If all non linear phenomenons take place in a very small zone, then the stresses near the crack tip can be approximated by the first term of Equation 2.32. This zone is called the zone of "dominance of K". The stress field is singular at the crack tip and can be described by only one simple term, proportional to K [27].

2.1.9.2.2 Energy restitution rate G

Another approach to study a cracked material submitted to a load is to look how the energy is redistributed during crack propagation. By considering a plate with a crack in its thickness undergoing a force F, the displacement u of the point of application of the force increases linearly with the load. The ratio $\frac{F}{u}$ gives the stiffness of the plate while $\frac{u}{F}$ gives the compliance. Crack extension causes a decrease of the stiffness of the structure containing the crack. In order for the crack to propagate, the work done $F\Delta u$ must be higher than the change of elastic strain energy ΔW_e. Indeed a part of the available energy is used to propagate the crack. The energy release rate G is defined as the amount of elastic energy that is available (which can be released) to propagate the crack [27]. The units of G are the one of an energy per unit area of crack J/m^2 and it is defined by:

$$F\Delta u - G\Delta A = \Delta W_e \tag{2.34}$$

The change of potential energy is:

$$\Delta P = \Delta W_e - F\Delta u \tag{2.35}$$

When ΔA tend to 0, G represents the mechanical energy variation due to an infinitesimal increase of crack area:

$$G = -\frac{\partial P}{\partial A} \tag{2.36}$$

The energy release rate G can also be viewed as a change of free energy or free enthalpy. It is the driving force for crack propagation in the material [27].

2.1.9.2.3 Toughness K_{IC} and G_{IC}

The stress intensity factor K and the energy release rate G increase progressively with the force applied until they reach a critical value when the crack propagation begins. In plane strain and mode I, those critical values are noted K_{Ic} and G_{Ic} and they are intrinsic properties of the material both called toughness [27]. The toughness is the ability of a material to absorb mechanical energy without fracturing or deforming [68].
Cracking occurs only if:

$$K_I \geq K_{Ic} \text{ or } G_I \geq G_{Ic} \tag{2.37}$$

The crack propagation continues for brittle materials if $K_I = K_{Ic}$. The required value of K for propagation usually continues to increase after the beginning of the propagation until reaching a steady state and thus the propagation condition is

given by:

$$K \geq K_R(\Delta a) \tag{2.38}$$

Where K_R is a function of the crack propagation.

2.1.9.2.4 Measurement of toughness

The toughness can be calculated by measuring K_{Ic} or G_{Ic} according to a standard method named ASTM D5045-99 [28]. This standard assumes an elastic linear behavior and a plane strain situation, it implies the loading of a notched sample with a pre-crack. To perform this test a single edge notched bending specimen (SENB) is often used as shown in Figure 2.45. In Figure 2.45, B is the thickness of the specimen, W the width such as $W = 2B$ and S the distance between the points of application of the force such as $S = 4W$. The length of the crack a must be between $0.45W$ and $0.55W$.

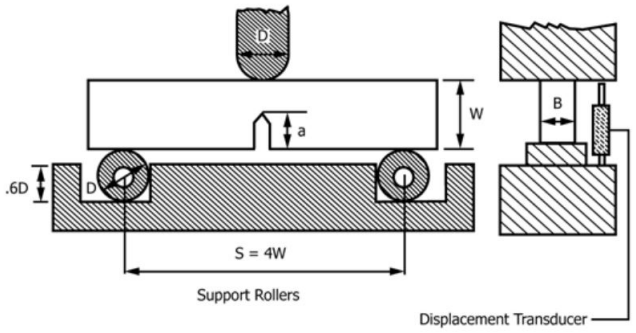

Figure 2.45: Geometry of a SENB specimen [28].

K_{Ic} and G_{Ic} values depend on the loading speed and the temperature. Those two parameters must thus be specified. To obtain a valid measurement the following condition must be respected:

$$B,\ a,\ (W-a) > 2.5\left(\frac{K_Q}{\sigma_y}\right)^2 \tag{2.39}$$

Where K_Q is the effective value of K_{Ic} and σ_y the yield strength. Indeed if B is too small then the plane strain behavior is not ensured and if $W - a$ is too small then the linear hypothesis is not respected. In order to ensure reproducibility of the test, at least three measurements for each material should be taken [28].

The force-displacement curve which is linear in the ideal case shows a sudden drop when the crack begins to propagate. An example of such curve is given at Figure 2.46. Thanks to this curve it is possible to determine K_Q the effective value of K_{Ic} [28].

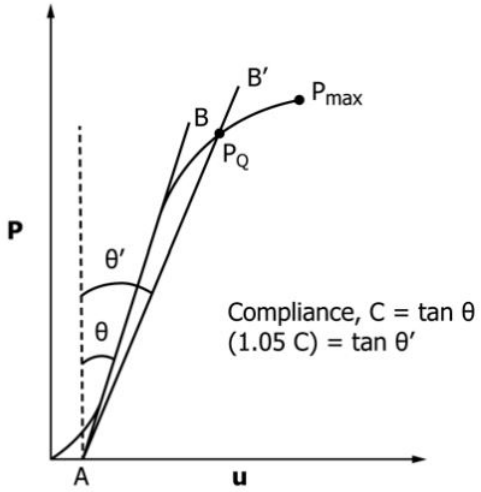

Figure 2.46: Force-displacement curve obtained with a three-points bending test on a SENB specimen [28].

To determine if the value of K_{Ic} is valid, a conditonal result must first be calculated K_Q, it must respect the conditon of Equation 2.39. To this end the initial compliance C must be calculated which is the inverse of the slope of the initial tangent (AB line). Then one must draw the line (AB') with a compliance of 5% higher than C. If the maximum force P_{max} supported by the specimen sits between the lines (AB) and (AB'), then P_{max} is used to calculate K_Q. Otherwise as illustrated in Figure 2.46 one needs to use the point P_Q which is the intersection of the curve with the line (AB'). Finally if $P_{max} > 1.1P_Q$ the measurement is not valid [28].

Once P_Q measrued, K_Q can be calculated using:

$$K_Q = \left(\frac{P_Q}{B\ W^{\frac{1}{2}}}\right) f(x) \tag{2.40}$$

Where the function f of $x = \frac{a}{W}$ such that $0 < x < 1$ is:

$$f(x) = 6\ x^{\frac{1}{2}} \frac{[1.99 - x\ (1-x)\ (2.15 - 3.93x + 2.7x^2)]}{(1+2x)\ (1-x)^{\frac{3}{2}}} \tag{2.41}$$

If all the required conditions of validity of the test are respected then:

$$K_{Ic} = K_Q \tag{2.42}$$

Another way to determine the toughness of the material is to calculate G_{Ic} which is given by Equation 2.43:

$$G_{Ic} = \frac{(1-\nu^2)\ K_{Ic}^2}{E} \tag{2.43}$$

Where ν is the Poisson coefficient and E must be obtained at the same time and temperature conditions as the fracture test because of viscoelastic effects. However this procedure introduces many uncertainties and it is considered to be better to determine G_{Ic} from the energy derived from integration of the load-displacement curve up to P_Q as:

$$G_{Ic} = \frac{U}{W\ B\ \phi} \tag{2.44}$$

Where U is the corrected energy and ϕ the calibration factor which can be found in tables as a function of the geometry. To find U the corrected displacement $u_c(P_Q)$ must be calculated from the measured displacement $u_Q(P_Q)$. To this end one need to determine the force-displacement curve of a specimen without pre-crack and to determine $u_i(P_Q)$ [28]. The value of the corrected displacement is finally given by:

$$u_c(P_Q) = u_Q(P_Q) - u_i(P_Q) \tag{2.45}$$

2.2 Literature review

2.2.1 Thermoplastic nanocomposites

To improve poor or insufficient properties of polymer, one can use composites which combine the advantages of their different constituent phases and surface properties. Nanocomposites are defined as multiphase materials where at least one of the constitutive phases has at least one dimension in the nanoscale range, that is to say below $100nm$. Nanofillers in polymer give access to multifunctional polymer composites with improved thermal, mechanical or electrical properties [53, 70]. With nanosized fillers significant improvement can be achieved with less than 10% of fillers unlike micron-sized fillers which are added in quantities above 30% to obtain significant improvement [70]. Nanoscale fillers are of various sizes ans shapes and can be classified according to their origin (synthetic or natural) or their synthetic pathway. Conventionally, nanofillers can be classified in three classes depending on dimensionality of the nanosized particles as followed [46, 53]:

1) *Plate-like nanofillers* are one-dimensional layered materials with a thickness on the order of $1nm$ with an aspect ratio of at least 25 for the two remaining dimensions. Layered silicates or graphene sheets are examples of such 1D nanofillers.

2) *Whiskers or nanofibres* are two-dimensional fillers with a diameter below $100nm$. They are characterized with an aspect ratio of at least 100. Carbon nanotubes are one of the main used nanofibres.

3) *Nanoparticles* are three-dimensional fillers exhibiting dimensions below $100nm$. Nanoparticles of silica have been investigated a lot as 3D nanofillers.

Nanoscale fillers have large surface area for a given volume due to their nanoscale dimensions. For particles and fibres, the surface area is inversely proportional to the diameter of the nanofiller [53].
Good dispersion of inorganic or organic fillers in the polymer matrix and good affinity between those two are significant parameters that determine the overall improvement [70].

2.2.1.1 PLA-based nanocomposites

Due to low crystallisation ability and degree of crystallisation of PLA limiting its industrial application, strategy consisting to incorporate nanosized reinforcements in the polymer matrix has been developped over the past years. So to enhance thermo-mechanical properties of PLA (as brittleness) and to supply additional functionalities such as fire-resistance, different types of nanoscale inorganic or organic fillers have been investigated as reinforcements [46, 53].

2.2.1.1.1 Silica/PLA nanocomposites

Commonly nanosilica particles as hard fillers are added in polymers to enhance the strength, adhesion, durability and abrasion resistance. Yan at al. [71] studied the addition, in PLLA matrix, of surface-modified silica nanoparticles with a L-lactic acid oligomer by grafting onto the surface of the silica nanoparticles. This incorporation leads to a significant increase in toughness and tensile strength of the composite because of the uniform dispersion of the nanoparticles in the PLLA matrix. However the addition of ungrafted SiO_2 nanoparticles into PLLA matrix degraded the mechanical properties of the composites [71]. Another study found that PLA/silica nanoparticles composites demonstrated better thermal stability than neat PLA [72].

2.2.1.1.2 Cellulose/PLA nanocomposites

Cellulose nanofillers can be defect-free rod-like nanoparticles called cellulose nanocrystals (CNs) or laterally yielding bundles of their elementary protofibrils called nanofibrillated cellulose (NFCs) or cellulose can be biosynthesised through microorganisms known as bacterial cellulose (BC).
The study of Oksman et al. [73] investigated an extruded blend of PLA and cellulose fibres to make a composite. The cellulose fibres incorporation results in improved mechanical properties of the PLA. Other researchers developed CNF/PLA nanocomposites using twin screw extrusion and no surface modification treatment was used. The results showed an increase of modulus and tensile strength, compared to neat PLA, from 2.9 to $3.6GPa$ and from 58 to $71MPa$ respectively when $5wt\%$ CNF was incorporated in PLA [74]. Microfibrillated cellulose (MFC) - PLA nanocomposites were made by Nakagaito et al. in 2009 [75]. The researchers showed that the modulus, strength and strain at fracture of the obtained composite increased linearly with the MFC content as well as that the toughness was improved.

Many other nanofillers have been investigated such as carbon nanotubes (CNTs), layered ceramic, glass particles, titanium or zinc oxide and alumina or Fe_3O_4 particles.

2.2.1.2 Lignin-Modified Polyester Materials

Lignin is an attractive inexpensive biodegradable material as a filler or as a chemical component in polymer blends due to these characteristics and particularly because of its biodegradability. Moreover the thermoplasticity of lignin can be improved by selectively changing its phenolic hydroxyl groups by hydroxylpropyl or methyl groups. Hence the addition of lignin derivatives in poylester can produced modified materials with excellent mechanical properties [7, 15, 76]. Alkylated kraft lignin possesses a structure and a stretching behavior similar to polystyrene and has good compatibility with aliphatic polyesters. Moderate hydrogen bonds are formed between the hydroxyl groups on the lignin and the carbonyl groups on the polyester [76].

2.2.1.2.1 Lignin/PCL nanocomposites

Polycaprolactone (PCL) is a bio-degradable thermoplastic, produced by ring-opening polymerisation and lignin-modified PCL materials can be made by mechanical blending. By incorporating 40% of lignin, the Young's modulus increases from $223MPa$ for the pure PCL to $448MPa$ for the obtained material. Unfortunately, as the lignin content increases, the strength and elongation at break of the material decrease. This phenomenon is due to the presence of lignin particles that are not

being able to be deformed preventing the formation of the long-range continuous phase PCL drawn at room temperature. Therefore when mass fraction of lignin added is lower than 25%, the obtained material presents good mechanical properties. In addition when the lignin content is too high, the compatibilty between lignin and PCL is relatively weak. Solution casting can also be used to prepare lignin-modified PCL with mechanical properties similar to those of lignin-modified materials prepared by mechanical blending. Glass transition temperature, melting temperature and crystallinity of PCL-lignin blends are similar to the those of pure PCL. The presence of lignin accelerates the decomposition of PCL at high temperature [29, 76].

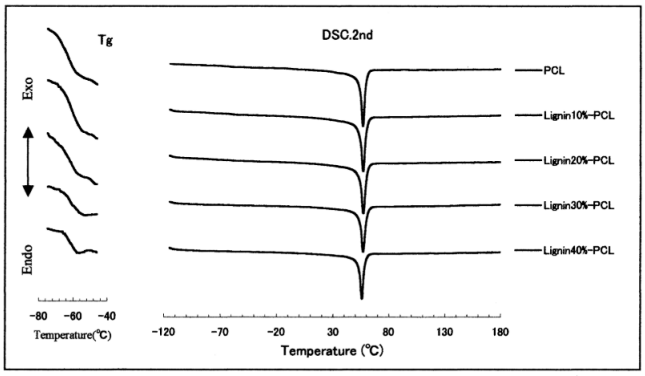

Figure 2.47: DSC second heating scans of PCL and its blends with various lignin content (prepared by mechanical mixing). Amplification of the area near T_g on left side [29].

2.2.1.2.2 Lignin/PHB and Lignin/PET nanocomposites

Addition of low content ($10\% - 40\%$) of lignin which acts as a good nucleating agent, in polyhydroxybutyl (PHB) can improve its crystallinity, accelerate the growth rate of spherulites and significantly reduce the crystallisation time. The crystal structure of the PHB matrix is not affected by the incorporation of lignin. However when the content of lignin is high ($70\% - 90\%$), the compatibility between the PHB matrix and lignin is poor and the crystallinity is not affected [76].
Lignin particles can also improve crystallinity and crystal size of polyethylene terephtalate (PET) matrix. As lignin content increases, the crystalline fraction of PET increases. The particles can be dispersed at a scale of several tens of nanometers to a few microns [76].

2.2.1.2.3 Lignin incorporation in PLA matix

Several studies were conducted on nanocomposites based on lignin and PLA. In 2014, a study using unmodified lignin and acetylation of lignin which chemically modified each lignin by esterification of its hydroxyl groups to improve the interaction with PLA was realised. The incorporation of lignin in both cases improved the thermal stability of the PLA. Indeed, the blends showed higher degradation onset and maximum temperature than pure PLA. However the crystallizaion behavior of PLA was not favoured with the addition of lignin in both cases. The incorporation of high percentages of lignin induced a degradation of mechanical properties such as failure strength and Young's modulus. Nonetheless, PLA/acetylated lignin blends showed similar mechanical properties to those of pure PLA. Moreover in all cases, an increase of the elongation at break was observed [46, 77]. When the lignin content exceeds 20%, the addition of lignin can accelerate the degradation rate of PLA at 200°C, and when the content of lignin is <20%, the modified PLA showed a good comprehensive performance, making it a promising modified material. The study of Spiridon et al. [78] on unmodified lignin/PLA composites indicated an increase in Young's modulus and Charpy impact strength. The addition of lignin obtained from softwood and hardwood enhanced the thermal stability of PLA and SEM micrographs revealed a good adhesion between the lignin and the PLA matrix [46, 78].

A study published in 2003 examined the thermal and mechanical properties of biodegradable blends of poly(L-lactic acid) (PLLA) and lignin prepared by manual mixing [7]. On the DSC scans performed shown in Figure 2.48, a single composition-dependent T_g between those of the pure components is observed which demonstrates miscibility. However the research precises that as the macromolecular structure of lignin is complex and that lignin does not show glass transition or melting phenomena, the blend can not be described by using the terms "miscibility" or "immiscibility". Pure PLLA which is a semi-crystalline polymer showed in DSC scan an exothermic peak at $63.4°C$ corresponding to the glass transition of amorphous domains and an endothermic peak at $169.9°C$ corresponding to the melting of crystalline domains. In addition to those two phenomena, exothermic peaks are observed just near the endothermic peaks which are due to cold crystallisation of the polymer during heating. As illustrated by Figure 2.48, when the contents of lignin in the blend increased from 0% to 40%, T_m decreased from $169.9°C$ to $161.8°C$. In the meantime T_g slightly decreased from $63.4°C$ to $57.3°C$ when the content of lignin increased to 40%. In other words T_m decreased by $0.2025°C$ per % of lignin added while T_g decreased by $0.1525°C$ per % of lignin added. These effects are due to the formation of hydrogens bonds between the carbonyl groups of PLLA and the phenolic hydroxyl groups of lignin. Those specific interactions responsible of the formation of miscible blend between PLLA and lignin were investigated by

FTIR spectroscopy [7].

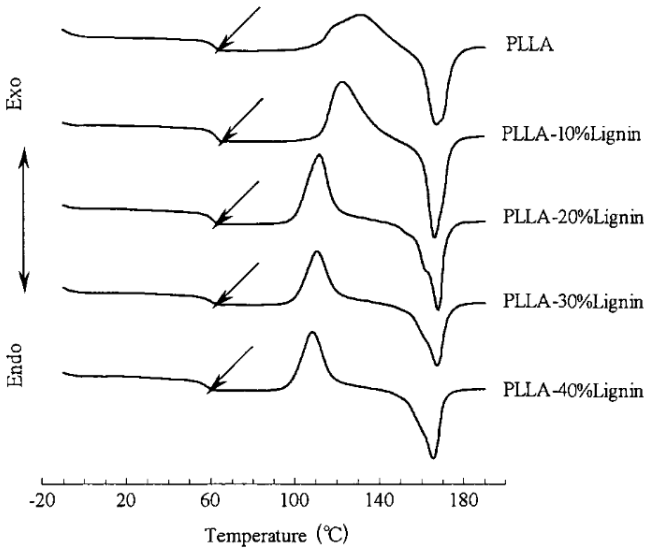

Figure 2.48: DSC second heating scans of PLLA and its blends with various lignin contents. The samples have been aged at $80°C$ for more than 2 weeks [7].

Tensile tests were performed to evaluate the mechanical properties of PLLA-lignin blends. The results in terms of maximum strength (σ_{max}), elongation at maximum strength (ε_{max}), elongation at break (ε_b) and Young's modulus (E) are listed in Table 2.7. When lignin is added, σ_{max} and ε_{max} decrease. However E value remains roughly the same up to 20% of lignin added. The study concluded that the mechanichal properties of the polymer stays at an acceptable level when the content of lignin is less than 20%. The presence of lignin particles of size about $3\mu m$ explained the observed reductions of mechanical properties. Indeed manual mixing could not make the two components blend at molecular level but only at the macroscopic level [7].

Thermogravimetric analysis (TGA) was performed to evaluate the thermal stability of the PLLA-lignin bends, the TGA curves are depicted in Figure 2.49. The curves of PLLA-0%lignin, PLLA-10%lignin and PLLA-20%lignin nearly superimpose from the starting point until degradation stage. Moreover when the temperature is higher than $365°C$, the difference between these three curves is almost entirely due to lignin residue. The results showed that when the content of lignin is no more than 20%, lignin has no obvious incidence on PLLA degradation and the starting point of thermal degradation T_s remains about $308°C$. Though when the

Table 2.7: Mechanical properties of PLLA and the blends with lignin [7].

Samples	$\sigma_{max}\,[Nmm^{-2}]$	$\varepsilon_{max}\,[\%]$	$E\,[Nmm^{-2}]$	$\varepsilon_b\,[\%]$
PLLA	68.1	4.92	1894	5.07
PLLA-10% lignin	46.8	3.19	1888	3.25
PLLA-20% lignin	38.4	2.38	1863	2.42
PLLA-30% lignin	28.5	2.30	1421	2.36
PLLA-40% lignin	23.2	2.18	1275	2.25

lignin content is higher than 20%, a clear decrease of T_s was observed. Lignin had thus a destabilizing effect on PLLA: T_s was only $289°C$ when the lignin content was 40% for instance. T_s is defined as the temperature at which the net weight loss of PLA is 5% either in the pure state or in blends when the effect of PLA on the degradation of lignin is neglected. The deterioration of mechanical properties could also be attributable to the fact that lignin accelerated thermal degradation of PLLA [7].

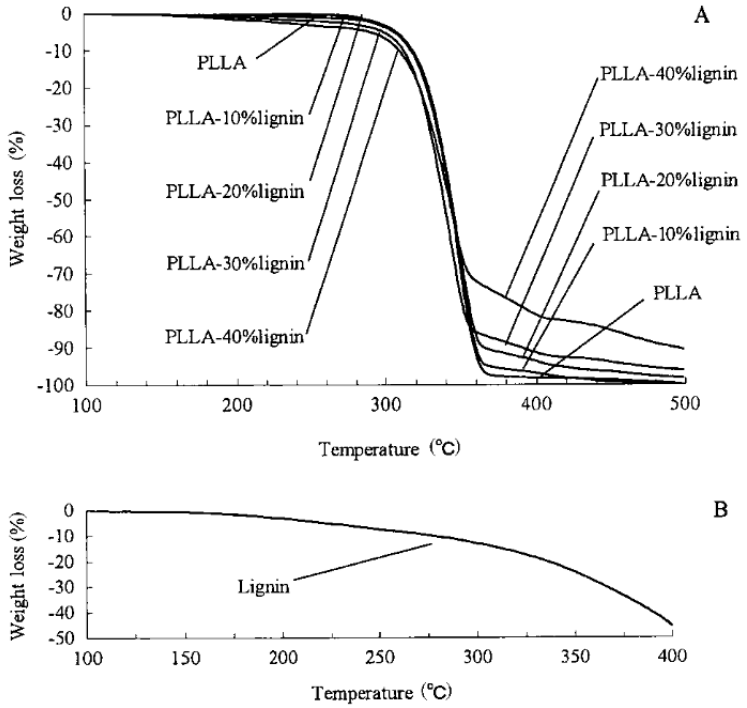

Figure 2.49: TGA curves of (A) PLLA and its blends with various lignin contents and of (B) lignin [7].

2.2.2 Improvement of epoxy resin with thermoplastic

Adding soft elastomer particles as toughening agent lead to a decrease in yield strength, creep resistance, thermal stability and stiffness due to the low glass transition temperature T_g. Therefore thermoplastic polymers have been used to toughen epoxy resin. Because of high stiffness (E) and high T_g, higher contents of thermoplastic can be incorporated in resins compared to elastomers [30].

2.2.2.1 Toughening mechanisms

Epoxy resins are intrinsically brittle materials with low fracture toughness at room temperature owing to the high cross-linking density. The usual strategy adopted to increase the fracture toughness of epoxy resins is to use a second phase which precipitates during curing. This addition will lead to a multiphase morphology able to initiate different toughening mechanisms during crack propagation. Different types of additives have been studied such as rubbers, inorganic glasses, acrylates, and ductile engineering thermoplastics [30, 60, 79]. In general, modifying epoxy

resins with rubber results in a decrease of T_g of the epoxy resins which is usually unfavorable for mechanical and thermal properties of the composites. Adversely, the addition of thermoplastics with a high T_g and modulus can lead to an increase in toughness without decreasing T_g or other properties [34].
For the toughening of multiphase system, four parameters are essential [79]:

- the adhesion between the particle and the matrix;
- the size of the separated particles;
- the distribution of the particles within the matrix;
- the strength of the separated particles.

Several toughening mechanisms of epoxy systems by rigid thermoplastic particles have been highlighted [30, 60]: particle bridging, crack pining, crack path deflection, particle-yielding-induced shear banding, particle yielding and microcracking. Those mechanisms are illustrated in Figure 2.50.

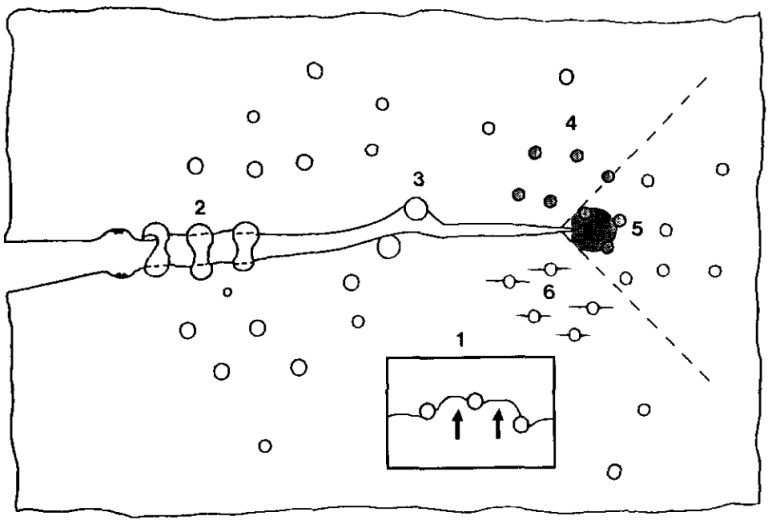

Figure 2.50: Shematic representation of toughening mechanisms for thermoplastic-modified epoxy resins: (1) crack pinning, (2) particle bridging, (3) crack path deflection, (4) particle yielding, (5) particle-yielding-induced shear banding and (6) microcracking [30].

Crack pinning The role of the thermoplastic particles (hard filler particles) is to act as impenetrable objects that prevent the propagation of the crack front and result in crack front bowing out between the particles. This phenomena causes an increase in toughness because it consumes extra energy. Thermoplastic particles can be considered as quasi impenetrable due to sufficiently large difference in toughness between the brittle epoxy resin and the ductile thermoplastic phase [30, 31, 60].

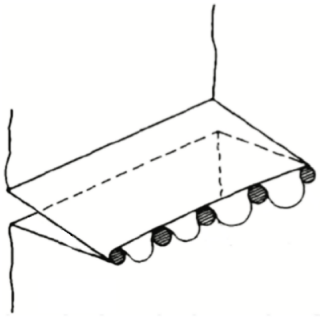

Figure 2.51: Scheme of crack pinning [31].

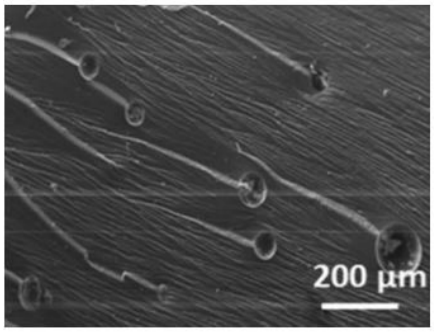

Figure 2.52: SEM picture of fracture surface of a thermoplastic modified resin with crack pinning [32].

Particle bridging - Crack bridging When rigid thermoplastic particles are used, particle-bridging mechanism could be more dominant. Rigid particles bridge two crack surfaces limiting the opening of the crack tip and apply surface tensile stress which reduces stress applied at the crack tip. Particles toughen epoxy resins through crack bridging mechanism involving large plastic deformation of the second phase, one needs to take into account the energy consumed when the crack deforms and tears the rigid particles [30, 31, 60].

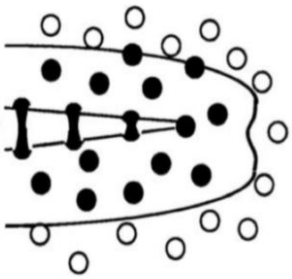

Figure 2.53: Scheme of crack bridging [33].

Figure 2.54: SEM picture of fracture surface of a thermoplastic modified resin with crack bridging [32].

Crack path deflection The thermoplastic particles induce the crack to deviate from its initial direction consequently, the crack surface area increases which results in an increase of the energy needed to propagate such crack [30, 60].
Deflection of cracks can be separated into [31]:

- *Tilting* characterised by an in-plane deflection and results in a mixed-mode (I&II) crack tip stress state.
- *Twisting* characterised by an out-of-plane deviation and results in a mixed-mode (I&III) crack tip stress state.

Figure 2.55: Scheme of crack path deflection [33].

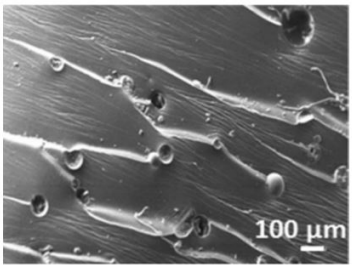

Figure 2.56: SEM picture of fracture surface of a thermoplastic modified resin with crack path deflection [32].

Particle-induced shear banding Thermoplastic particles can also induce shear banding in the matrix analogously to rubber particles. Indeed, yielding of the rigid particles lowers their modulus up to that of the rubber. The modulus mismatch between matrix and yielded particles induces a significant stress concentration which initiates shear banding in the surrounding matrix [30, 60].

2.2.2.2 Thermoplastic-modified epoxy

To achieve efficient toughening of epoxy resin with thermoplastic blend, researchers [31, 79] have highlighted five factors:

1) the thermoplastic backbone should have high thermal stability and be soluble in the uncured epoxy, but it must form multiphase morphology and thus phase separate during curing;

2) the final morphology is very important: optimum toughness is usually reached through development of a phase-inverted (which is the case when more content of thermoplastic is added to the blend) or a co-continuous morphology;

3) the literature is ambivalent on the importance of reactive and functionalised end groups in the toughening phase, but end groups of thermoplastic can help for the compatibility;

4) an increase of crosslinking density of epoxy resins results in an increase of the efficiency of the toughening;

5) High molecular weights of thermoplastic filler promote the toughening of the matrix; however increase of molecular weight results in increase in viscosity which will be a constraint in some composite process.

PES incorporation

Bucknall and Partidge in 1983 [80, 81] were the first to used a thermoplastic, a polyethersulphone, to toughen blends of TGAP and TGDDM using DDS or DICY hardeners. A (PES) multiphase morphology with PES particles of around $0.5\mu m$ in diameter was observed when TGAP was used with the DDS harderner whereas all the other blends were homogeneous. The toughness of the blends with PES was improved but not significantly [79].
MacKinnon et al. [82] also worked with PES to toughen a TGAP/DDS epoxy resin system. With increasing content of thermoplastic the toughness of the material increased drastically when at least PES 20% was added and a co-continuous morphology was observed [79].

More recently Brooker et al. [83] investigated mechanical properties of a mix of DGEBF and TGA cured with MCDEA and toughened with different concentrations of PES with reactive end groups. E' and T_g did not really change with the addition of thermoplastic and there was no progressive improvement in Young's modulus E with increasing TP content. However the tensile strength σ_y and elongation at break ε_b increased when PES addition. In addition, the researchers observed a steady increase of fracture toughness with increasing content of the thermoplastic toughener, by up to 63% at 35 wt% PES but this increase did not correspond to a change in morphology [60, 79].

PEI incorporation

Mechanical properties of TGDDM cured with DDS and blended with PEI were examined by Gilbert and Bucknall in 1989 [84]. When the content of polyetherimide (PEI) added was of 30% phase inversion occurred and a large increase in fracture toughness of 218% was observed. SEM images revealed that particle bridging was the major toughening mechanism and crack pinning a minor one [60, 79].
In 1992 Murakami et al. [85] worked on the mechanical properties of PEI-modified DGEBA. With 20% and 30% of PEI in the blend, the fracture toughness increased significantly of about 150% and 110% respectively while with only 10% no increase in K_{Ic} value was observed because no phase separation occurred. With 20% a particulate morphology with ductile thermoplastic particles dispersed within the epoxy matrix and particle bridging mechanism were noticed. Phase inversion happened when 30wt% of PEI was added. The PEI-modified blends showed higher T_g and stiffness than unmodified resin [60, 79].
More recently Kandpal et al. [86] studied EPN/PEI blends' mechanical properties. The results showed that the stiffness remained merely the same than without PEI and showed a moderate increase in tensile strength. However the Charpy impact strength considerably increased by up to 175% with 7.5% of PEI added. Actually PEI could reduce the entanglement of polymer chains and thus ensued in higher molecular mobility and improved toughness. At concentrations higher than 5% of PEI a heterogeneous morphology was observed, obtained due to CRIPS (explained in the next section). Indeed the phase separation occurred by spinodal decomposition [60].

2.2.2.3 Morphology of TS - TP with nanofillers

Before curing, thermoset/thermoplastic blends are usually homogeneous when the thermoplastic incorporated is amorphous such polystyrene (PS), polyetherimide (PEI), polysulfone (PSF) or polyehtersulfone (PES) as the TP phase is miscible with the epoxy resin. Nevertheless, the molar mass of the resin increases as the

crosslinking reaction progresses and phase separation is induced up to the gel point. This phenomenon is called cure-reaction-induced phase separation (CRIPS). It can happen by two mechanisms : either spinodal decomposition (SD) or nucleation and growth (NG) as shown in Figure 2.57 [34].

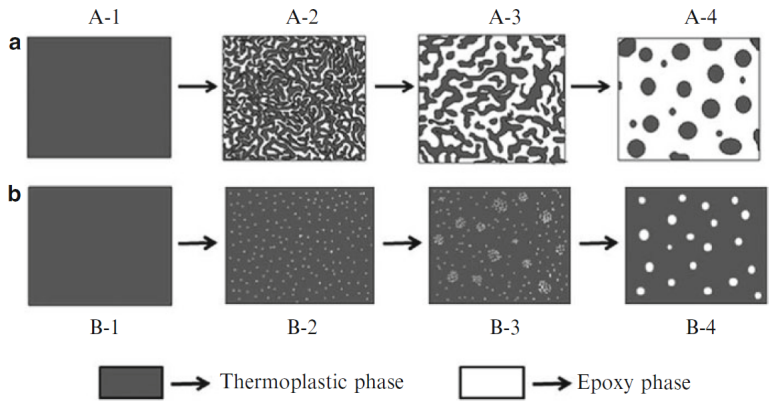

Figure 2.57: Illustration of (a) the spinodal decomposition (SD) and (b) the nucleus growth (NG) mechanisms in an epoxy/thermoplastic binary system [34].

Spinodal decomposition (SD) Initially, the mixture is a single phase and the thermoplastic begins to separate out during curing resulting in a co-continuous morphology as depicted in A-1 in Figure 2.57. Thereafter the thermoset regions grow and connect with each other which is called coarsening; this results in the destruction of the continuous phase of thermoplastic. The TP particles form islands with regular or irregular shape in the TS continuous phase (as A-4). If the thermoplastic content is high ($\geq$ 30 wt%), an inverted structure with TS particles distributed in a TP matrix can be obtained [34].

Nucleation and Growth (NG) Small TP particles within the thermoset are formed, they aggregate into larger particles which results in an island structure with regularly distributed TP particles as depicted in A-4 in Figure 2.57 [34].

The type of cure-reaction-induced phase separation mechanism depends on different parameters such as the curing temperature, the concentration of thermoplastic and the concentration of curing agent [34].
Some TS/TP systems are immiscible before the curing reaction, they do not undergo CRIPS mechanisms and the system remains phase separated after curing. This is

the case when the thermoplastic added is semi-crystalline such as polypropylene (PP) or polyethylene (PE) [34].

2.2.2.3.1 Nanoparticle distribution in TS/TP nanocomposites

The efficient dispersion of nanofillers in the matrix is one of the crucial factor in order to optimise the properties of the nanocomposites especially for mechanical properties. However, almost all nanoparticles are aggregated or agglomerated due to strong attractive interactions such as van der Waals forces which hinder interfacial adhesion and/or homogeneous dispersion in the polymer [34].

In the case of immiscible polymers blend multiphase composites, the dispersion of nanofillers throughout the material is usually not homogeneous. Three situation are possible as illustrated in Figure 2.58 whereby the nanofiller is located in one of the polymer phase or at the interface between them. The factors influencing the nanofiller distribution include thermodynamic and kinetic factors, dimensions and surface properties of the nanofillers and the viscosity of the polymer matrix [34].

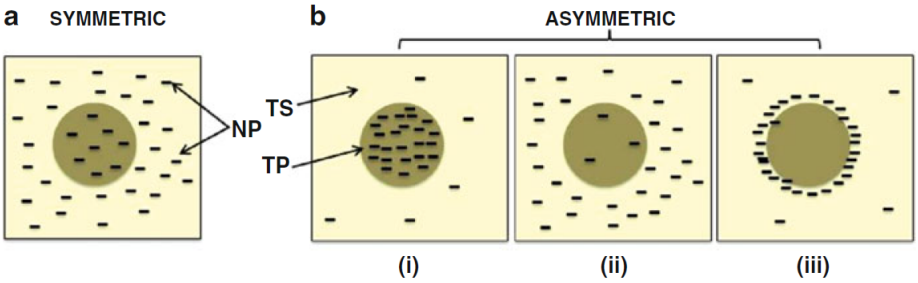

Figure 2.58: Illustration of possible nanoparticle distribution situation in TS/TP blend nanocomposites: nanofillers located (i) and (ii) in one of the polymer phase, (iii) at the interface between them [34].

The thermodynamics indicates that the location of the nanofiller depends on the balance of the interfacial energies which can be estimated using the wetting coefficient ω_a defined by the Equation 2.46:

$$\omega_a = \frac{\gamma_{filler-polymer1} - \gamma_{filler-polymer2}}{\gamma_{polymer1-polymer2}} \tag{2.46}$$

Where γ_{x-y} is the interfacial tension between the components x and y.
The wetting coefficient can be used to indicate the preferential location of the nanofiller. When $\omega_a < -1$ nanofillers tend to be located in polymer 1 while

when $\omega_a > 1$ they tend to be located in polymer 2 and when $-1 < \omega_a < 1$ it is more probable to be located at the interface. The nature of the polymer plays also a significant role on the nanoparticles dispersion. The location in one or the other polymer phase can be determined by the relative degree of interaction when intermolecular interactions occur between the polymer and the nanofillers [34].

In 2013, the study of Tao et al. [35] investigated addition of carbon nanotubes (CNTs) in a polyamide 12 (PA12) and acrylate-ethylene (EA) copolymer. The Figure 2.59 shows that a significant fraction of carbon nanotubes accumulated at the PA12/EA interface (partial interfacial confinement of the CNTs). In addition, the size of the PA12 domains was reduced due to the presence of CNTs compared to PA12/EA blends without CNTs. In Figure 2.59, PA12 dispersed phase appears darker.

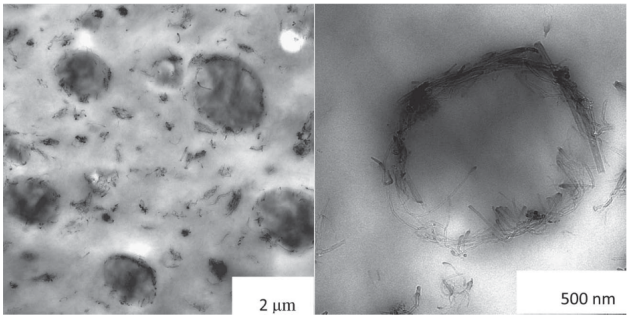

Figure 2.59: TEM images of PA12/EA blend with $1.8wt\%$ carbon nanotubes, obtained by premixing CNTs with EA next blending with PA12 [35].

During her Master thesis in 2017, Sarah Gabriel [36] has studied triphasic system : epoxy resin (TGDDM)/polyhydroxyether of bisphenol-A (PKHH) blends with addition of core shell rubber (CSRs). The TEM analysis revealed that the CSRs dispersion depends on the PKHH content in the system. When the content of PKHH reached 10%, CSRs agglomerated because the increase in PKHH concentration led to the formation of CSRs agglomerates due to their weak affinity as depicted in Figure 2.61. For a small amount of PKHH, CSRs formed circles around the PKHH nodules without adhering to their surface as shown in Figure 2.60. Indeed PKHH nodules are formed by nucleation and growth during curing. During growth the PKHH nodules pushed away the CSR particles dispersed in this area [36].

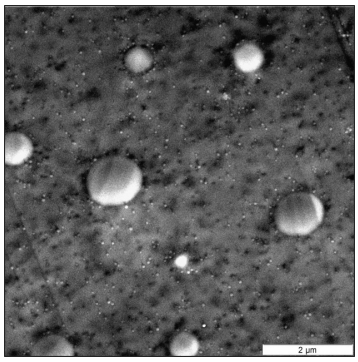

Figure 2.60: TEM picture of epoxy resin/PKHH (5%) with CSRs [36].

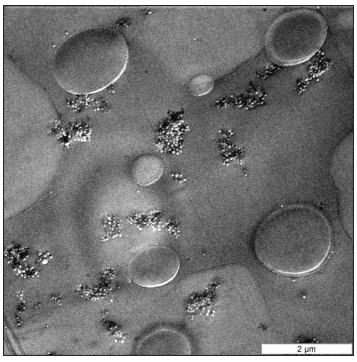

Figure 2.61: TEM picture of epoxy resin/PKHH (10%) with CSRs [36].

According to recent studies, many morphologies can be obtained by incorporating carbon nanofillers in TS/TP blends such as dispersed, co-continuous, dendritic, or phase-inverted ones. They showed that uneven or asymetric distribution of nanofillers could conduct to improvements in several properties because of synergistic effects. Especially, composites with a TP-spheres dispersed morphology and selective distribution of nanofillers at the TP/TS interphase could present an optimal equilibrium between toughness, stiffness and strength [60].

Chapter 3

Experimental part

At this stage, it is necessary to explain the steps followed during this work. As a first step extrusion and injection moulding of PLA - Lignin blends have been realised in different proportions (wt% of lignin). Their thermal properties, tensile properties and quality of dispersion were studied and characterised as well as the influence of composition and processing conditions on them.
In the second phase Lignin - bio-sourced epoxy resin, PLA - bio-sourced epoxy resin blends and blends of bio-sourced epoxy resin with PLA - Lignin nanocomposites were made. Their morphology, fracture toughness and hardness should further be analysed.

The scope of the chapter is to present the materials used during this work namely the PLA's, the lignin, the flax fibres, the bio-sourced epoxy resin and the hardener. The samples preparation and processing techniques as well as the characterisation techniques used for this work are also explained.

3.1 Materials

3.1.1 Thermoplastics: PLA

The thermoplastics used for this work are both supplied by *NatureWorks LLC*. One of the thermoplastic is a semicrystalline polylactic-acid (PLA) with *Ingeo^{TM} Biopolymer 2500HP* as reference which is designed to crystallise during processing. The other one is an amorphous PLA with *Ingeo^{TM} Biopolymer 4060D* as reference. Drying before processing is required for both. Other characteristics given by technical datasheets [8, 9] of the PLA's are reported in Table 3.1 and Table 3.2.

Table 3.1: Properties of *Ingeo^{TM} Biopolymer 2500HP* (PLA) [8].

Properties	PLA 2500HP
Aspect	opaque pellets
Density [/]	1.24
Melting temperature T_m [$°C$]	210

Table 3.2: Properties of *Ingeo^{TM} Biopolymer 4060D* (PLA) [9].

Properties	PLA 4060D
Aspect	clear (transparent) pellets
Density [/]	1.24
Glass transition temperature T_g [$°C$]	55-60

3.1.2 Charges

3.1.2.1 Lignin

Lignin powder used is a commercial soda pulp lignin from agricultural residues named *Protobind^{TM} 1000*. The extraction process is a $NaOH$ based one. Characteristics of this lignin are reported in Table 3.3. Before extrusion of Lignin / TP blends, lignin was manually mixed with the thermoplastic pellets. The elastic modulus of lignin is about $6 - 7\,[GPa]$.

Table 3.3: Properties of *Protobind^{TM} 1000* lignin.

M_n	$65000\,[g/mol]$
T_g	$102\,[°C]$
Particles size	between 20 & $200\,[\mu m]$

3.1.2.2 Flax fibres

Flax fibres were supplied by *Centexbel* and they didn't undergo chemical treatment. Long flax fibres were first cut into small fibres and manually mixed with the thermoplastic pellets before extrusion.

3.1.3 Thermoset system

The epoxy system used is a two-component epoxy system and is formulated for infusion or resin transfer moulding processes. The system is characterised by a very low viscosity at ambient temperature. The cured system shows a temperature resistance up to $100°C$ (T_g onset) [10].

3.1.3.1 InfuGreen 810 resin

The resin used is produced by *Sicomin*. The *SR InfuGreen* epoxy resin is made with about 38% of carbon derived from plant and therefore present a lower environmental impact than standard epoxy resins. Such a resin is said to be bio-sourced. The percentage of carbon from plant origin is function of the carbon origin contained in the epoxy molecule. The characteristics of the resin given in the technical datasheet [10] are reported in the Table 3.4. The resin is a colourless liquid with two epoxy components derived from rape and is composed of diglycidyl ether of bisphenol A, formaldehyde and 1,4-butanediol diglycidyl ether [87].

Table 3.4: Properties of *SR InfuGreen 810* resin [10].

Properties	SR InfuGreen 810
Aspect	clear liquid
Density at $20°C$	1.16 [/]
Viscosity at $25°C$	750 $[Pa \cdot s]$

3.1.3.2 SD 4771 hardener

The hardener used is the *SD 4771 UltraSlow* one supplied by *Sicomin*. This hardener is designed for very thick laminates by infusion and is composed of ether diamine, 4-methylcyclohexane-1,3-diamine and 2-methylcyclohexane-1,3-diamine. However, the hardener is not considered as bio-sourced (0% carbon green content). Therefore, the total percentage of bio-sourced components in the epoxy system is smaller than the one of the resin alone. The characteristics of the hardener given in the technical datasheet [10] are reported in the Table 3.5.

Table 3.5: Properties of *SD 4771* hardener [10].

Properties	SD 4771
Aspect	light yellow liquid
Density at $20°C$	0.944 [/]
Viscosity at $25°C$	9 $[Pa \cdot s]$

3.2 Samples preparation and processing

3.2.1 Drying

PLA must be dried sufficiently before processing in order to prevent excessive hydrolysis that can compromise the polymer's properties. Drying of PLA2500HP semi-crystalline takes place in the temperature range of $80-100°C$ and the required time depends on this drying temperature. Drying of PLA4060D amorphous takes place just below its glass transition temperature ($55-60°C$). *NatureWorks LLC*, the supplier of PLA polymers used in this project recommended that resins should be dried to 250 ppm moisture content, or below, before extrusion [3].
Drying of PLA was achieved in a vacuum pump chamber (see Figure 3.1) for more than 6 hour, usually all night.

Figure 3.1: Vacuum pump chamber used for drying.

3.2.2 Extrusion of thermoplastics

Premixes of PLA pellets and lignin powder are manually realised before extrusion. Extrusion is a thermo-mechanical manufacturing process in which 2 or more components are mixed to obtain an homogeneous mix. The material is then forced

to go through a die having the section of the desired shape. A rod of material is continuously formed. Figure 3.2 shows a schematic representation of a single screw extruder 's main components. A typical screw is composed of three sections [3, 88]:

- *Feed section* which receives the polymer and forward the polymer to the screw;
- *compression or melting section* which compresses the polymer's pellets to increase the contact with the barrel and the friction.
- *metering section* which acts as a pump to convey the required quantity of molten polymer into the die; this zone is characterized by a constant and shallow flight depth; in this section the flight depth decreases gradually.

The ratio of flight length of the screw and the flight outer diameter $\frac{l}{d}$ determines the residence time and the shear in the extruder. A screw with a large $\frac{l}{d}$ ratio presents better mixing, greater shear heating and longer melt residence time. The compression ratio given by the flight depth in the feed section divided by the flight depth in the metering section is a significant factor. The screw provides more shear heating if the compression ratio is greater [3].

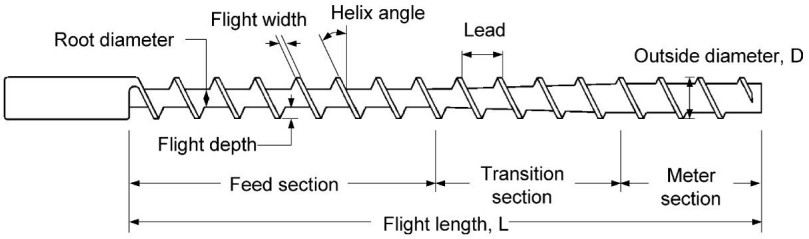

Figure 3.2: Typical geometries of a screw for single-screw extruder [3].

Extrusion was achieved with the *Thermo Scientific Process 11 Twin-screw Extruder* supplied by *Thermo Fisher Scientific* (see Figure 3.3). The two counter-rotating screws, driven by an electric motor, rotate and transport the molten polymer towards the end of the barrel. As the screws rotate, the flights shear and push the polymer against the wall of the barrel which also delivers frictional heat for melting the polymer. The heat required for melting is provided by the heater bands wrapped around the barrel and frictional heat from friction between the polymer and the screws and the barrel. The combined thermal energy provides sufficient heat to raise the PLA polymer above its melting point ($170 - 180°C$) by the time it reached the end of the barrel. In the case of the semi-crystalline PLA (2500HP), the heater set point is usually set at $190 - 210°C$ in order to guarantee that all the

crystalline phases are melted and to obtain an optimal melt viscosity for processing [3]. The extruder heated zones are represented in Figure 3.3. The T_5 & T_6 zones are the compression zones in the case of this extruder. The applied temperature profiles for this work are shown in Table 3.6 and Table 3.7. They are based on the ones recommended by *NatureWorks* technical datasheet [8, 9] although they differ slightly.

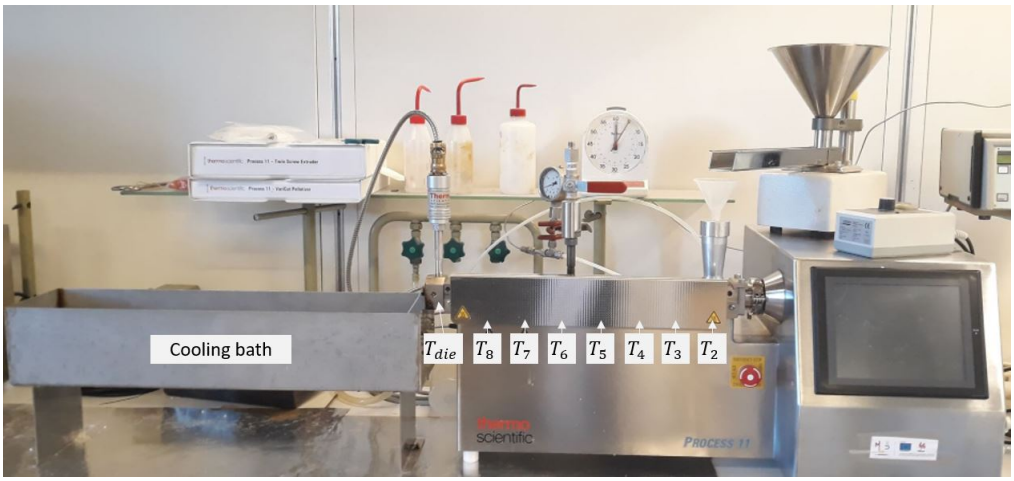

Figure 3.3: Picture of the *Thermo Scientific Process 11 Twin-screw Extruder* used.

Table 3.6: Extrusion parameters for PLA 2500HP pure and blends with lignin.

T_2	T_3 & T_4	T_5 & T_6	T_7 & T_8	T_{die}	Rotation speed	Torque τ
180 [$°C$]	190 [$°C$]	180 [$°C$]	200 [$°C$]	210 [$°C$]	100 [rpm]	35-50 [%]

Table 3.7: Extrusion parameters for PLA 4060D pure and blends with lignin.

T_2	T_3 & T_4	T_5 & T_6	T_7 & T_8	T_{die}	Rotation speed	Torque τ
190 [$°C$]	200 [$°C$]	190 [$°C$]	200 [$°C$]	200 [$°C$]	50 [rpm]	40 [%]

3.2.3 Injection moulding

Injection moulding is a manufacturing process for producing parts by high pressure injection of pelletised raw material into a mould which shapes the polymer into the desired form. Polymer is fed into a heated barrel (or cylinder) and then injected

into the mould cavity (see Figure 3.6), where it cools down and hardens while taking the shape of the cavity [3, 89].

Before performing injection moulding, the *VariCut Pelletizer* supplied by *Thermo Fisher Scientific* (see Figure 3.4) is used to cut the extruded rod into small pellets. Indeed small pellets melt faster and therefore the risk of polymer degradation when waiting for melting of it is reduced. Small pellets are then dropped in the heated cylinder of the injection moulding machine.

Figure 3.4: Picture of the *VariCut Pelletizer* used.

Figure 3.5: Picture of the *Thermo Scientific*^{TM} *HAAKE*^{TM} *MiniJet Pro* used.

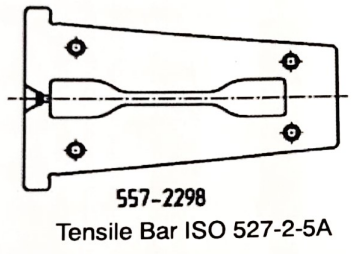

Figure 3.6: Schematic representation of the mould used.

Injection moulding of pure PLA's and PLA's / Lignin blends was achieved with the *Thermo Scientific*^{TM} *HAAKE*^{TM} *MiniJet Pro* supplied by *Thermo Fisher Scientific* (see Figure 3.5). The different settings of the piston injection moulding system used for injection moulding of PLA 2500HP / Lignin blends and PLA 4060D / Lignin blends are listed in Table 3.8 and Table 3.9 such as pressure p, post pressure p_{post}, temperatures of the cylinder $T_{cylinder}$ and the mould T_{mould}. A standardized ISO 527-2-5A mould for common plastic tensile testing is used. The pressure and the post pressure are maintained during 30 seconds.

Table 3.8: Injection Moulding parameters for PLA 2500HP pure and blends with lignin.

$n°$		$T_{cylinder}\,[°C]$	$T_{mould}\,[°C]$	$p\,[bar]$	$p_{post}\,[bar]$
1	PLA 2500HP neat	230	85	600	500
2	PLA2500HP neat extruded	230	80	600	500
3	PLA2500HP + 1% Lignin	225	85	600	500
4	PLA2500HP + 5% Lignin	225	85	600	500
5	PLA2500HP + 10% Lignin	210	75	600	500
6	PLA2500HP + 20% Lignin	210	80	600	500
7	PLA2500HP + 30% Lignin	210	80	600	500

Table 3.9: Injection Moulding parameters for PLA 4060D pure and blends with lignin.

$n°$		$T_{cylinder}\,[°C]$	$T_{mould}\,[°C]$	$p\,[bar]$	$p_{post}\,[bar]$
8	PLA4060D neat	230	85	600	500
9	PLA4060D neat extruded	230	85	600	500
10	PLA4060D + 1% Lignin	220	85	600	500
11	PLA4060D + 5% Lignin	215	85	600	500
12	PLA4060D + 10% Lignin	215	85	600	500
13	PLA4060D + 20% Lignin	205	75	600	500
14	PLA4060D + 30% Lignin	210	80	600	500

3.2.4 Epoxy resin - thermoplastic blends preparation

For the study of the system of modified epoxy resin with thermoplastic, only the PLA4060D, the amorphous one is used. To prepare TP modified epoxy resin, the thermoplastic must first be solubilised in the resin. The right percentage of PLA4060D or PLA4060D / Lignin blend was incorporated in *InfuGreen 810* resin gradually while the mix is heated up to $110°C$ and magnetically agitated. To add the hardener, the mix needs to slowly cool down to $55°C$ to avoid that it already polymerises. Prior to pour the mix in the mould, degassing is need. Degassing is performed in a vacuum pump chamber. Once the mould is assembled, the mould is coated with *frekote*, a demoulding agent.
Different curing cycles were apply to neat resin and mix, there are all reported in Table 3.10. The curing cycle presented in Figure 3.7 consists of heating the system up to T_1 with a heating rate of $1.5°C/min$ and applying an isotherm at T_1 during $2h$ then heating the system up to T_2 and again applying an isotherm at T_2 during $2h$.

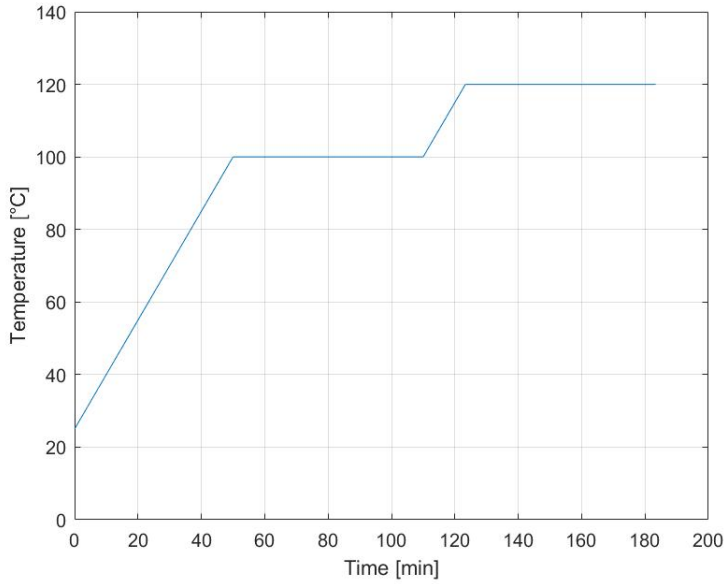

Figure 3.7: Curing cycle applied for resin/PLA blends.

Table 3.10: Curing cycle parameters for epoxy resin, epoxy resin/PLA and epoxy resin/Lignin blends.

n°		Curing cycle			
a	resin neat	70 $[^\circ C]$	2h	120 $[^\circ C]$	2h
b	resin + 0.5% Lignin	70 $[^\circ C]$	2h	120 $[^\circ C]$	2h
c	resin + 2% Lignin	70 $[^\circ C]$	2h	120 $[^\circ C]$	2h
d	resin + 3% Lignin	70 $[^\circ C]$	2h	120 $[^\circ C]$	2h
e	resin + 5% Lignin	70 $[^\circ C]$	2h	120 $[^\circ C]$	2h
f	resin + 10% Lignin	70 $[^\circ C]$	2h	120 $[^\circ C]$	2h
g	resin neat	80 $[^\circ C]$	2h	130 $[^\circ C]$	2h
h	resin neat	90 $[^\circ C]$	2h	140 $[^\circ C]$	2h
i	resin neat	100 $[^\circ C]$	2h	150 $[^\circ C]$	2h
j	resin + 1% PLA 4060D	100 $[^\circ C]$	2h	150 $[^\circ C]$	2h
k	resin + 2.5% PLA 4060D	100 $[^\circ C]$	2h	150 $[^\circ C]$	2h
l	resin + 5% PLA 4060D	100 $[^\circ C]$	2h	150 $[^\circ C]$	2h
m	resin + 10% PLA 4060D	100 $[^\circ C]$	2h	150 $[^\circ C]$	2h
n	resin + 15% PLA 4060D	100 $[^\circ C]$	2h	150 $[^\circ C]$	2h
o	resin + 20% PLA 4060D	100 $[^\circ C]$	2h	150 $[^\circ C]$	2h
p	resin + 10% (PLA 4060D + 10% Lignin)	100 $[^\circ C]$	2h	160 $[^\circ C]$	2h
q	resin + 10% (PLA 4060D + 5% Lignin)	100 $[^\circ C]$	2h	160 $[^\circ C]$	2h
r	resin neat	110 $[^\circ C]$	2h	160 $[^\circ C]$	2h

3.3 Characterisation techniques

3.3.1 Differential Scanning Calorimetry (DSC)

The Differential Scanning Calorimetry (DSC) (see Figure 3.8) is an analysis technique based on the measurement of the amount of heat required to increase or decrease continuously the temperature of a sample which is compared to a reference sample without any transition. The reference sample undergoes the same temperature profile. The difference of temperature between few mg of sample placed in a small Al pan and the reference (same empty Al pan) is measured during heating or cooling. The difference of temperature is considered as proportional to the heat flux. Two configurations exist: in the first one, the two pans are placed in the same

furnace and are heated or cooled at a constant rate. Calibration with standards allows to convert differences of temperature between sample and reference into specific heat. Two thermocouples measure the temperature of the furnace and the difference of temperature. In the second configuration, the two pans are placed in separated furnaces and maintained at the same temperature. In function of the heating power needed during the transformation of the sample, the heat flux can be determined. The heat absorbed or released is equal to the difference of electrical power supplied to heat the sample and reference furnaces. This method allows to determine the thermal transitions (glass transition, melting, crystallisation) and the enthalpy of the system [41, 58, 90].

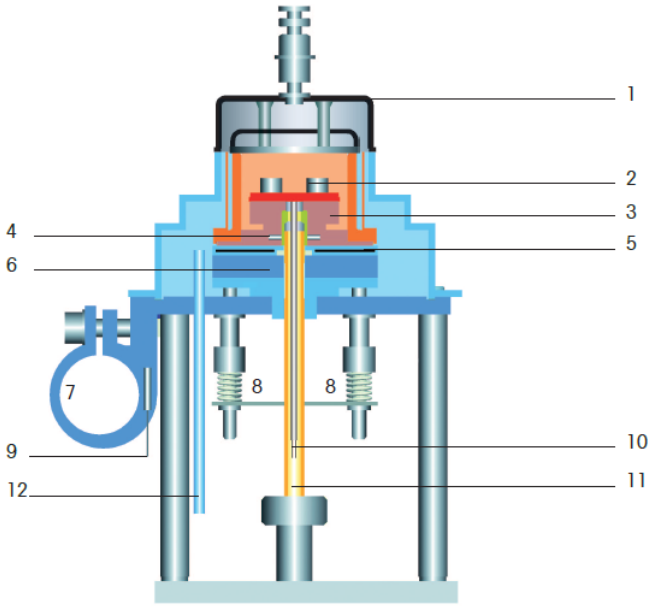

Figure 3.8: Schematic principle of a DSC. 1 - Furnace lid; 2 - Crucible on the DSC Sensor; 3 - Silver furnace; 4 - Pt100 temperature sensor of furnace; 5 - Flat heater between two insulating disks; 6 - Thermal resistance for cooler; 7 - Cooling flange; 8 - Compression spring construction; 9 - Cooling flange Pt100; 10 - DSC raw signal for amplifier; 11 - Purge gas inlet; 12 - Dry gas inlet [37].

The equipment used is a *DSC 1* supplied by *Mettler Toledo*. The data treatment is done using the *STARe* software. The crucibles used are $40\mu l$ standard crucible of aluminium with a perforated cover plate and without pin. After insertion of sample in the pan, the cover is sealed and drilled to allow gas exhaust during heating. For the analysis, ideal samples are as thin, flat and large as possible in order to ensure a good thermal contact and to avoid a temperature gradient. Finally, each sample

has a mass between 5 (to ensure a sufficient response) and 15 mg (to avoid inertia effect). The atmosphere is inert (nitrogen $50ml/min$).

The samples named *1, 2, 3, 4, 5, 6, 7, 8, 9, 10, 11, 12, 13, 14* in the Table 3.8 and Table 3.9 are analysed. The analysis is repeated 2 times for each sample/blend. The aim is to observe the influence of the extrusion and the influence of charges on glass transition, melting point and crystallisation.
The thermal method imposed to samples is illustrated graphically in Figure 3.9. The first segment is an isothermal one at $25°C$ during one minute. Next, the temperature is increased up to $200°C$ at a constant rate of $10°C/min$. A second isothermal segment at $200°C$ is applied during one minute before a decrease of temperature of $10°C/min$ down to $25°C$. Finally a second heating of $10°C/min$ up to $200°C$ is applied after a third isothermal segment at $25°C$ during one minute. The furnace then cools down automatically to ambient temperature. The first heating is done in order to erase the history of the polymer, however it gives information on the crystallisation that can happen during cooling of the polymer rush just after extrusion. The glass transition temperature is calculated during the second heating.

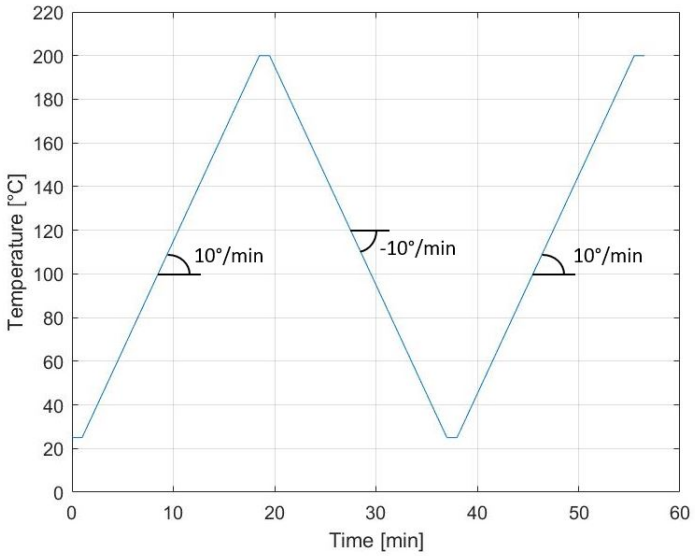

Figure 3.9: Method applied to each sample for the DSC analysis.

3.3.2 Thermogravimetric analysis (TGA)

Thermogravimetric analysis (TGA) (see Figure 3.10) measures the amount and the speed of weight change of a material, either as a function of increasing temperature, or isothermally as a function of time, in a controlled atmosphere. It allows to evaluate the material's thermal stability (material is stable if no weight change is observed) and its fraction of volatile components by monitoring the weight change which occurs as the sample is heated at a constant rate. This method also gives the upper use temperature of a material: beyond this temperature the material will begin to degrade. The device is constituted of a thermocouple which controls the temperature, a precision balance and a furnace. Different types of thermogravimetric analysis exist [59, 90]. The first one is an *isothermal* or *static* thermogravimetry in which the sample weight is recorded as function of time at constant temperature. Another one is called *dynamic* thermogravimetry in which the sample is heated in an environment whose temperature is changed in linear manner.

The thermogravimetric data collected are compiled into a plot of percentage of

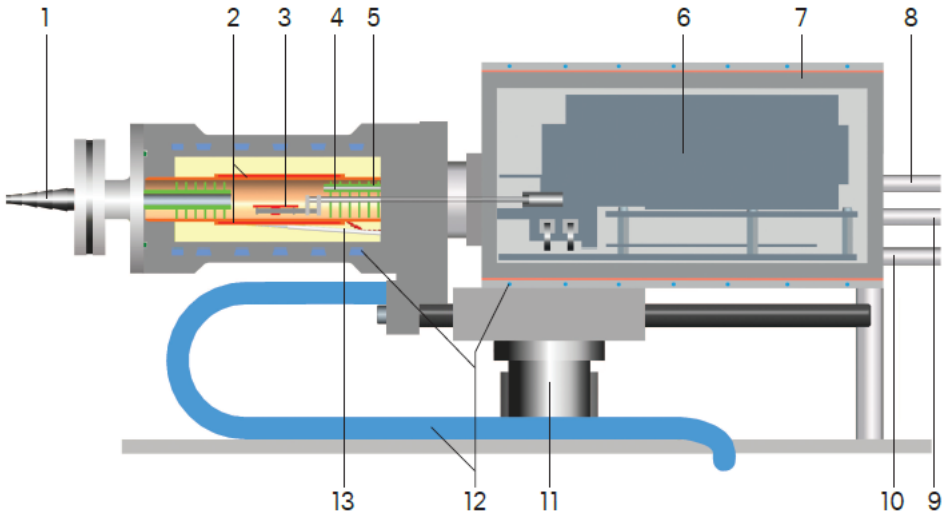

Figure 3.10: Schematic principle of TGA. 1 - Gas outlet; 2 - Furnace heater; 3 - Sample support; 4 - Reactive gas capillary; 5 - Baffles; 6 - Parallel-guided ultramicro balance; 7 - Thermostated balance chamber; 8 - Protective gas inlet; 9 - Reactive gas inlet; 10 - Purge gas inlet; 11 - Motor for opening sample chamber; 12 - Cooling circuit; 13 - Furnace temperature sensor [38].

initial mass on the y axis versus temperature. This plot is referred to as a TGA curve. The first derivative of the TGA curve may be plotted to determine inflec-

tion points useful for in-depth interpretations as well as differential thermal analysis.

The equipment used is a *TGA/SDTA851e* supplied by *Mettler Toledo*. The data treatment is done using the *STARe* software. The crucible used are $70\mu l$ standard reusable crucible of alumina. The chosen atmosphere for all the measurements done in this study is nitrogen ($50ml/min$). Finally, each sample has a mass between 5 (to ensure a sufficient response) and $15mg$ (to avoid inertia effect).

The samples numbers *1, 2, 3, 4, 5, 6, 7, 8, 9, 10, 11, 12, 13, 14* in the Table 3.8 and Table 3.9 are analysed. The analysis is repeated 2 times for each type of sample/blend. The aim is to observe the thermal stability of the polymers and the charges and the impact those charges.

The thermal method imposed to samples is illustrated graphically in Figure 3.11. The first segment is an isothermal one at $30°C$ during one minute. Next, the temperature is increased up to $600°C$ at a constant rate of $10°C/min$. The furnace then cools down automatically to ambient temperature. In order to avoid artefact due to expansion of air, a blank measurement is made which consists of the application of the thermal method to an empty crucible.

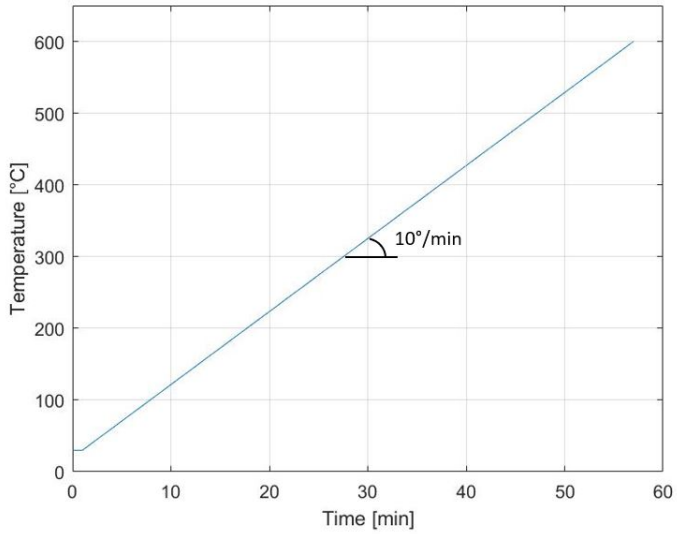

Figure 3.11: Method applied to each sample for the TGA analysis.

3.3.3 Scanning Electron Microscopy (SEM)

Scanning Electron Microscopy (SEM) consists of the bombardment of material surface by an electron beam derived from the thermoelectronic emission of a tungsten filament or an emision electron gun. The electrons have a smaller wavelength than photons, thus the resolution of such microscope is better than the one of an optic microscope. The electrons penetrate the sample and weakly bonded electrons forming the conduction band, called secondary electrons, are ejected. Backscattered electrons are also generated. Specific detectors are used. The secondary electrons have a weak energy therefore only electrons from the surface can escape the sample as shown in Figure 3.12. Those electrons are accelerated and the signal detected is amplified. The secondary electrons from the surface of the scanned sample are highly sensitive to surface variations which allows to obtain informations on the topology of the sample.

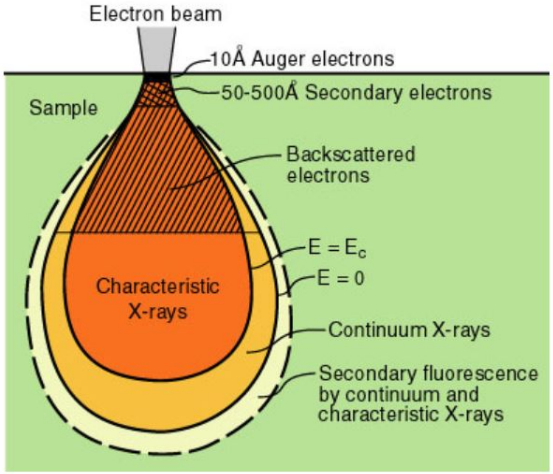

Figure 3.12: Generalised illustration of interaction volumes for various electron-specimen interactions [39].

The equipment used is a *Scanning Electron Microscopy 7600F* supplied by *JEOL*. The samples numbers *4, 11* in the Table 3.8 and Table 3.9 are analysed. The samples should be conductive in order to avoid charge phenomenon due to the accumulation of electrons which would lead to over-brightness and deflection of the beam. Therefore the surface of samples should be recovered by a conductive layer, however this was not done for lack of time. Moreover a vacuum pump system is used to avoid broadening of the beam and too important noise.

3.3.4 Tensile Test

During tensile test, a specimen is broken due to uniaxial tensile loading while clamped at its two ends. Tensile force is measured and recorded as a function of crosshead displacement when the tensile test is carried out. Several properties can be directly measured via a tensile test as ultimate tensile strength σ_u, breaking strength σ_b and elongation at break ϵ_b. Those measurements allow to obtain other mechanical properties of a material such as Young's modulus E, yield strength σ_y, Poisson's ratio ν and strain-hardening characteristics [66, 91].
Concerning this work, measurements of mechanical properties of specimens are performed at $23.3°C$ with a level of relative humidity of 50% on a *Zwick Roell* test machine at a crosshead speed of $5mm/min$. Specimens obtained by injection molding are tensile bar ISO 527-2-5A (see Figure 3.13). All specimens had a gauge length of $20mm$, and a gauge width of $4mm$ with variable thickness of $0.2 \sim 0.3mm$. The samples numbers *2, 3, 4, 5, 6, 7, 9, 10, 11, 12, 13* in the Table 3.8 and Table 3.9 are analysed. For each type of sample at least 3 reproducible tests were performed except for the semi-crystalline PLA 2500HP with 10% of flax for which only 2 tests were performed.

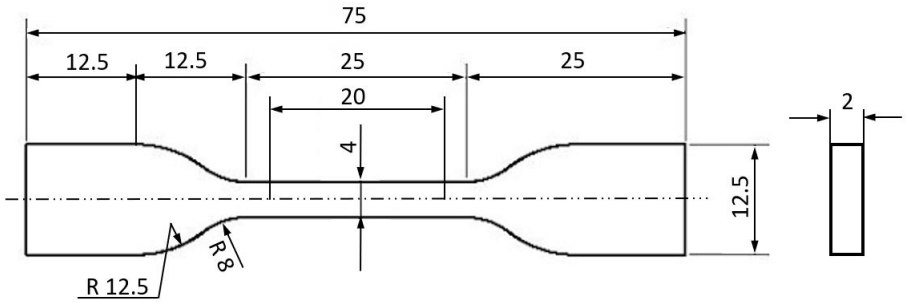

Figure 3.13: Tensile bar ISO527-2-5A (measurements in mm).

3.3.5 Dynamic Mechanical analysis (DMA)

Dynamic mechanical analysis (DMA) allows to test samples in a large range of configurations (torsion, three-points bending, elongation, compression,...) while controlling temperature and imposing a periodically varying stress or deformation (possibly superimposed to a static deformation) of small amplitude and controllable frequency to the sample. Measurements as a function of frequency (from few hundredths to a few hundreds of Hz) and temperature are ideal to characterise viscoelastic polymers. Depending on frequency, the material may behave as a solid or a liquid. This method is suitable to obtain the elastic or storage modulus $E^{'}$ which measures the elasticity of the material and its capacity to store energy. The viscous or loss modulus $E^{''}$ which depicts the capacity of the material to dissipate the energy, is also measured. The ratio of the loss modulus and the storage modulus gives the damping factor $tan\delta = \frac{E^{''}}{E^{'}}$. The glass transition temperature can also be determined because it corresponds to a sudden drop of the storage modulus $E^{'}$ and the maximum point of the loss modulus $E^{''}$ curve. The glass temperature transition can also be determined as the maximum of $tan\delta$. The strain resulting from the periodic stress will be periodic but out of phase due to energy dispersion as heat or damping if the sample is a viscoelastic material [41, 90].
When an elastic sample is vibrated over a range of frequencies, by measuring the amplitude of vibration, one can relate the resonance frequency ν_r to the Young's modulus E. The resonance frequency ν_r is the frequency for which a maximum in the plot of the amplitude of vibration against frequency is observed. The relationship between E and ν_r is given by the Equation 3.1 where c is a constant, L the sample length between clamps, d the sample thickness and ρ the sample density [41, 90].

$$E = \frac{cL^4\rho\nu_r^2}{d^2} \tag{3.1}$$

The device used for the experiment is a *DMA/SDTA861e* supplied by *Mettler Toledo* which is coupled with the *STARe* software (see Figure 3.14).

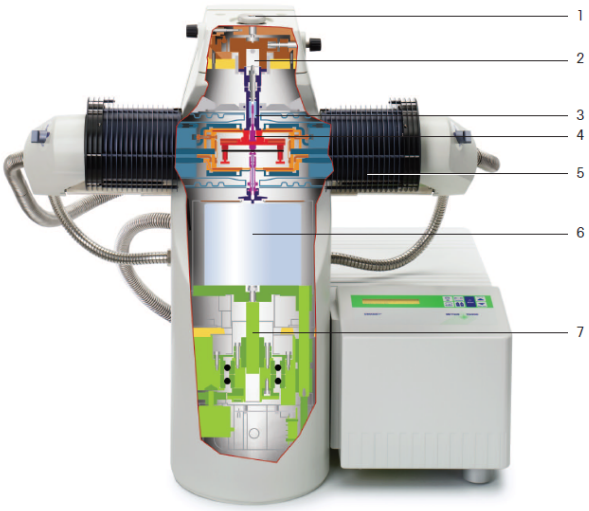

Figure 3.14: Scheme of Dynamic Mechanical Analysis (DMA). 1 - 4-axis alignment; 2 - Force sensor (piezoelectric); 3 - Displacement sensor (LVDT); 4 - Clamping assembly and sample holder; 5 - Furnace; 6 - Drive motor; 7 - Z-axis table [40].

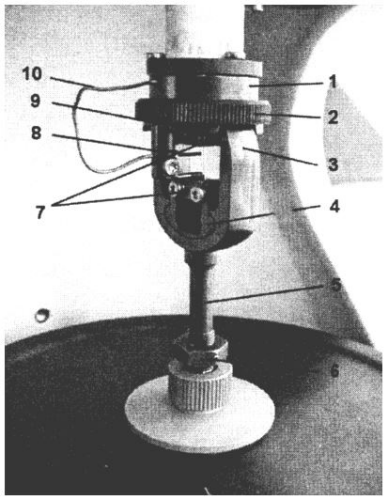

Figure 3.15: Zoom on the measuring head (elongation) of Dynamic mechanical analyzer (Mettler-Toledo) [41].

The method used is different for the semi-crystalline PLA (PLA2500HP) and the amorphous one (4060D), they are illustrated at Figure 3.16. The heating rate is of 3 $[°C/min]$ and the measurements are performed at a frequency of $1Hz$. A pre-test is realised for the two types of PLA in order to know the stress and strain limits to apply. The maximum force is of $2N$ and the maximum strain is of $1\mu m$ for the PLA4060D and $2\mu m$ for the PLA2500HP. The samples numbers *2, 3, 4, 5, 6, 7, 9, 10, 11, 12, 13* in the Table 3.8 and Table 3.9 are analysed. The analysis is repeated at least 2 times for each type of sample/blend. The aim is to observe the influence of the presence of lignin charges on glass transition temperature and storage modulus.

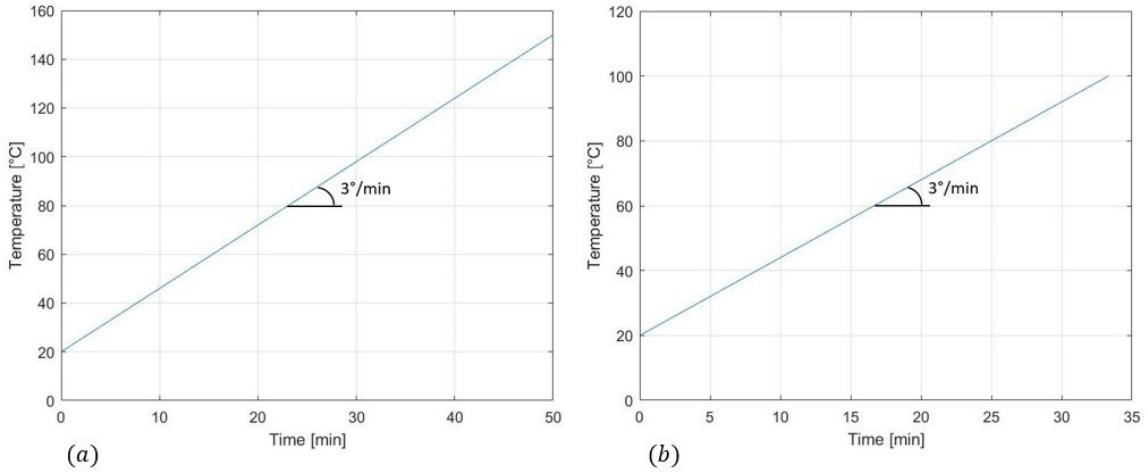

Figure 3.16: Method applied for the DMA analysis for each (a) PLA2500HP (+ Lignin) (b) for PLA4060D (+ Lignin).

3.3.6 Three-point flexural test

In order to characterise the toughness of TP/epoxy resin blends, SENB specimens are realised as depicted in Figure 2.45 with characteristic dimensions of $14mm$ for the width W, $7mm$ for the thickness B and the distance between points of support is $56mm$.

Chapter 4

Results and discussion

This chapter's aim is to present the results obtained from the experiments and analysis done during this work and to interpret them. A discussion will accompagny the description of the results based on the theory and the literature review outlined at the beginning of this work (Chapter 2). The discussion will relate the results with each other as well.

4.1 Characterisation of thermoplastic nanocomposites

4.1.1 Thermal characterisation (DSC and TGA analysis)

4.1.1.1 DSC Analysis

The data collected from the DSC analysis of blends with the semicrystalline PLA are summarised in Table 4.1 and in Table 4.4. Conventionally T_m corresponds to the temperature of melting of the crystalline domains and T_g corresponds to the temperature of the glass transition of the amorphous domains of the polymer.
The fluctuations of the baseline in the DSC scans are observed due to poor thermal contact between the crucible and the pellet. Indeed, the PLA pellets are very hard and small which makes them difficult to cut in order to obtain optimal mass and contact.
For the blends with the semi-crystalline PLA, 5 different peaks can be observed on the cooling and second heating scans as depicted in Figure 4.1:

- **Exothermic peak I:** the polymer crystallises during cooling at rate of $10°C/min$, the peak is very broad probably because different crystal types of

PLA are formed (with different crystallisation temperatures T_{cryst}).

- **Exothermic peak II:** further crystallisation of polymer during heating (called cold crystallization) becomes possible when the temperature is raised above T_{cryst} and thus reorganisation of polymer chains occurs.
- **Small endothermic peak III:** this peak is probably due to the fusion of the PLA crystals with a low thermal stability, formed at T_{cryst} or in the range of cold crystallisation.
- **Exothermic peak IV:** successive structural reorganisations into more stable crystals occur which result in the appearance of an exothermic peak at a temperature noted T^* in Table 4.1.
- **Endothermic peak V:** final melting of the perfected crystals of PLA.

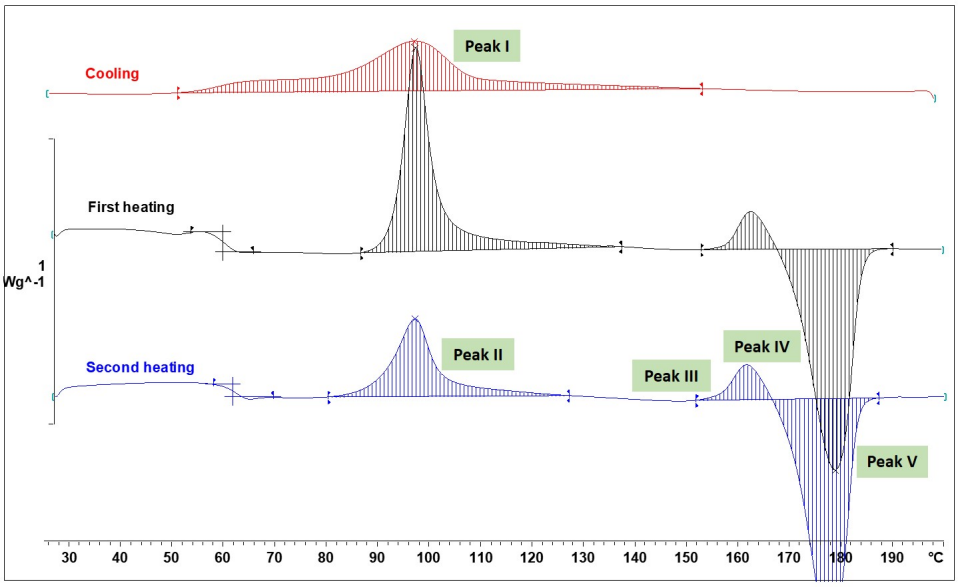

Figure 4.1: DSC scan of PLA 2500HP semicrystalline neat extruded and identification of the different peaks.

Indeed, isothermal grown PLA crystals have a large tendency to reorganize into more stable structures, through continuous partial melting/recrystallisation/crystal perfection processes that occur during the subsequent heating scan that leads to fusion. When crystallisation is conducted at low temperatures, small and/or defective crystals develop, and low values of crystallinity are attained. The large

reorganisation of crystal phase results in a multiple melting behavior. Nevertheless, when high crystallisation rates are used, one single endothermic peak is detectable from calorimetric analyses.
The measurement of $T_{g,PLA}$ is not easy for such a semi-crystalline polymer that is to say to measure the temperature of the glass transition in the amorphous rigid interfacial region situated between the lamellar crystals and the amorphous phase is not easily observable. Thus, a first scan where the sample is heated above its T_m is done before quenching the sample and again reheated it to obtain the DSC thermogram during second heating scan and extracted data from this scan. Somehow, first heating scan is also meaningful because it reflects the thermal characteristics of the sample as produced after processing (extrusion).
The different DSC data T_g, T_m, $T_{coldcryst}$, T_{cryst}, T^*, ΔH_m, ΔH_m, $\Delta H_{coldcryst}$ and ΔH_{cryst} are calculated thanks to the *STARe* software and the value of T_g is taken as the midpoint temperature of the glass transition.

4.1.1.1.1 Semicrystalline PLA (PLA2500HP) - Lignin nanocomposites

The semicrystalline PLA received from NatureWorks (PLA2500HP) did not crystallise during cooling (see Figure 4.2). Moreover the PLA2500HP neat and not extruded as received from NatureWorks did not show any cold crystallisation during the first heating scan (see Figure 4.3). Indeed, the calculated degree of crystallinity of the neat not extruded PLA2500HP is about 37.43% which is nearly the maximum of crystallinity attainable for PLA according to the literature [47].
When the content of lignin in the blend increases, one can observe a decrease of $T_{m,blend}$ and $T_{g,blend}$ as shown in Figure 4.4, which indicates the existence of a intermolecular interaction between PLA and lignin [7]. As a matter of fact hydrogen bonds are formed between phenolic hydroxyl groups of lignin and the carbonyl groups of PLA. The phenolic hydroxyl groups of lignin have a strong ability to form strong intermolecular hydrogen bonds with carbonyl groups of esters. Those specific interactions are responsible for the formation of miscible blend of PLA and lignin. A decrease of T_m and T_g of on average $0.114°C$ per % of lignin added and $0.066°C$ per % of lignin added are respectively observed.
The observation of a single composition-dependent T_g between those of the pure components is usually the evidence of miscibility [7, 22]. But as lignin does not really show glass transition or melting phenomena, the terms "miscibility" or "immiscibility" are not truly appropriate to describe the system. $T_{g,lignin}$ is described in the literature as near the onset of the $T_{m,PLA}$ [7].
Lignin seems to act as a nucleating agent when its weight percentage increases to 10%. When increasing further the content of lignin, the degree of crystallisation χ_c keeps increasing (see Table 4.1).

$\Delta H_{coldcryst}$ is an exothermic enthalpy that is absorbed by crystals growth during heating. Cold crystallisation is linked to rapid cooling of the melt in the mould cavity during injection moulding [49]. As demonstrated by Figure 4.4 cold crystallisation happens at higher temperature with increasing content of lignin in the blend.

If a slower cooling/heating DSC measurement is done on PLA, the cooling scan shows different peaks of crystallisation depending on the different crystalline phases of PLA. However the heating scan presents only one recrystallisation because in this situation, one lets the time to the system to reorganise and thus the exothermic peak just before the melting peak is not observed [7].

Table 4.1: DSC results of First scan of PLA 2500HP - Lignin blends. T^* is the temperature of the exothermic peak before melting and $\Delta H_m^0 = -93.7\,[J/g]$ is the melting enthalpy of a completely (100%) crystalline PLA [3, 11].

	T_g $[°C]$	$T_{coldcryst}$ $[°C]$	$\Delta H_{coldcryst}$ $[J/g]$	T^* $[°C]$	T_m $[°C]$	ΔH_m $[J/g]$	χ_c [%]
1	68.6	/	/	166.1 (or /)	179.3	35.09	37.4
2	60.8	97.3 (or /)	27.59 (or /)	160.5 (or /)	177.9	39.13	12.3
3	58.6	96.4	28.56	163.2	177.3	36.92	9
4	58.4	96.12	32.08	161.4	177.4	37.83	6.5
5	/	/	/	157	175.3	39.48	46.8
6	/	/	/	155.9	174.2	36.69	48.9
7	/	/	/	154.7	174	33.07	50.4

Table 4.2: DSC results of PLA 2500HP - Lignin blends from Cooling and Second heating.

	T_g $[°C]$	$T_{coldcryst}$ $[°C]$	$\Delta H_{coldcryst}$ $[J/g]$	T_m $[°C]$	ΔH_m $[J/g]$	T_{cryst} $[°C]$	ΔH_{cryst} $[J/g]$
1	61.1	122.1	25.15	176.4	20.27	/	/
2	60.0	98.4	21.94	177	39.57	96.9 (or /)	19.1
3	61	96.4	18.99	176	39.16	98	19.19
4	60.4	96.2	19.01	176.3	39.74	97.6	20.06
5	59.6	98.8	35.06	174.9	38.5	/	/
6	58.8	107.3	34.53	175	35.95	/	/
7	58.2	111.8	33.71	174.7	34.24	/	/

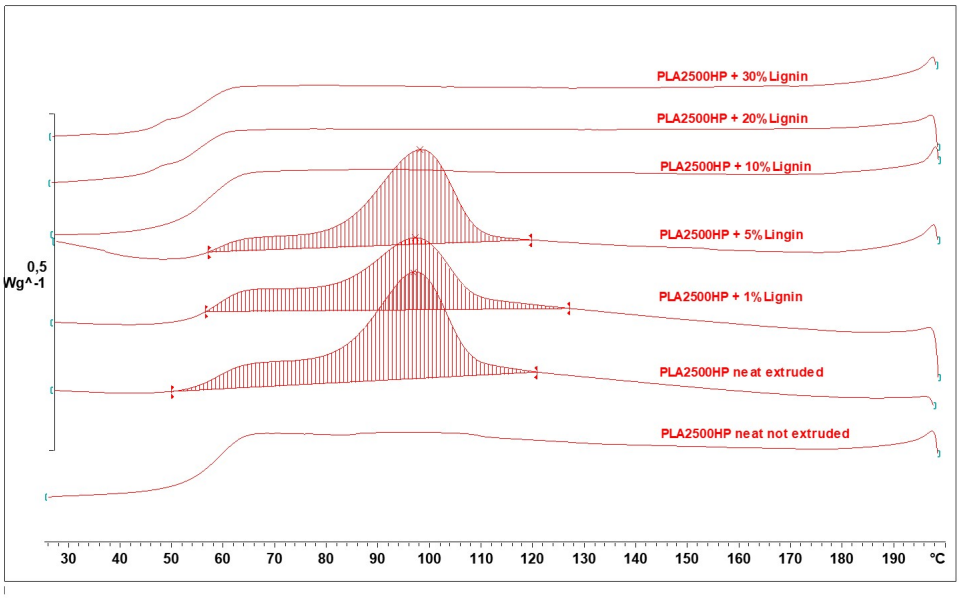

Figure 4.2: DSC Cooling heating scans curves of PLA 2500HP - Lignin blends.

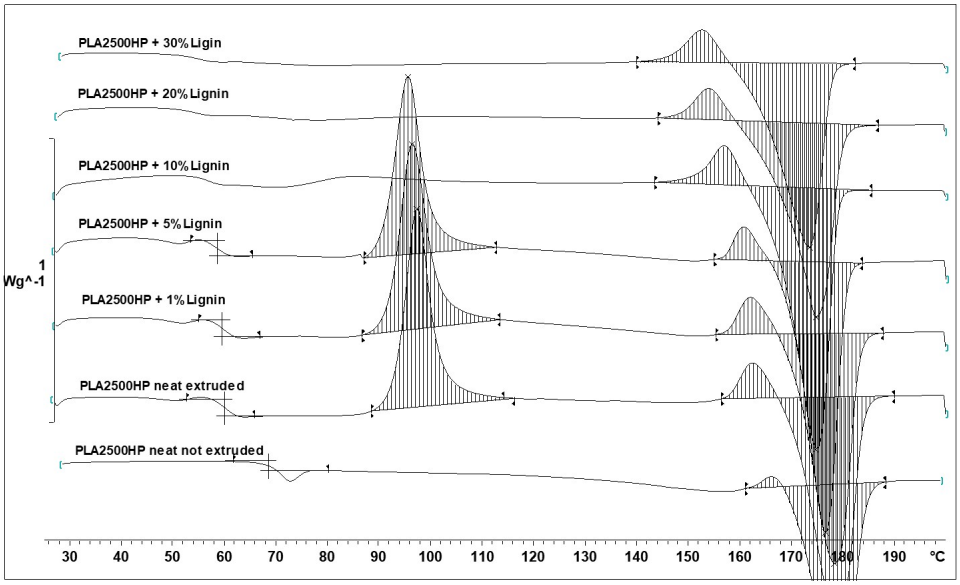

Figure 4.3: DSC First heating scans curves of PLA 2500HP - Lignin blends.

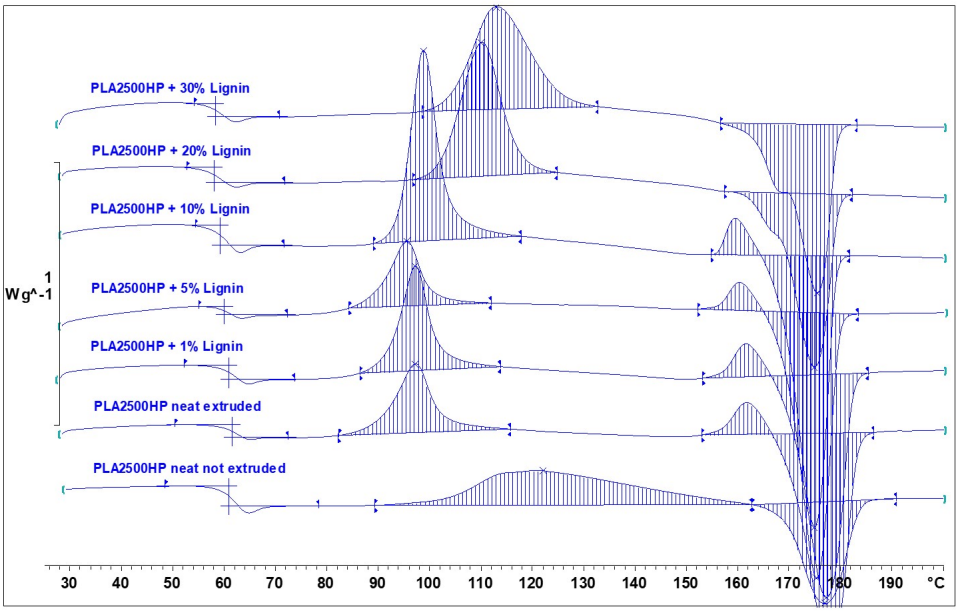

Figure 4.4: DSC Second heating scans curves of PLA 2500HP - Lignin blends.

4.1.1.1.2 Amorphous PLA (PLA4060D) - Lignin nanocomposites

The data collected from the DSC analysis of blends with the amorphous PLA are

summarised in Table 4.3. Again fluctuations of baseline are due to poor thermal contact between the crucible and the pellet. The DSC scans for the amorphous PLA are illustrated in Figure 4.5, Figure 4.6 and Figure 4.7.
In accordance with the literature the value of T_g of amorphous PLA (PLA4060D) is lower than the one of the semicrystalline PLA. The endothermic peak observed at T_g for some DSC scans (see Figure 4.7 and Figure 4.6) is due to the relaxation of stresses coming from processing/extrusion.
As for the semicrystalline PLA, when lignin is added to the amorphous PLA (PLA4060D), $T_{g,blend}$ decreases which indicates the existence of the same intermolecular hydrogen bonds between PLA and lignin. The decrease of $T_{g,blend}$ is of on average $0.138°C$ per % of lignin added.

Table 4.3: DSC results for PLA4060D - Lignin blends.

	$T_{g,firstheating}$ $[°C]$	$T_{g,secondheating}$ $[°C]$
8	58.9	56.9
9	56.2	56.4
10	55.1	55.9
11	54.5	55.8
12	53.8	55.1
13	51.4	54.4
14	50.3	53.9

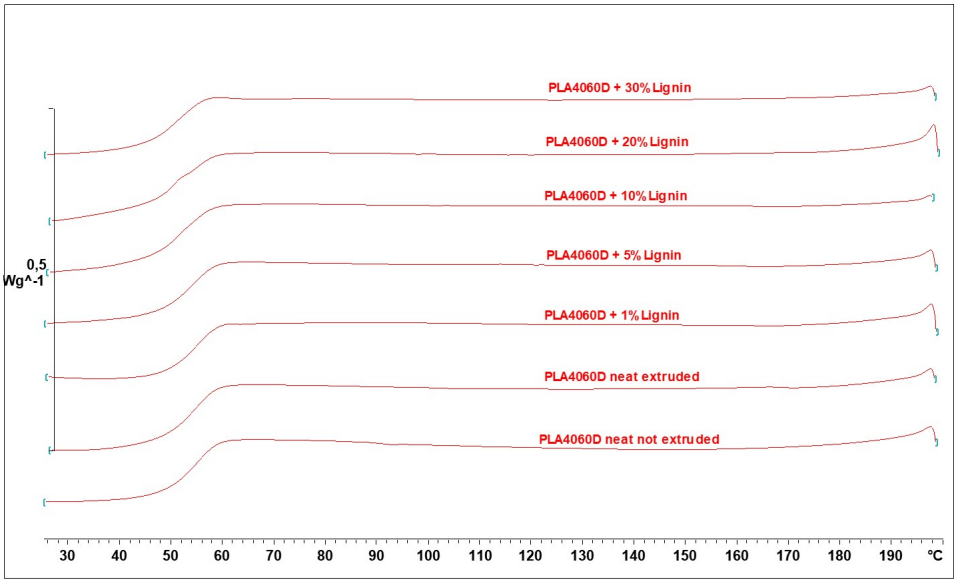

Figure 4.5: DSC Cooling heating scans curves of PLA 4060D - Lignin blends.

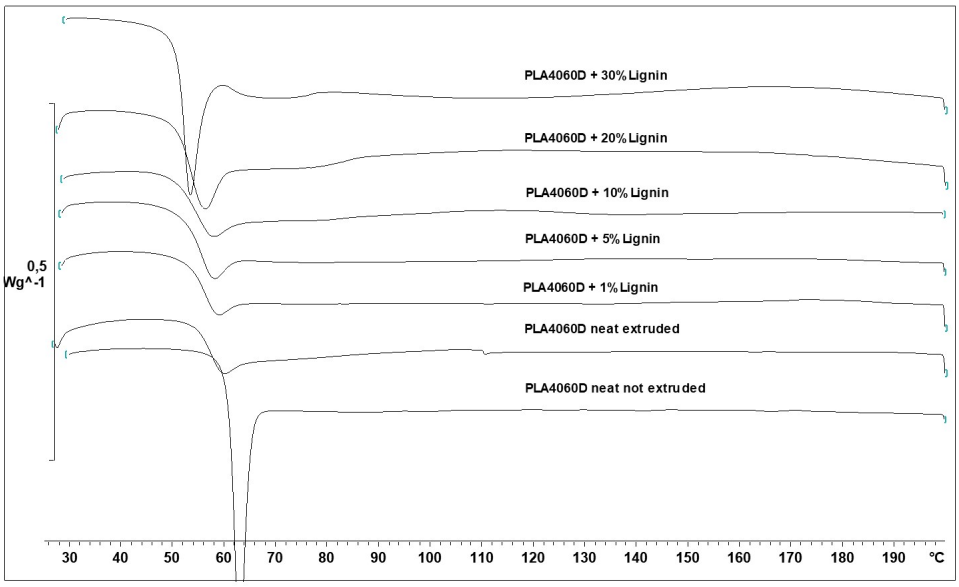

Figure 4.6: DSC First heating scans curves of PLA 4060D - Lignin blends.

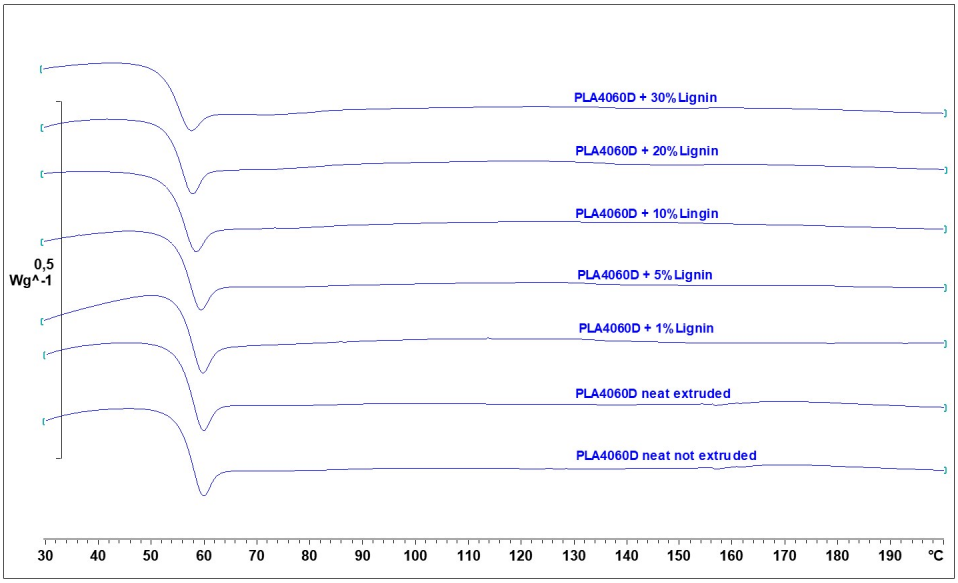

Figure 4.7: DSC Second heating scans curves of PLA 4060D - Lignin blends.

4.1.1.1.3 Semicrystalline PLA (PLA2500HP) - Flax nanocomposites

The data collected fron the DSC scans of PLA 2500HP - flax blends are listed in Table 4.4 nd Table 4.5. The DSC curves illustrated in Figure 4.8, Figure 4.10 and Figure 4.9 reveal an increase of $T_{crystallisation}$ and an increase of the enthalpy of crystallisation ΔH_c. There is also an increase of the degree of crystallinity χ_c when the content of flax increases.
Increasing content of flax results in a decrease of $T_{cold\ crystallisation}$ and enthalpy of cold crystallisation $\Delta H_{cold\ crystallisation}$.
As for PLA - Lignin blends T_g and T_m seems to decrease with increasing flax content which indicates the existence of a specific intermolecular interaction between PLA and Flax fibers.
Moreover the degree of crystallinity of PLA2500HP blend with $10wt\%$ of flax added $\chi_c = 49.3\%$ is close to the one of PLA2500HP blend with $10wt\%$ of lignin added $\chi_c = 46.8\%$.

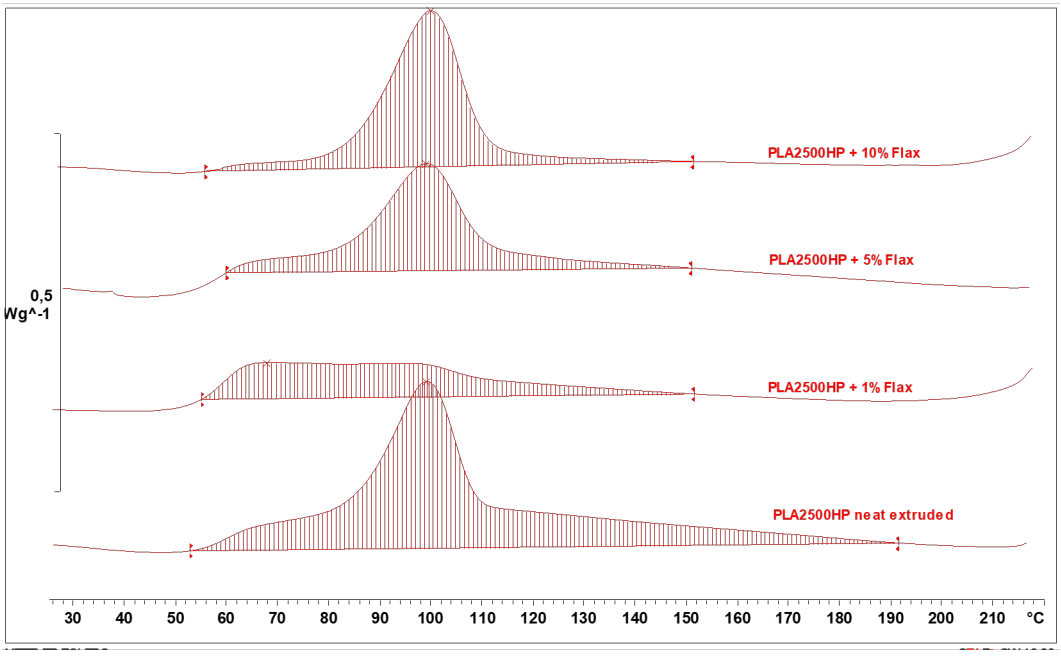

Figure 4.8: DSC Cooling scans of PLA 2500HP - Flax blends with different weight percentage realised by *Rajendar Nutenki*.

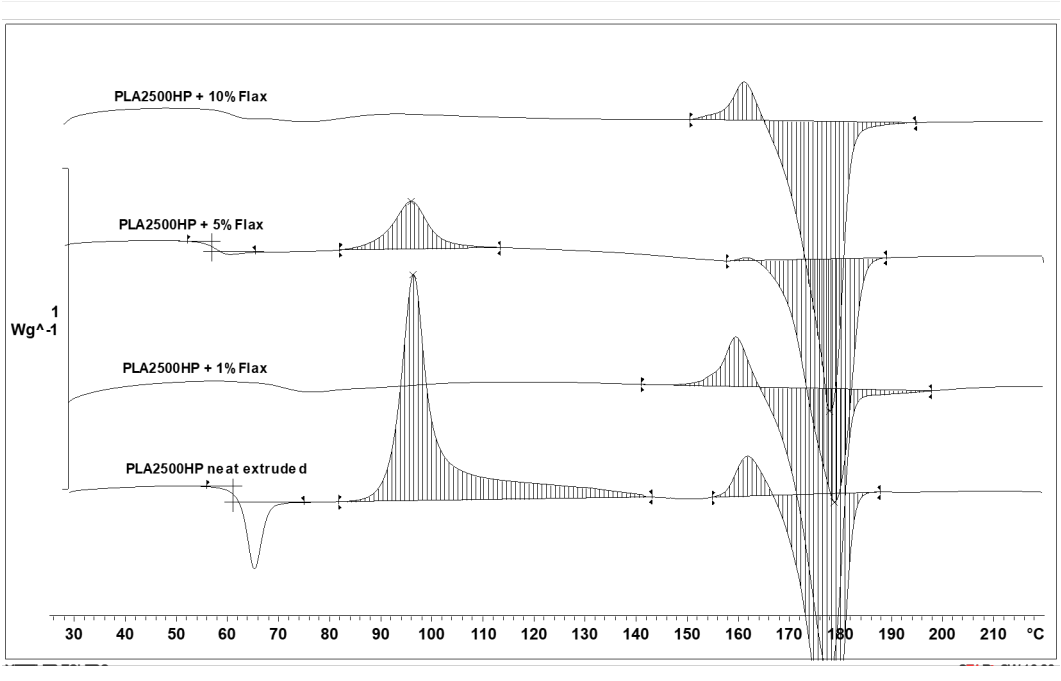

Figure 4.9: DSC First heating scans of PLA 2500HP - Flax blends with different weight percentage realised by *Rajendar Nutenki*.

Table 4.4: DSC results of PLA 2500HP - Flax blends from Cooling and First heating.

	T_g $[°C]$	$T_{coldcryst}$ $[°C]$	$\Delta H_{coldcryst}$ $[J/g]$	T_m $[°C]$	ΔH_m $[J/g]$	T_{cryst} $[°C]$	ΔH_{cryst} $[J/g]$	χ_c $[\%]$
Neat extr.	63.7	96.4	24.6	178	35.3	99	23.4	11.4
1%	71	/	/	178.5	35.4	65.7	14.9	38.2
5%	60.6	96	6.63	178.9	44.02	98.8	21.65	42
10%	/	/	/	177.8	41.6	100.1	28.06	49.3

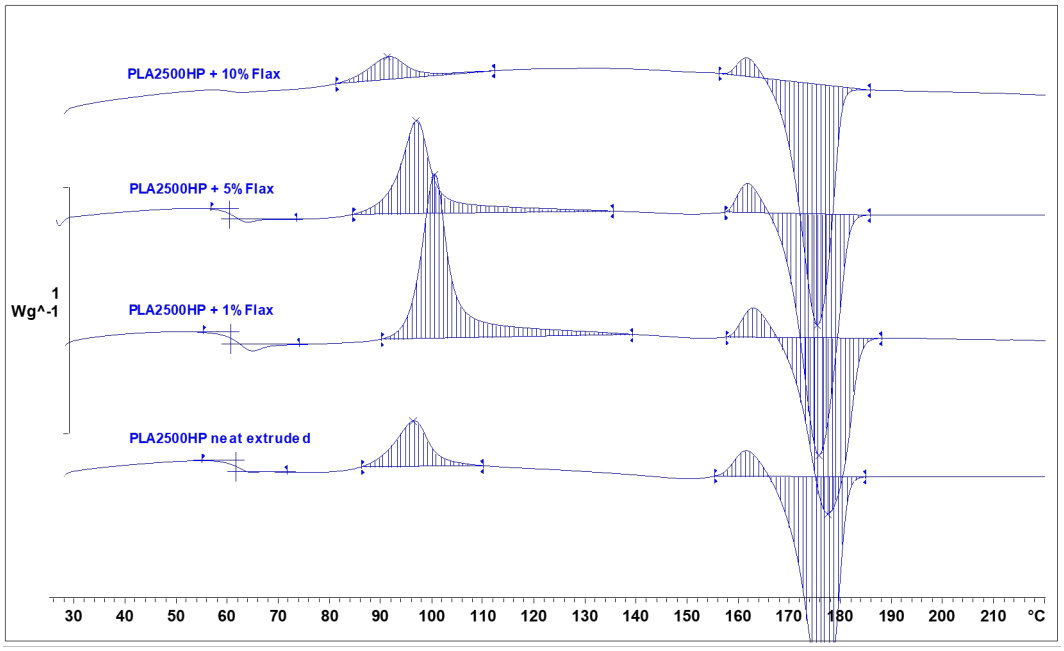

Figure 4.10: DSC Second heating scans of PLA 2500HP - Flax blends with different weight percentage realised by *Rajendar Nutenki*.

Table 4.5: DSC results of PLA 2500HP - Flax blends from Second heating.

	T_g $[°C]$	$T_{coldcryst}$ $[°C]$	$\Delta H_{coldcryst}$ $[J/g]$	T_m $[°C]$	ΔH_m $[J/g]$	χ_c $[\%]$
Neat extr.	61.6	96.4	11.8	176.6	38.05	28.01
1%	61.6	100.6	25.12	177.5	34.02	9.4
5%	61.6	96.9	17.82	175.8	42.13	25.94
10%	/	91.4	2.78	175.8	36.6	36.09

4.1.1.1.4 PHBV - Flax nanocomposites

Poly(3-hydroxybutyrate-co-3-hydroxyvalerate) has improved characteristics compared to poly(β-hydroxybutyrate) (PHB) such as better flexibility and strength, reduced chain packing and toughness. Additionally, the increase in the amount of HV in the PHB polymer leads to a more amorphous structure. Poly(3-hydroxybutyrate-co-3-hydroxyvalerate) known as PHBV is a biodegradable, biocompatible and environmentally friendly polymer which has a low thermal stability and is brittle due to high degree of crystallinity [92, 93].

The data collected from the DSC scans of PHBV - flax blends are listed in Table 4.6 and Table 4.7. The DSC scans are illustrated in Figure 4.11, Figure 4.13 and Figure 4.12. The data show an increase of $T_{crystallisation}$ and an increase of the enthalpy of crystallisation ΔH_c when a small amount flax is added and when the content of flax increases then $T_{crystallisation}$ and ΔH_c decrease. In addition an increase of the degree of crystallinity χ_c is observed when the content of flax increases. However PHBV extruded is already quite crystalline $\chi_c = 45.7\%$ compared to neat extruded semicrystalline PLA $\chi_c = 12.32\%$.
Data are not so clear to conclude about the evolution of $T_{cold\ crystallisation}$ and enthalpy of cold crystallisation $\Delta H_{cold\ crystallisation}$ with increasing content of flax. The particularity of PHBV is that there it has two distinct T_m. There is no clear decrease or increase of T_g and T_m's observed with addition of flax.
There is an increase of the degree of crystallinity χ_c when the content of flax is smaller than 10% then it decreases.

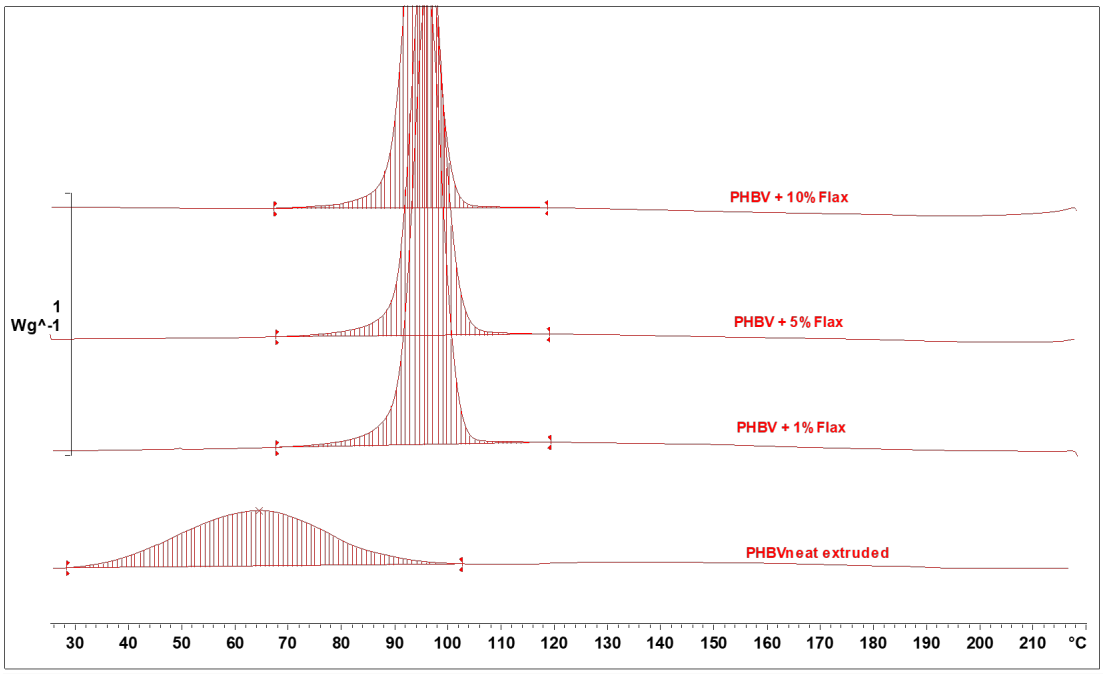

Figure 4.11: DSC Cooling scans of PHBV - Flax blends with different weight percentage realised by *Rajendar Nutenki*.

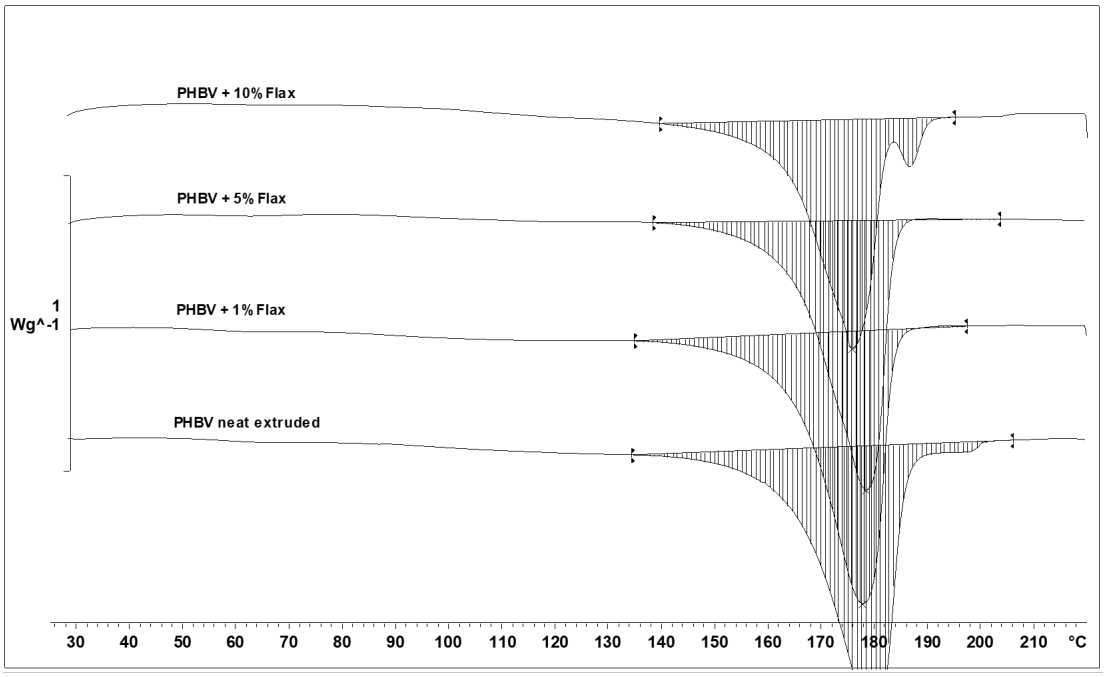

Figure 4.12: DSC First heating scans of PHBV - Flax blends with different weight percentage realised by *Rajendar Nutenki*.

Table 4.6: DSC results of PHBV - Flax blends from Cooling and Second heating.

	$T_{coldcryst}$ $[°C]$	$\Delta H_{coldcryst}$ $[J/g]$	T_{m1} $[°C]$	T_{m2} $[°C]$	ΔH_m $[J/g]$	ΔH_m^0 $[J/g]$	χ_c $[\%]$
Neat extr.	47.9	9.94	172.4	/	76.63	146	45.7
1%	/	/	164.6	173.3	75.58	146	52.29
5%	/	/	165.4	176.9	73.46	146	52.9
10%	/	/	164.5	173.3	64.48	146	49.1

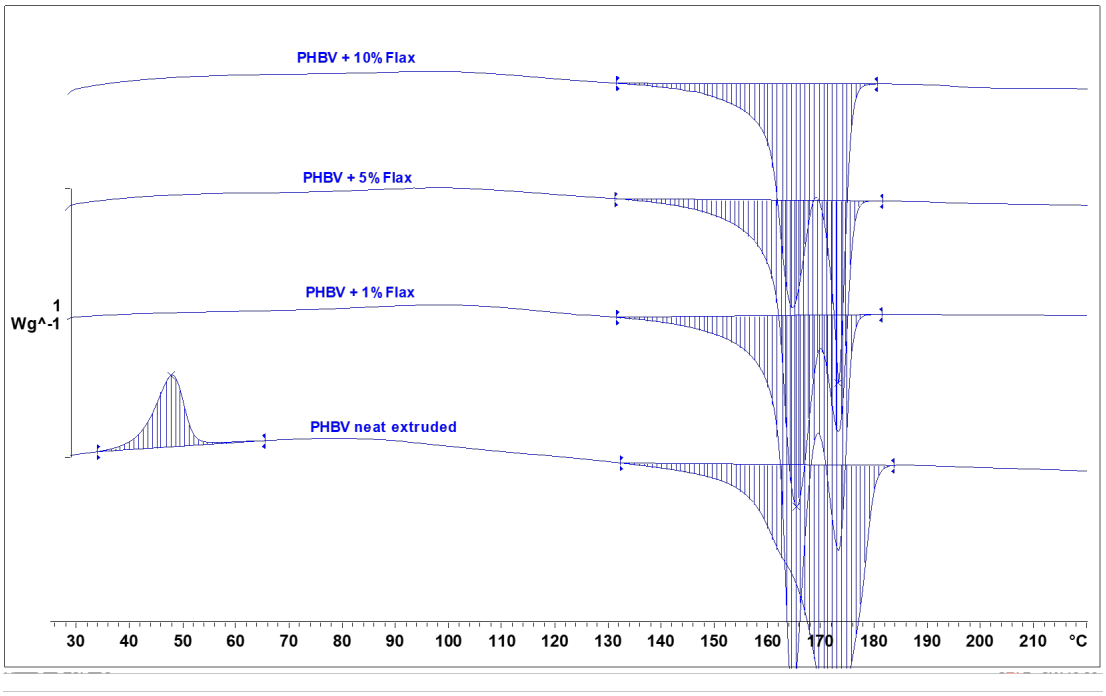

Figure 4.13: DSC Second heating scans of PHBV - Flax blends with different weight percentage realised by *Rajendar Nutenki*.

Table 4.7: DSC results of PHBV - Flax blends from First heating.

	T_m $[°C]$	ΔH_m $[J/g]$	T_c $[°C]$	ΔH_c $[J/g]$	ΔH_m^0 $[J/g]$	χ_c $[\%]$
Neat extr.	175.8	76.01	64.6	37.51	146	52.06
1%	178.5	76.72	96.1	71.14	146	52.54
5%	177.8	85.09	96	69.49	146	58.28
10%	177.8	96.67	94.7	59.12	146	66.21

4.1.1.2 TGA Analysis

The different TGA data are evaluated thanks to the *STARe* software.
The data collected thanks to Thermogravimetry analysis show that pure lignin starts around $135°C$ and degrades significantly over a broad range of temperatures starting at $220°C$ but is not fully degraded up to $600°C$ as illustrated by Figure 4.14 which is consistent with literature. This slow degradation is due to the presence of various oxygen functional groups from the lignin structure having different thermal

stabilities, their scission occurring at different temperatures [56]. The bottom part of Figure 4.14, called the DTG curve, is obtained by deriving the TGA curve. The DTG curve expresses the speed at which the sample loses weight. It highlights easily the small weight losses or potential curve's shoulder. In the case of lignin, the lignin's maximum speed of degradation is around $350°C$.

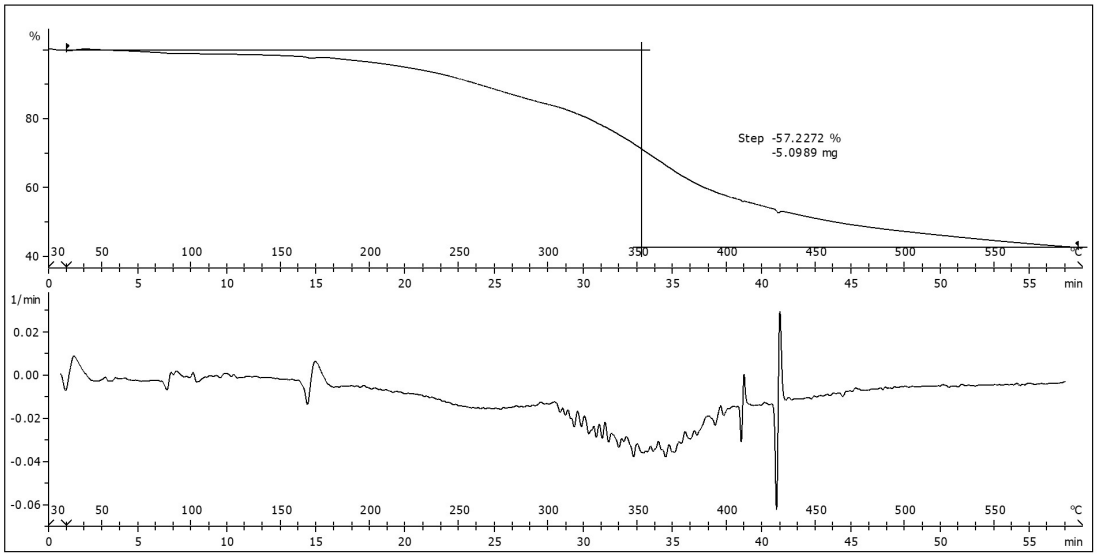

Figure 4.14: TGA curve of pure lignin.

According to literature the starting point of thermal degradation T_s is defined as the temperature at which the net weight loss of the PLA is 5% either in the pure state or in blends when the effect of PLA on the degradation of lignin is neglected.

The TGA curve of the different PLA2500HP - lignin blends are illustrated in Figure 4.15 and data extracted from those curves are reported in Table 4.8. The TGA realised on semicrystalline PLA (2500HP) shows that T_s is around 325°C and that PLA2500HP is thermally stable up to 300°C. As expected only one degradation mechanism is observed for PLA. From the DTG curve, the maximum speed of degradation of neat PLA is observed around 372°C and 99.3% of mass was degraded at the end of the experiment.
When the content of lignin increases, the curves of PLA with lignin are similar to the one of pure PLA2500HP; only one degradation mechanism is observed which is quite unexpected. The maximum speed of degradation is between 355°C and 372°C. When lignin content is 10% or 20%, T_s decreases from 325°C to ±310°C which is a slight decrease. For a content of lignin of 30%, T_s decreases to 278°C.
In literature, curve of PLLA (semi-crystalline) with lignin contents of 0%, 10% and 20% overlapp from the starting point until the degrading stage. When the temperature is higher than 365°C, the difference between these three curves is due to almost entirely lignin residue. When content of lignin is no more than 20%, lignin has no obvious influence on the degradation of PLA and T_s remains about 308°C. However when the lignin content is more than 20%, T_s clearly decreases, lignin has thus a destabilizing effect on PLA. When the content of lignin was 40%, T_s was only 289°C [7].

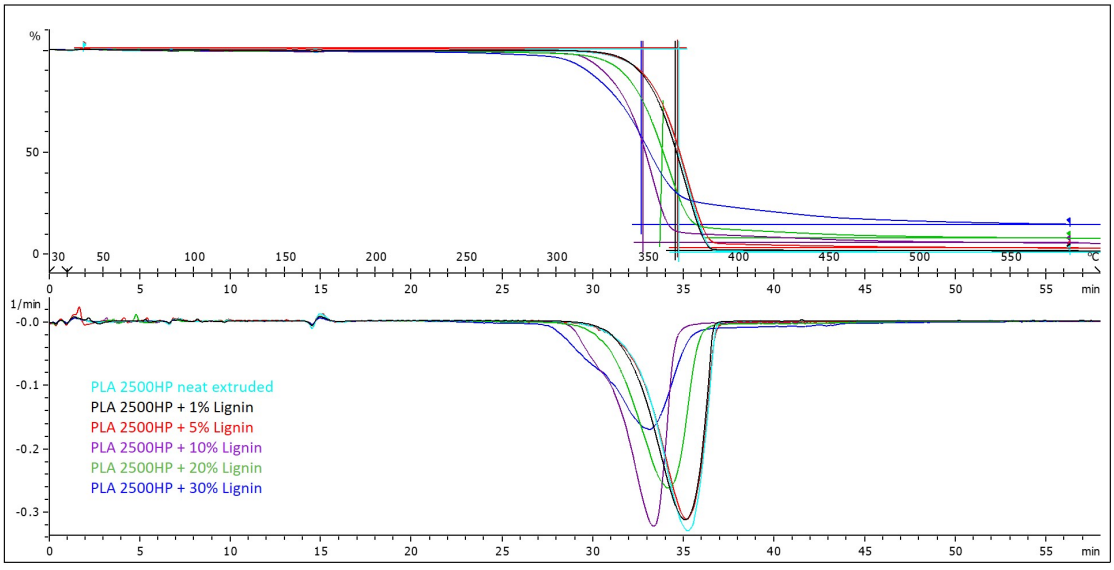

Figure 4.15: TGA curves of PLA 2500HP - Lignin blends.

Table 4.8: TGA results of PLA2500HP - Lignin blends.

	$T_s\,[°C]$	$T_{maximum\ speed\ of\ degradation}\,[°C]$
Neat extr.	325	372
1%	328	370.5
5%	326	371
10%	309	355
20%	310	362
30%	278	356

The TGA curve of the different PLA4060D - lignin blends are illustrated in Figure 4.16 and data extracted from those curves are reported in Table 4.9. The TGA realised on amorphous PLA (4060D) shows that T_s is around $330°C$ and that PLA 4060D is thermally stable up to $300°C$ comparably to PLA2500HP. Again only one degradation mechanism is observed for PLA4060D - lignin blends which is not what would be expected since lignin was added. The maximum speed of degradation is observed around $372°C$ and 98.5% of mass was degraded for PLA 4060D neat extruded.
When the content of lignin increases, the curves of PLA with lignin are similar to the one of pure PLA4060D. The maximum speed of degradation is between $349°C$ and $373°C$. When lignin content is 5%, 10% or 20%, T_s decreases from $330°C$ to $302 - 313°C$ which is a slight decrease. For a content of lignin of 30%, T_s decreases to $272°C$.

Table 4.9: TGA results of PLA4060D - Lignin blends.

	$T_s\,[°C]$	$T_{maximum\ speed\ of\ degradation}\,[°C]$
Neat extr.	330	372
1%	331	373
5%	313	361
10%	309	360
20%	302	342
30%	272	349

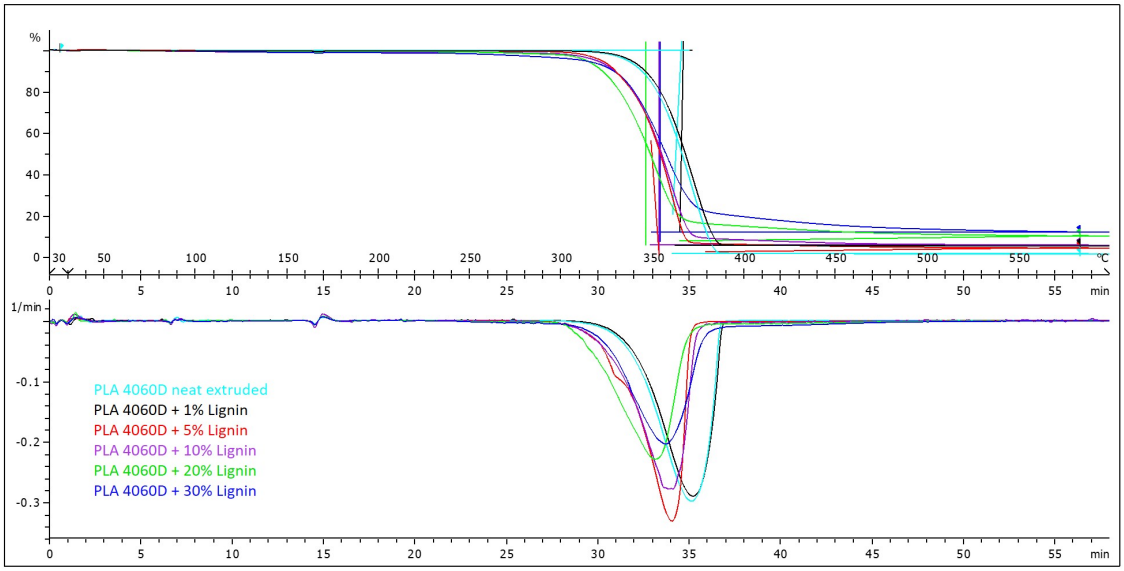

Figure 4.16: TGA curves of PLA 4060D - Lignin blends.

4.1.2 Mechanical characterisation

4.1.2.1 Tensile Test

Values of characteristic mechanical properties are calculated as described in Chapter 2 following the ISO527 standard.
True stress-strain curves for the PLA2500HP and PLA4060D - Lignin blends were drawn using Matlab and are displayed in Figure 4.21 and Figure 4.22. Warping and/or buckling of some samples realised with injection moulding occurred during removal of the specimen from the mould. Though most of them were straight.
The stress-strain (normal and true) curves for each specimen tested are shown in the appendix (Chapter 6).
In the stress-strain curves, two main deformation regions are identified: an elastic and a plastic deformation regions. The elastic deformation ensues in two mechanisms in thermoplastics. The stress applied leads to stretching and distortion of the covalent bonds within the chain, leading to elastic elongation of chains. Recovery from the deformation is almost immediate when stress is removed. If entire segments of polymer chains are distorted, the chains go back to their initial position over a period of time when stress is removed. This is characteristic of the viscoelastic (time-dependent) behavior of polymers. Beyond yield point which is the stress that causes a material to permanently deform [68], the polymer deforms plastically. Plastic deformation is induced by chains sliding, stretching, rotating

and disentangling under load causing permanent deformation [43, 94].

In polymers different strength-limiting processes are known. Polymers are brittle below $0.75T_g$. Polymers are thus low-toughness materials. Figure 4.17 depicts the stress-strain curve in the case of a brittle fracture [42].

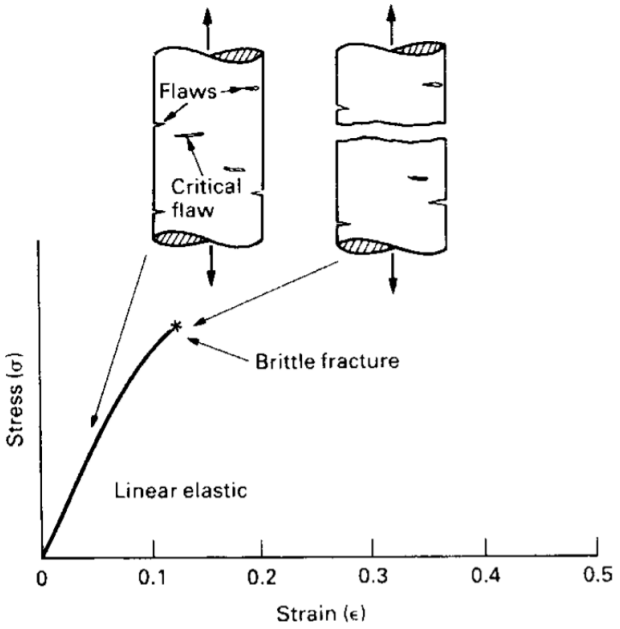

Figure 4.17: Brittle fracture in thermoplastics [42].

Thermoplastic becomes plastic at temperatures around $50°C$ or below T_g. The stress-strain curve (see Figure 4.18) in this case shows three regions. First the polymer is linear elastic at low strains. Then it yields and draws. During cold drawing the chains unfold or draw out of the amorphous tangle (if the polymer is glassy). Drawing starts at a point of stress concentration or weakness: a part of the gauge length draws down (similarly as necking). The neck spreads along all the sample until it is all drawn. The neck propagates instead of simply causing failure because the material is now stronger in the draw direction than before. Next the chains straighten and align which causes draw-strengthening [42].

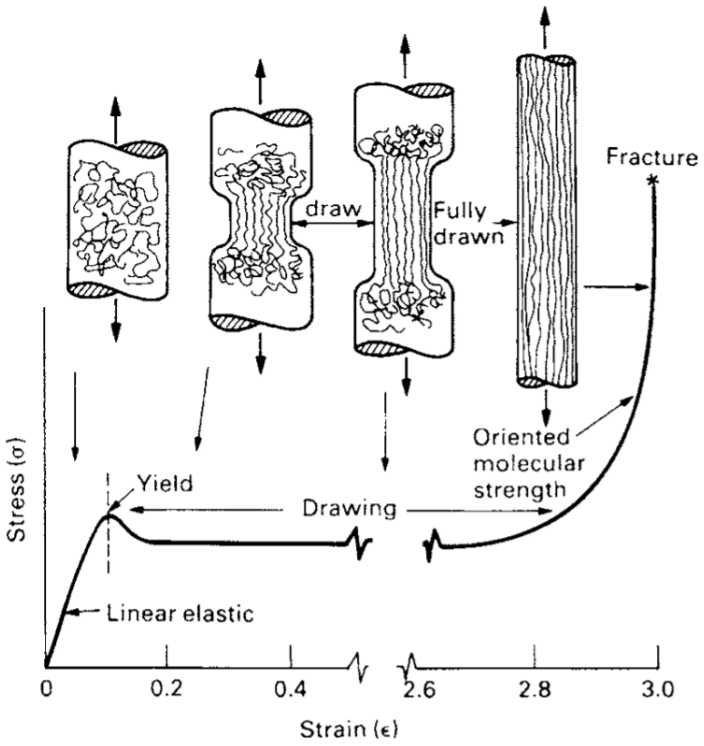

Figure 4.18: Cold-drawing of a linear polymer [42].

When the yield strength is exceeded, there is a drop in stress because entangled chains become straight and untangled. Then additional stress causes necking in which sliding and deformation of chains continue. Necking is a type of deformation where strain localises in a region of the specimen. The point for onset of necking can be determined by a local increase in temperature or by a structural or material imperfection. A necessary but not sufficient condition for necking is the presence of a local maximum on nominal stress-strain curve [95].
In amorphous polymers continuous necking induces the chains to get closer together

and almost parallel. Strong Van der Waals forces between the closely aligned chains necessitate higher stress to continue the fracture process. For semi-crystalline polymers the plastic deformation process is different and is illustrated in Figure 4.19.

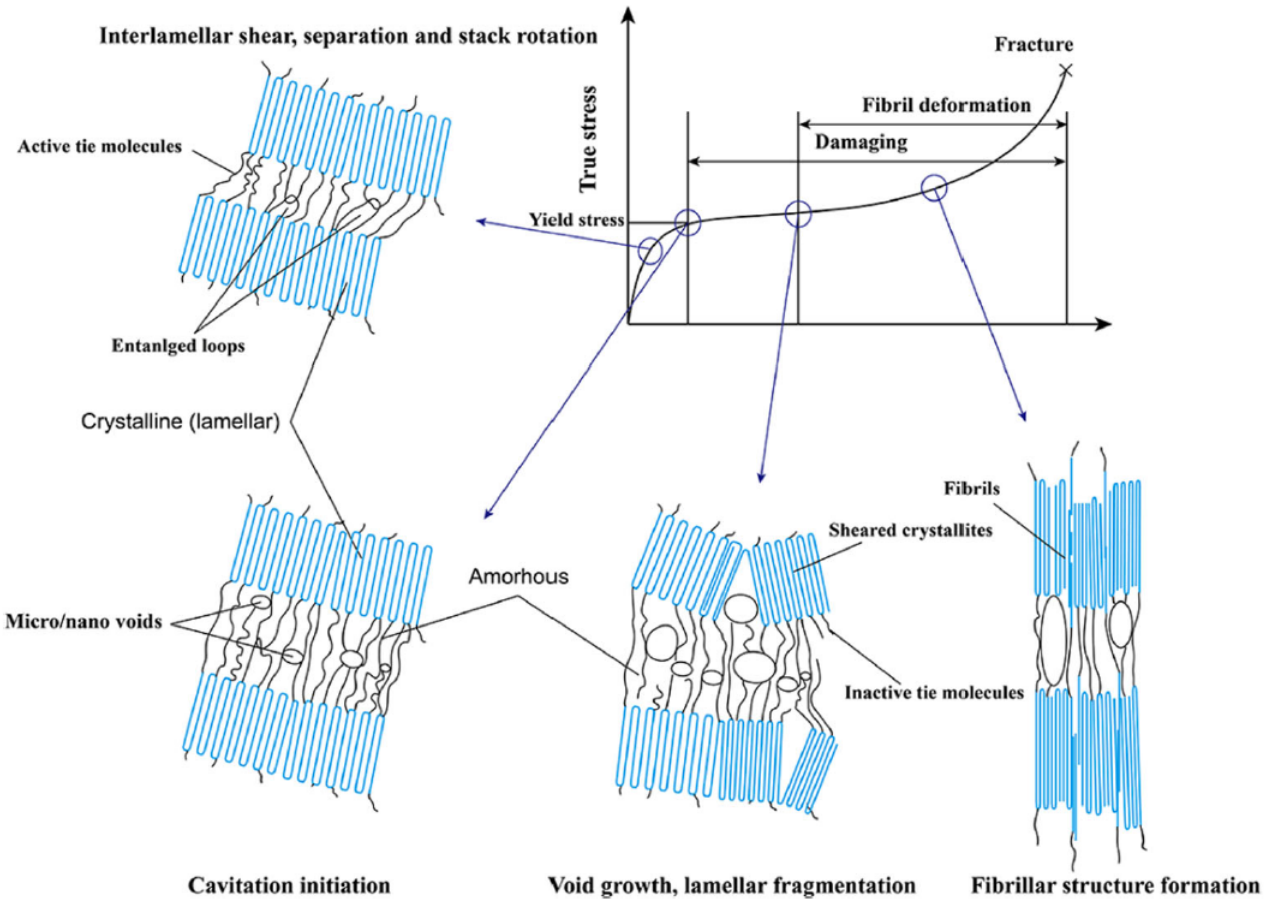

Figure 4.19: Schematic description of the true stress–strain relationship of semi-crystalline polymers and the evolution of microstructure [43].

Higher T_g thermoplastics loaded in tension craze at room temperature. Small crack-shaped domains inside the polymer draw down. However they are constrained by the surrounding undeformed solid, strands bridging the craze surfaces (microcracks) appear (see Figure 4.20). Craze is visible as white streaks or general whitening. Crazes precede fracture: a crack forms at the centre of a craze and then propagates prior to general drawing [42].

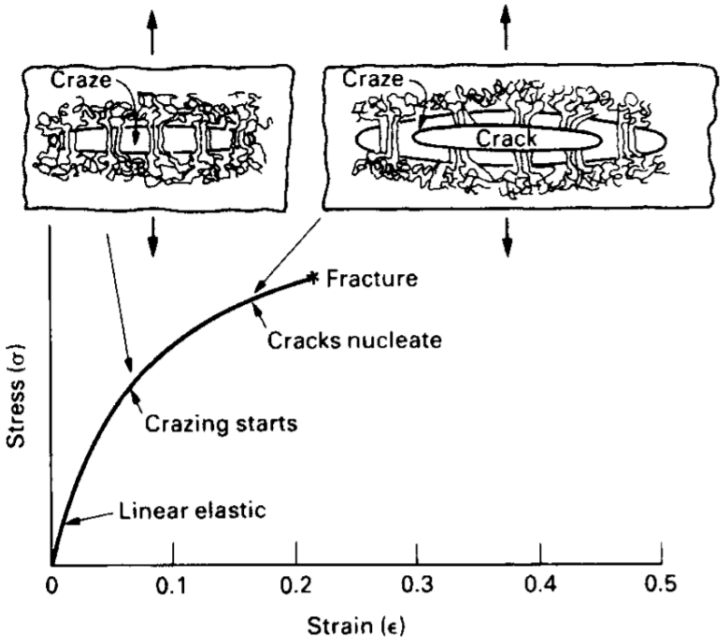

Figure 4.20: Crazing in a linear polymer [42].

Stress-strain curves for the semi-crystalline PLA are characterised by a linear elastic region, a yielding followed by a drop in stress, a formation of a neck, and finally fracture. As PLA is a quite brittle thermoplastic, stress-strain curves of semi-crystalline PLA does not show an increase in stress due to straightening of polymer chains. Regarding stress-strain curves for the amorphous PLA, they are characterised by a linear elastic region, a yielding followed by a drop in stress, a formation of a neck, a drawing of the neck and finally fracture [43, 94].

With addition of lignin in PLA matrix σ_{max}, ε_{max} and ε_b decrease. Nevertheless E remains almost the same over a lignin content up to 20%. As observed by comparison of Table 4.10 and Table 4.11, a slightly lower E for PLA4060D amorphous than for PLA2500HP semicrystalline and slightly higher ε_b for PLA4060D amorphous are observed corresponding to what was expected. E is around $3-4MPa$ corresponding to what the literature says.
The reductions of the mechanical properties of the PLA-Lignin blends could be attributed to the presence of lignin particles (see 4.1.4). Indeed the manual mixing can not make the two polymer components blend at molecular level but only at the macroscopic level, irrespective of the PLA-lignin intermolecular hydrogen-bonding interaction. To verify this hypothesis, SEM images of PLA with 5% lignin were realised. The size and the dispersion of lignin particules will be illustrated later in 4.1.4.

Table 4.10: Tensile test results for PLA semi-crystalline 2500HP - Lignin blends.

PLA2500HP	$E_t\,[GPa]$	$\sigma_{max}\,[MPa]$	$\varepsilon_{max}\,[\%]$	$\varepsilon_b\,[\%]$
SC-N (2)	3.72	70.1	2.33	3.21
SC-1L (3)	3.72	65.1	2.12	2.64
SC-5L (4)	3.82	62.1	1.96	2.13
SC-10L (5)	3.91	63.5	1.97	2.07
SC-20L (6)	3.93	49.4	1.4	1.4
SC-30L (7)	4.2	48.2	1.24	1.24

Table 4.11: Tensile test results for PLA amorphous 4060D - Lignin blends.

PLA4060D	$E_t\,[GPa]$	$\sigma_{max}\,[MPa]$	$\varepsilon_{max}\,[\%]$	$\varepsilon_b\,[\%]$
AM-N (9)	3.6	57	1.76	4.79
AM-1L (10)	3.63	55.8	1.91	5.62
AM-5L (11)	3.58	51.2	1.72	3.95
AM-10L (12)	3.76	49.9	1.53	1.76
AM-20L (13)	3.85	48.9	1.47	1.47

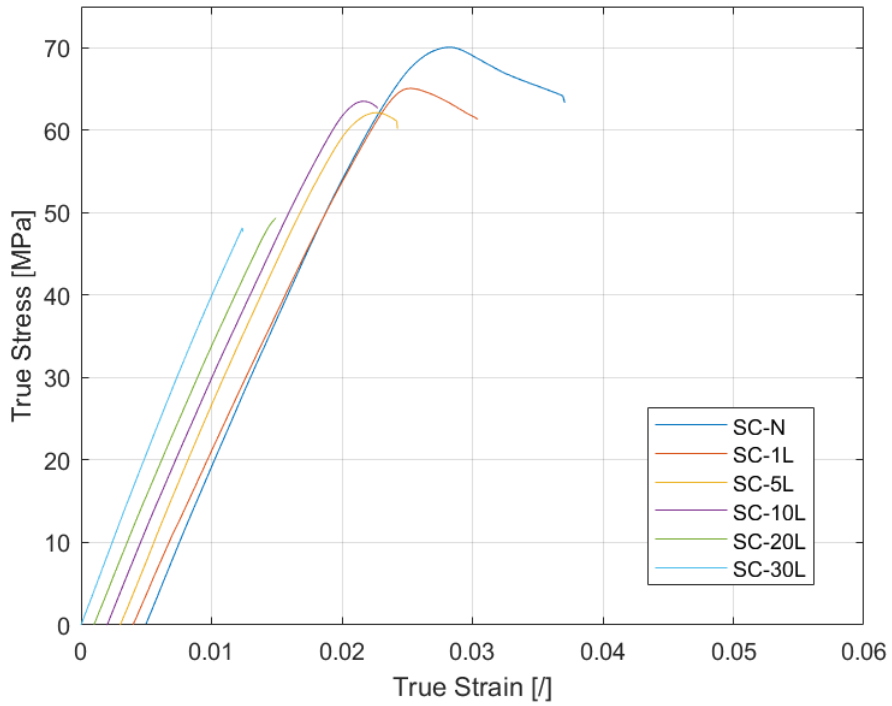

Figure 4.21: Stress-strain curves of the different PLA2500HP - Lignin blends drawn with Matlab illustrating the evolution of the mechanical properties. Curves have been deliberately shifted by 0.001 to the right with respect to each other to compare them easily.

Indeed for the PLA2500HP there is a slight increase of E of 12.9% with $30wt\%$ lignin addition and for PLA4060D, the slight increase of E is of 6.94% for $20wt\%$ lignin addition. The decrease of σ_{max} is higher for PLA2500HP (29.43% for the addition of $20wt\%$ lignin respectively) than for PLA4060D (14.2% for the addi-

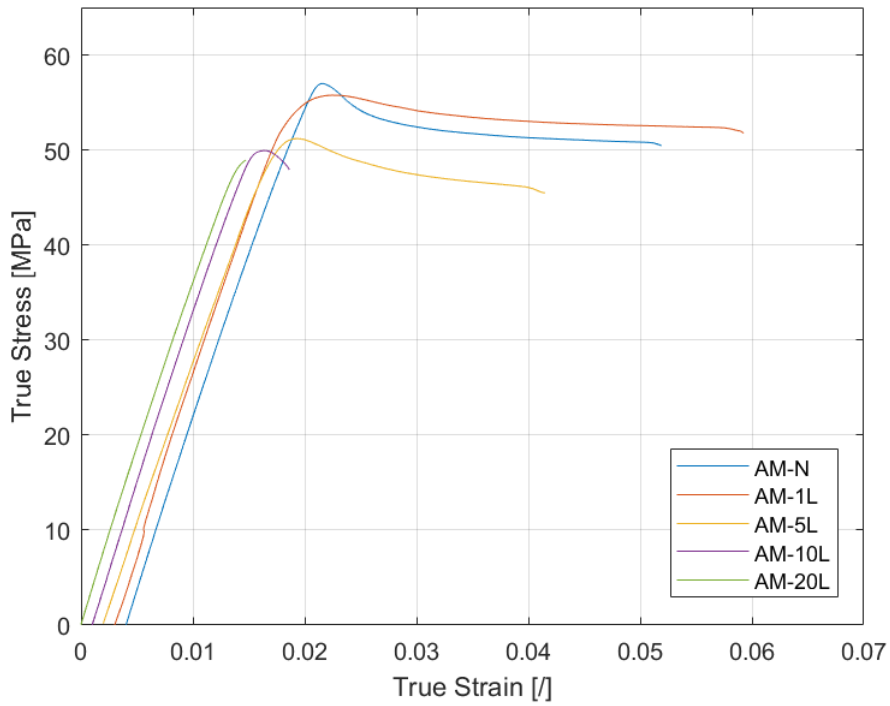

Figure 4.22: Stress-strain curves of the different PLA4060D - Lignin blends drawn with Matlab illustrating the evolution of the mechanical properties. Curves have been deliberately shifted by 0.001 to the right with respect to each other to compare them easily.

tion of $20wt\%$ lignin respectively). However the decrease of ε_b is higher for the amorphous PLA 528.92% and 69.31% for $20wt\%$ of lignin addition) than for the semicrystalline PLA (61.37% for $20wt\%$ of lignin addition).

4.1.2.1.1 PLA2500HP and PLA4060D - Flax blends

Stress-strain curves for the PLA2500HP and PLA4060D - Flax blends were drawn using Matlab and are displayed in Figure 4.23, Figure 4.24, Figure 4.25 and Figure 4.26. The results from Table 4.12 and Table 4.13 show that with flax fibers incorporation, the increase of E is more important and the decrease of σ_{max}, ε_{max} and ε_b is less important than with incorporation of lignin.

For the PLA2500HP, the increase of E is of 11.91% with $10wt\%$ flax fibers addition and for PLA4060D, the increase of E is of 11.2%. The decrease of σ_{max} is higher for PLA2500HP (13.6% for the addition of $10wt\%$ flax) than for PLA4060D (2.1%f or the addition of $10wt\%$ flax). For PLA2500HP ε_b decreases while for PLA4060D it increases slightly. However the decrease of ε_{max} is lower for the amorphous PLA (3.53% for $10wt\%$ of flax fibers addition) than for the semicrystalline PLA (18.45% for $10wt\%$ of flax fibers addition).

Table 4.12: Tensile test results for PLA semi-crystalline 2500HP - Flax blends.

PLA2500HP	$E_t\,[GPa]$	$\sigma_{max}\,[MPa]$	$\varepsilon_{max}\,[\%]$	$\varepsilon_b\,[\%]$
SC-5F	4.07	62.9	2	4.03
SC-10F	4.32	60.5	1.98	3.03

Table 4.13: Tensile test results for PLA amorphous 4060D - Flax blends.

PLA4060D	$E_t\,[GPa]$	$\sigma_{max}\,[MPa]$	$\varepsilon_{max}\,[\%]$	$\varepsilon_b\,[\%]$
AM-5F	4.04	53.6	1.68	5.52
AM-10F	4.15	55.8	1.7	5.68

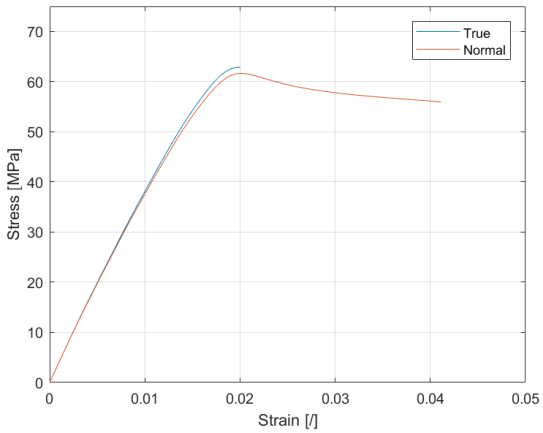

Figure 4.23: Stress-strain curves for PLA2500HP - 5wt%Flax blend.

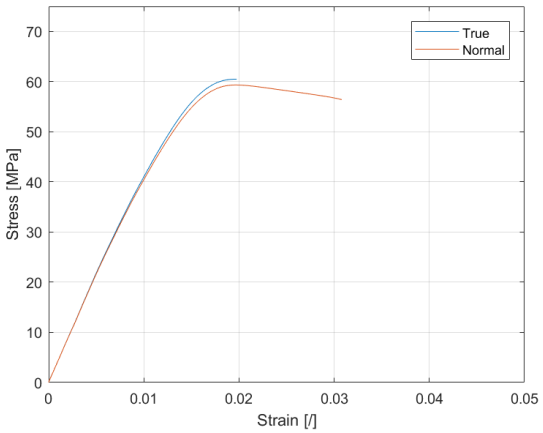

Figure 4.24: Stress-strain curves for PLA2500HP - 10wt%Flax blend.

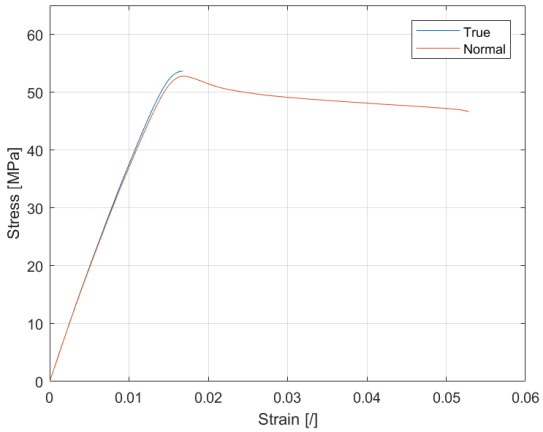

Figure 4.25: Stress-strain curves for PLA4060D - 5wt%Flax blend.

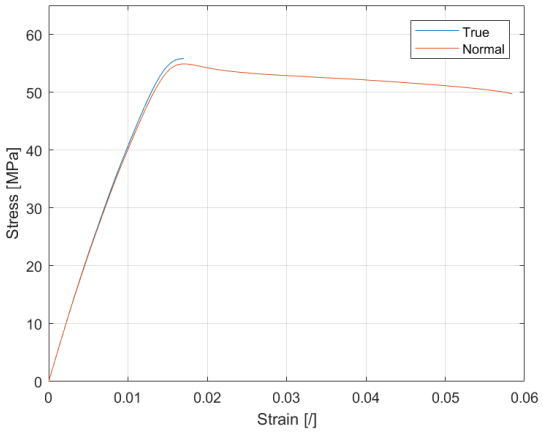

Figure 4.26: Stress-strain curves for PLA4060D - 10wt%Flax blend.

4.1.3 Dynamical mechanical analysis

The data from the DMA analysis are collected thanks to the *STARe* software. The value of T_g is determined as the temperature corresponding to the peak in $tan\delta$ vs T curve.

4.1.3.0.1 PLA - Lignin nanocomposites

The evolution of the storage modulus $E^{'}$, the loss modulus $E^{''}$ and the damping factor $tan\delta$ with the temperature of the different PLA2500HP - lignin blends are shown in Figure 4.27. One can observe first a decrease of $E^{'}$ around T_g. At a certain temperature above T_g, the value of $E^{'}$ increases due to cold crystallisation. The chains of the system which were in an amorphous state before have now enough time and energy to reorganise in a crystalline phase. This cold crystallisation leads to an increase of $E^{'}$.
For PLA2500HP - lignin blends, the value of $E^{'}$ and $E^{''}$ at $25°C$ and the value of T_g taken at the maximum of $tan\delta$ are listed in Table 4.14. An increase of storage modulus $E^{'}$ is observed as expected from DSC results. The increase of $E^{'}$ of 38.7% and 70% when respectively 10% and 20% of lignin is added. T_g decreases of 4.4% when 20% of lignin is added.

Table 4.14: DMA results for PLA semi-crystalline 2500HP - Lignin blends.

PLA 2500HP	$E^{'}_{max} \pm 150\,[MPa]$	$E^{''}\,[MPa]$	Maximum of $tan\delta$	$T_g\,[°C]$
SC-N (2)	3000	35	2.19	69.8
SC-1L (3)	3330	34	1.15	68.2
SC-5L (4)	3650	29	0.43	66.9
SC-10L (5)	4160	88	1.69	68
SC-20L (6)	5120	105	1.83	66.8
SC-30L (7)	5300	49	1.43	66.6

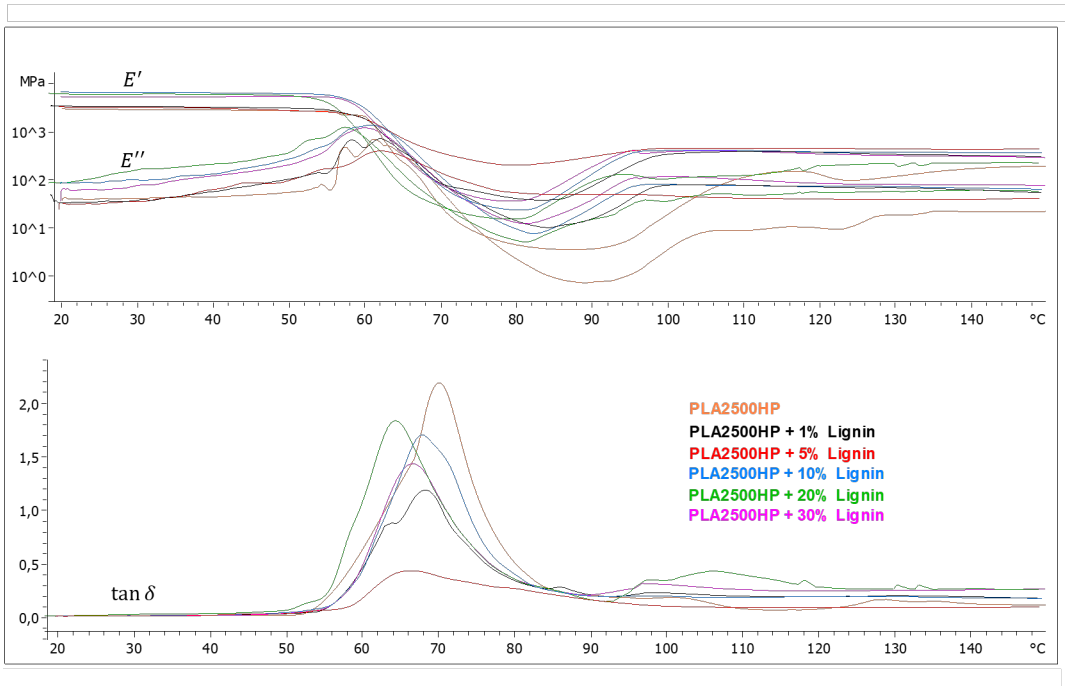

Figure 4.27: DMA curves of PLA 2500HP - Lignin blends.

The evolution of the storage $E^{'}$ modulus, the loss modulus $E^{''}$ and the damping factor $tan\delta$ with the temperature of the different PLA4060D - lignin blends are shown in Figure 4.28. One can observe a decrease of $E^{'}$ around T_g.
For PLA4060D - lignin blends, the value of $E^{'}$ and $E^{''}$ at $25°C$ and the value of T_g taken at the maximum of $tan\delta$ are listed in Table 4.15. The storage modulus $E^{'}$ increase is of 26.7% when 20% of lignin is added. T_g decreases of 1.7% when 20% of lignin is added.

Table 4.15: DMA results for PLA amorphous 4060D - Lignin blends.

PLA 4060D	$E^{'}_{max} \pm 150\,[MPa]$	$E^{''}\,[MPa]$	Maximum of $tan\delta$	$T_g\,[°C]$
AM-N (9)	2960	20	1.65	63.2
AM-1L (10)	3320	23	2.33	64.4
AM-5L (11)	3070	24	2.33	65.4
AM-10L (12)	3480	34	2.07	62.4
AM-20L (13)	3750	45	1.85	62.2

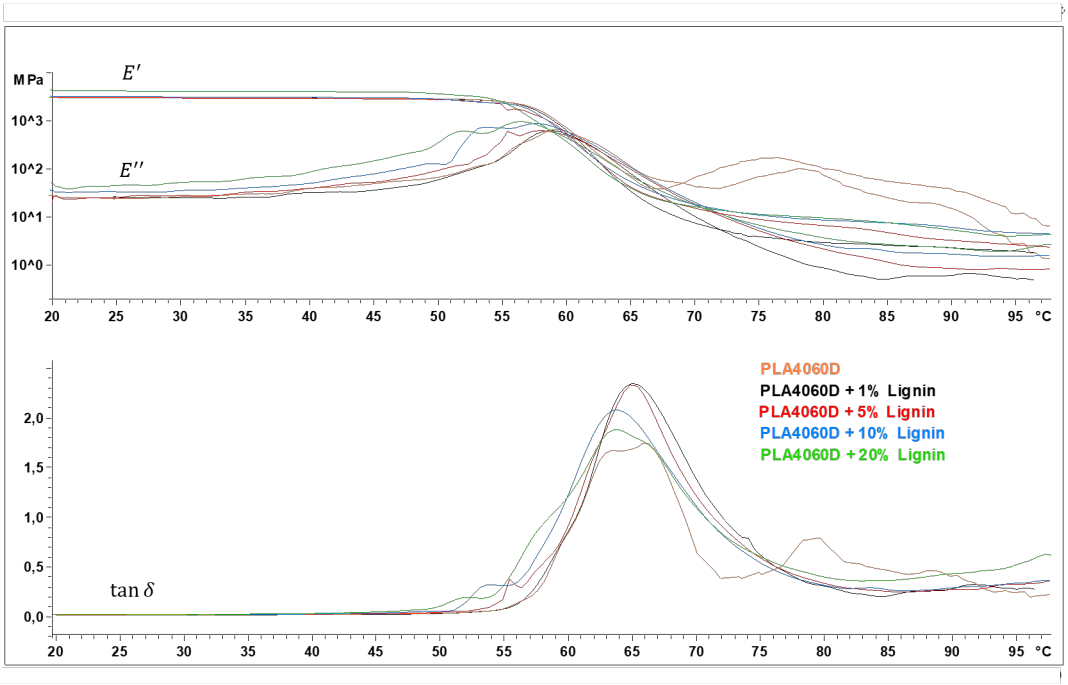

Figure 4.28: DMA results for PLA 4060D - Lignin blends.

4.1.3.0.2 PLA semicrystalline (PLA2500HP) - Flax nanocomposites

For PLA2500HP - flax blends, the value of $E^{'}$ and $E^{''}$ at $25°C$ and the value of T_g taken at the maximum of $tan\delta$ are listed in Table 4.16. The storage modulus $E^{'}$ increase is of 45% when 10% of flax fibers are added and T_g increases of 8.67% when 10% of flax fibers are added. The increase of storage modulus $E^{'}$ is here more important than the one observed for addition of lignin instead of flax.

Table 4.16: DMA results for PLA semicrystalline 2500HP - Flax blends.

	$E^{'}_{max} \pm 150\,[MPa]$	$E^{''}\,[MPa]$	Maximum of $tan\delta$	$T_g\,[°C]$
Neat	2910	293	0.22	75
1% flax	3240	338	0.26	78
5% flax	3320	263	0.19	80
10% flax	4230	283	0.12	81.5

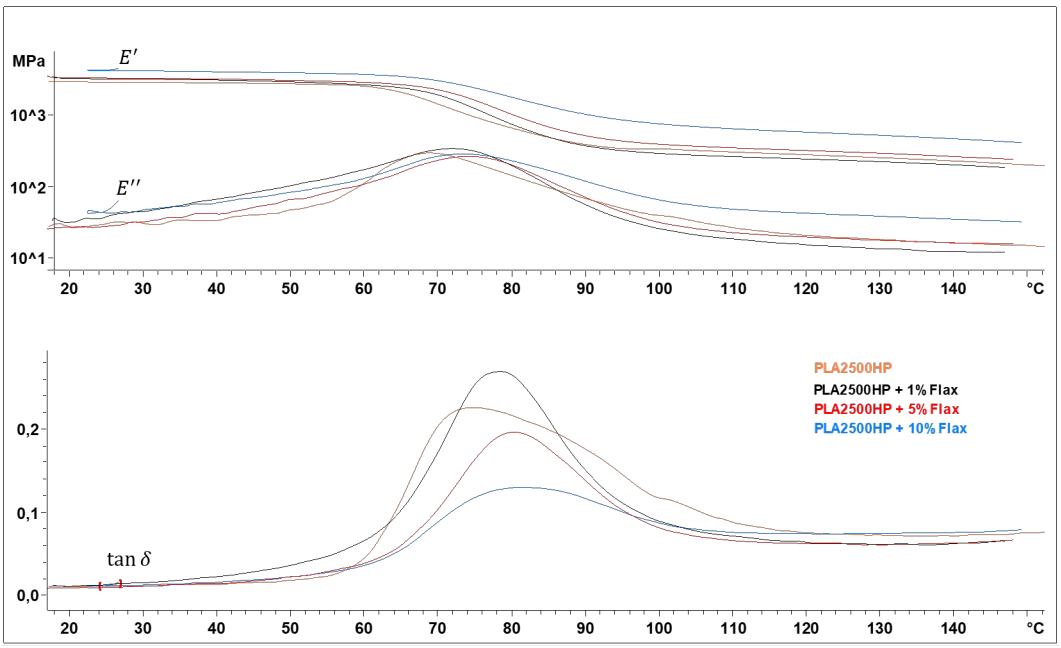

Figure 4.29: DMA results for PLA2500HP - Flax blends.

4.1.3.0.3 PHBV - Flax nanocomposites

For PHBV - flax blends, the value of $E^{'}$ and $E^{''}$ at $25°C$ and the value of T_g taken at the maximum of $tan\delta$ are listed in Table 4.17. The storage modulus $E^{'}$ increase is of 30% when 10% of flax fibers are added which is a smaller increase than for PLA2500HP with both lignin and flax. T_g first increases and then decreases and returns to a value close to the one of neat PHBV when flax fibers is added.

Table 4.17: DMA results for PHBV - Flax blends.

	$E^{'}_{max} \pm 150\,[MPa]$	$E^{''}\,[MPa]$	Maximum of $tan\delta$	$T_g\,[°C]$
Neat	4410	121	0.03	26
1% flax	4880	159	0.04	29
5% flax	5360	197	0.049	28
10% flax	5730	214	0.05	26.5

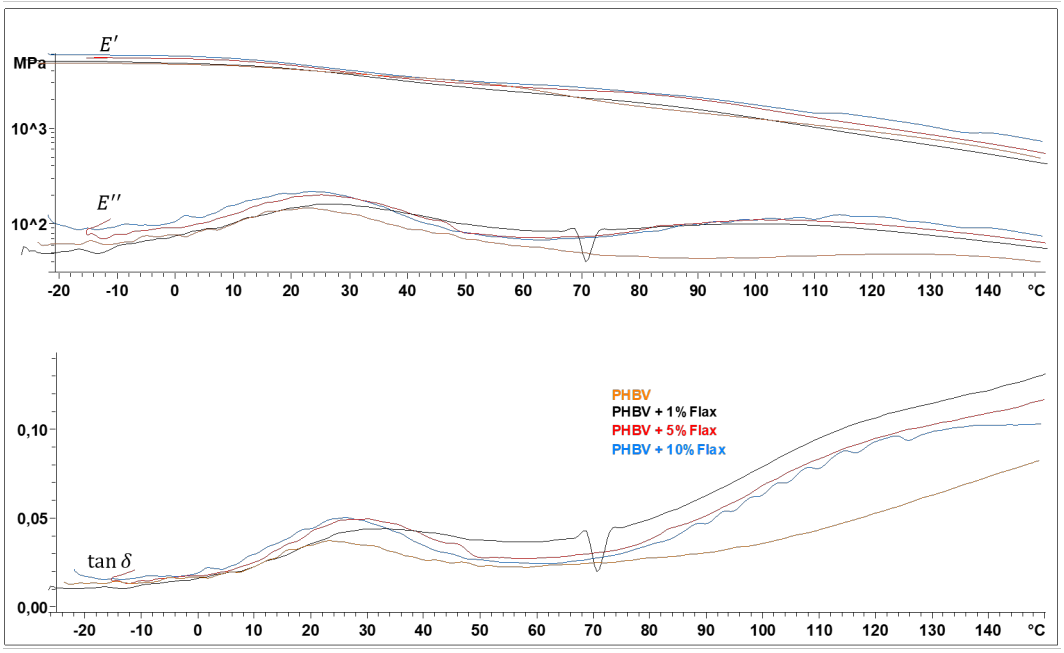

Figure 4.30: DMA results for PHBV - Flax blends.

4.1.3.0.4 Comparison of T_g measured by DSC and DMA

Table 4.18 andTable 4.19 show that the values of T_g obtained from DSC and DMA differ from around 7 to 10°C. However the two analysis indicate that the value of T_g decreases when lignin is added.

There is different possible explanations to this difference in T_g values. First DSC and DMA measure different processes. A difference of 25°C in data from a DSC to DMA data reported as peak of tan delta can be observed. The heating rate used in DMA is typically of 3°C/min because polymers have a small thermal conductivity and the fact that the sample used for DMA is much bigger (higher mass) than the one used for DSC.

Moreover as fillers usually have different conductivity compare to the thermoplastic matrix. As a result a shift in T_g values of the sample can be observe [68, 96, 97]. Therefore the use of low heating rates is important in order for the sample to have enough time to reach thermal equilibrium with the chamber environment.

Moreover interface scattering of phonons during heat transfer in nanocomposites reduces thermal conductivity [96]. The thermocouples in the device are placed on the surface of the specimen and the surface of the specimen does not necessarily reflect the temperature of the bulk.

Additionally the glass transition happens in a range of temperatures. Furthermore the difference measured between $T_{g,dma}$ and $T_{g,dsc}$ is due to the fact that the glass

transition is frequency dependent. In a DSC analysis, the measurement is mainly static even if one attributes a frequency on the order of $10 - 2Hz$ while for the DMA analysis the frequency was set to $1Hz$.
Then the value of $T_{g,DMA}$ will be always higher than the one of $T_{g,DSC}$.

Table 4.18: Comparison of T_g from DSC and DMA analysis for PLA2500HP - Lignin blends.

	$T_g\,[°C]$ from DSC	$T_g\,[°C]$ from DMA
Neat extr.	60.03	69.84
PLA2500HP + 1% Lignin	60.99	68.18
PLA2500HP + 5% Lignin	60.44	66.94
PLA2500HP + 10% Lignin	59.55	67.95
PLA2500HP + 20% Lignin	58.77	66.75
PLA2500HP + 30% Lignin	58.22	66.57

Table 4.19: Comparison of T_g from DSC and DMA analysis for PLA4060D - Lignin blends.

	$T_g\,[°C]$ from DSC	$T_g\,[°C]$ from DMA
Neat extr.	56.35	63.2
PLA4060D + 1% Lignin	55.91	64.35
PLA4060D + 5% Lignin	55.79	65.42
PLA4060D + 10% Lignin	55.13	62.41
PLA4060D + 20% Lignin	54.35	62.15

4.1.3.0.5 Comparison of E measured by tensile test and DMA

Table 4.20 andTable 4.21 show that the values of E_t and $E^{'}$ obtained from tensile test and DMA differ from around 0.06 to $1.32GPa$. However the two analysis indicate that the value of E_t and $E^{'}$ increases when lignin is added as expected. Young's modulus E_t calculated from the slope of the initial part of a stress-strain curve and the storage modulus $E^{'}$ are close conceptually. However they are not the same even if $E^{'}$ is a measure of the elastic response of a material [68].
Moreover E_t form tensile test is calculated in fairly small deformations in the elastic region assuming that the material deforms only elastically. Young's modulus depends both on engineering strain rate $\dot{\varepsilon}$ and temperature T : $E(\dot{\varepsilon}, T)$. Tensile test is performed at $23.3°C$ and the loading speed is of $5\,[mm/min]$ which corresponds to $\dot{\varepsilon} = 0.003\,[s^{-1}]$. In DMA the frequency is fixed at $1Hz$ while a sweep in temperature form $20°C$ to $100°C$ for PLA4060D or $150°C$ for PLA2500HP is realised. DMA is based on the principle that the material's deformation is the combination of the elastic and viscous behavior. If the material tested is isotropic or if the DMA test is done in the same direction as the tensile test and is done in the linear viscoelastic region, then the value of $E^{'}$ should be in good agreement with the value of E_t obtained from the tensile test [68, 98].

Table 4.20: Comparison of E from tensile test and DMA analysis for PLA2500HP - Lignin blends.

	$E_t\,[GPa]$ from tensile test	$E^{'} \pm 0.15\,[GPa]$ from DMA
Neat extr.	3.72	3.0
PLA2500HP + 1% Lignin	3.72	3.33
PLA2500HP + 5% Lignin	3.82	3.65
PLA2500HP + 10% Lignin	3.91	4.16
PLA2500HP + 20% Lignin	3.93	5.12
PLA2500HP + 30% Lignin	4.2	5.3

Table 4.21: Comparison of E from tensile test and DMA analysis for PLA4060D - Lignin blends.

	$E_t\,[GPa]$ from tensile test	$E^{'} \pm 0.15\,[GPa]$ from DMA
Neat extr.	3.6	2.95
PLA4060D + 1% Lignin	3.63	3.32
PLA4060D + 5% Lignin	3.58	3.07
PLA4060D + 10% Lignin	3.76	3.48
PLA4060D + 20% Lignin	3.85	3.75

The slight increase of E_t with lignin addition is surprising. The calculated values of E_t are compared to the Voigt and Reuss bounds (see Table 4.22 and Table 4.23). Voigt and Reuss models correspond to the simple case of laminated composite structure. The upper bound E_{upper} follows a rule of mixture. It is found by assuming that the two components undergo the same strain during loading. Hence the stress is the volume average of the local stresses. The lower bound E_{lower} is obtained by assuming that the two components bear the same stress. The strain is then the volume average of the local strains [99].
The tables reveal that the calculated stiffness is lower than the Reuss bound. The concentration of lignin in the specimen (obtained from injection moulding) is probably lower that the one in the premix due to loss of lignin powder on surfaces during processing steps. Dispersion of lignin particles in the blend is also investigated in 4.1.4.

$$E_{upper} = fE_{Lignin} + (1-f)E_{PLA} \tag{4.1}$$

$$E_{lower} = \frac{E_{Lignin}E_{PLA}}{fE_{PLA} + (1-f)E_{Lignin}} \tag{4.2}$$

with f the volume fraction of lignin in the blends.

Table 4.22: Comparison of E_t with Voigt and Reuss models for PLA2500HP - Lignin blends.

	E_t	E_{upper}	E_{lower}
PLA2500HP + 1% Lignin	3.72	3.78	3.74
PLA2500HP + 5% Lignin	3.82	3.99	3.84
PLA2500HP + 10% Lignin	3.91	4.25	3.96
PLA2500HP + 20% Lignin	3.93	4.71	4.2
PLA2500HP + 30% Lignin	4.2	5.11	4.43

Table 4.23: Comparison of E_t with Voigt and Reuss models for PLA4060D - Lignin blends.

	E_t	E_{upper}	E_{lower}
PLA4060D + 1% Lignin	3.63	3.66	3.62
PLA4060D + 5% Lignin	3.58	3.88	3.72
PLA4060D + 10% Lignin	3.76	4.15	3.85
PLA4060D + 20% Lignin	3.85	4.6	4.09

4.1.4 Dispersion analysis

The aim of the observation of the samples with a secondary electron microscope (SEM) is on one hand to see the quality of dispersion of the charge in the TP matrix and on the other hand to see if the charges are individual ones or agglomerated (interspersed or exfoliated morphological state). If well dispersed agglomerates exist, it will impact the mechanical properties. Indeed, lignin particles agglomerates could not be able to be deformed.

Thanks to the observation of the semi-crystalline PLA (PLA2500HP) with 5% of lignin blend with SEM, one can observe spherulites in Figure 4.32. As explained in chapter 2, solidification starts with nucleation. During nucleation a small number of atoms or molecules aggregates due to temperature fluctuations in the melt. Therefore, this process is generally described as a random process in space but the random description only holds when the heat flow rate does not depend on the direction, that is to say when the heat propagation is isotropic. In those conditions, observations of polymer crystallisation from melt show the growth of circular crystalline units known as spherulite. The spherulites are usually made up of fibrillar crystals that originated in the centre (Figure 4.31) [100, 101].

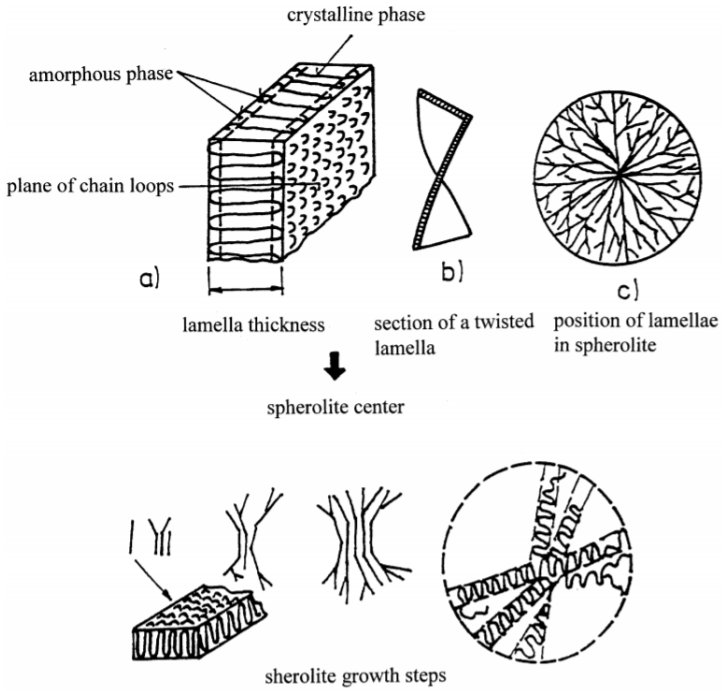

Figure 4.31: Drawing of a 2D projection of a spherulite formed from radially grown lamellae with a small degree of branching [26].

As there is no metallic coating on the sample, it was not possible to zoom on spherulites. Charge phenomenon appears due to the accumulation of electrons on the surface which would lead to over-brightness and deflection of the beam.
Thanks to the software *ImageJ*, the average dimensions of spherulites are measured. As the observed spherulites are seen as ellipses, two dimensions (diameter) are averaged: $6.45\mu m$ and $4.65\mu m$.

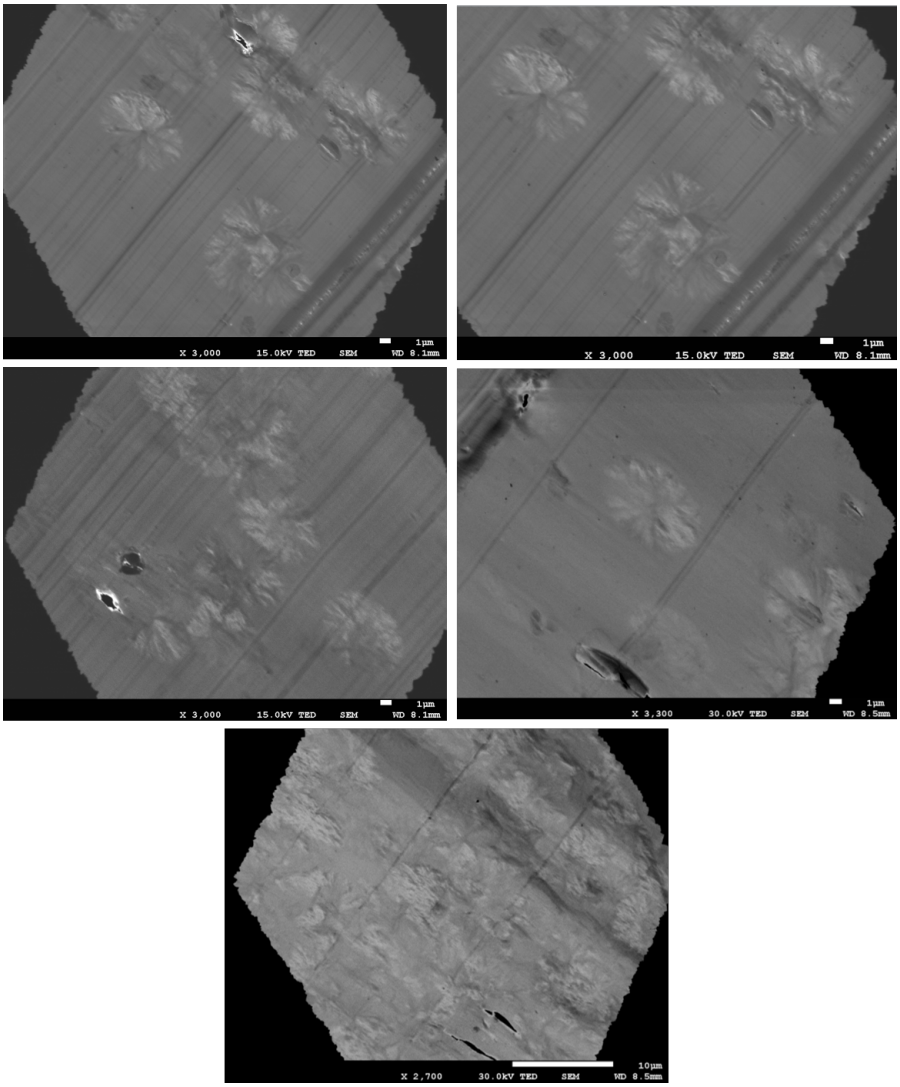

Figure 4.32: SEM pictures of semicrystalline PLA 2500HP with 5% of lignin.

For the amorphous PLA (PLA4060D) with 5% lignin, the SEM pictures (see Figure 4.33) reveal agglomerates of different sizes (measured with *ImageJ*. Smaller ones are quite spherical with average dimensions between 0.3 and 0.9μm. Medium ones have average dimensions between 1.2 and 2.8μm. Bigger ones are ellipses with average dimensions between 3.5 and 7.6μm. Those agglomerates could be lignin particles and can be at the origin of the reduction of mechanical properties when lignin is added to PLA.

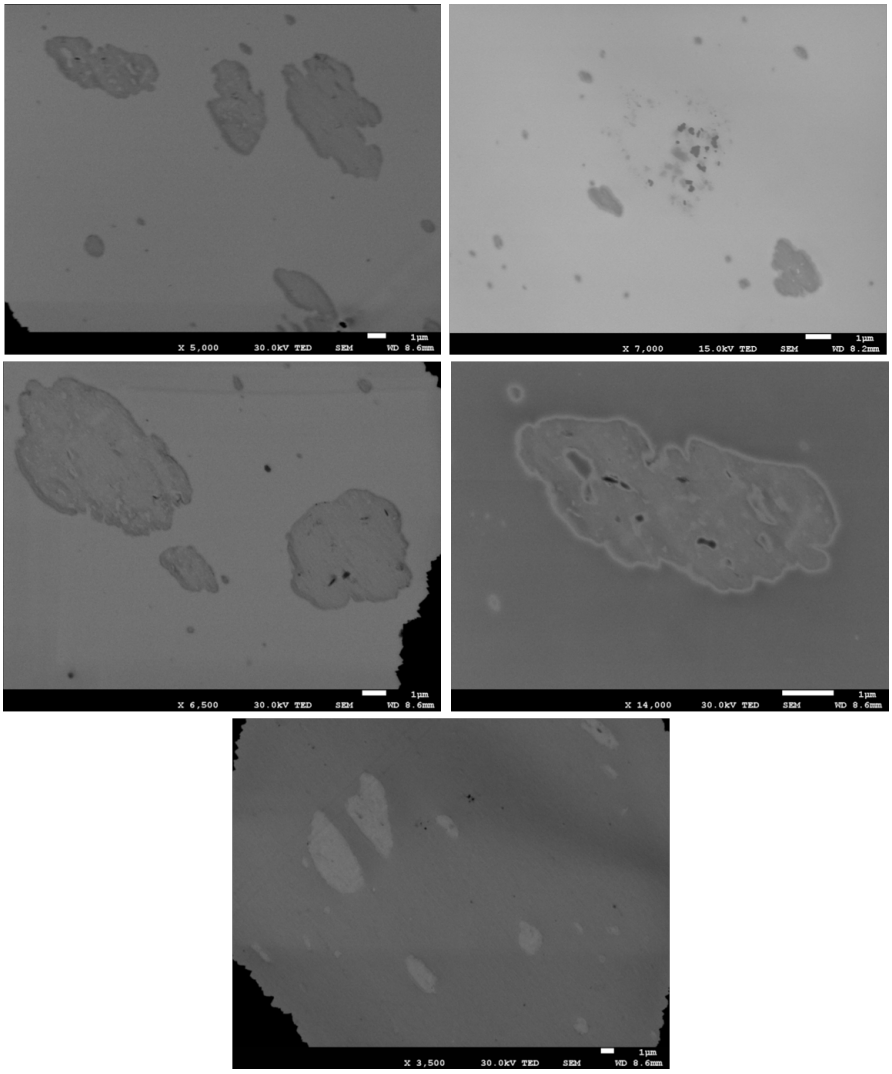

Figure 4.33: SEM pictures of amorphous PLA 4060D with 5% of lignin.

In order to have a more comprehensive understanding of the presence or not about lignin particles agglomerates in PLA4060D - lignin blends, STEM (scanning transmission electron microscope) or TEM (transmission electron microscope) images could be useful.

Chapter 5

Conclusion and Perspectives

To conclude, this work explores specific properties of nanocomposites made of lignin particles dispersed in a semi-crystalline or amorphous polylactic acid (PLA) matrix. Morphological, thermal and mechanical properties are investigated thanks to a number of analysis and tests including scanning electron microscopy (SEM), differential scanning calorimetry (DSC), thermogravimetry analysis (TGA), dynamical mechanical analysis (DMA) and tensile test.

Thermal characterisation indicates that lignin addition slightly decreases the thermal stability of PLA. Though the thermal stability of semi-crystalline and of amorphous PLA are similar. DSC results exhibit that the glass transition temperature T_g for both PLA and the melting temperature T_m for the PLA2500HP decrease when lignin is added, although this decrease is small.
Regarding the mechanical and thermo-mechanical properties, tensile test shows an increase in stiffness E_t (increase of 3.38% for PLA2500HP and 0.79% for PLA4060D for $20wt\%$ of lignin added) when the content of lignin in the blend increases however at the same time the maximum tensile strength σ_{max} and the strain at break ε_b decrease significantly. The decrease of ε_b is even more important for the amorphous PLA (decrease of 76.99% for $20wt\%$ of lignin added) which is initially the most ductile one while the decrease of σ_{max} is larger for the semi-crystalline PLA (decrease of 20.44% for $20wt\%$ of lignin added). Above $20wt\%$ of lignin, the decrease of those mechanical properties becomes detrimental compare to the profit of the stiffness' increase.
DMA analysis reveals a significant increase of the storage modulus $E^{'}$ with the addition of lignin for both semi-crystalline and amorphous PLA (increase of 70% and 26.7% for 20% of lignin added respectively). As expected from DSC results, glass transition temperature T_g decrease slightly with lignin addition. However this decrease is not so significant to be detrimental (decrease of 4.4% for PLA2500HP and 1.7% for PLA4060D for $20wt\%$ of lignin added).

SEM pictures allow to observe the spherulites present in the semi-crystalline PLA. Potential lignin agglomerates of different sizes are also observed in amorphous PLA with 5% of lignin thanks to SEM indicating that manual mixing and extrusion do not allow to blend at molecular level the two components. Those agglomerates could explain the decrease of the values of σ_{max} and ε_b.

Spider charts summarizing the influence of the addition of different weight percentage of lignin on the key thermal and mechanical properties of all nanocomposites are presented in Figure 5.1 and Figure 5.2.

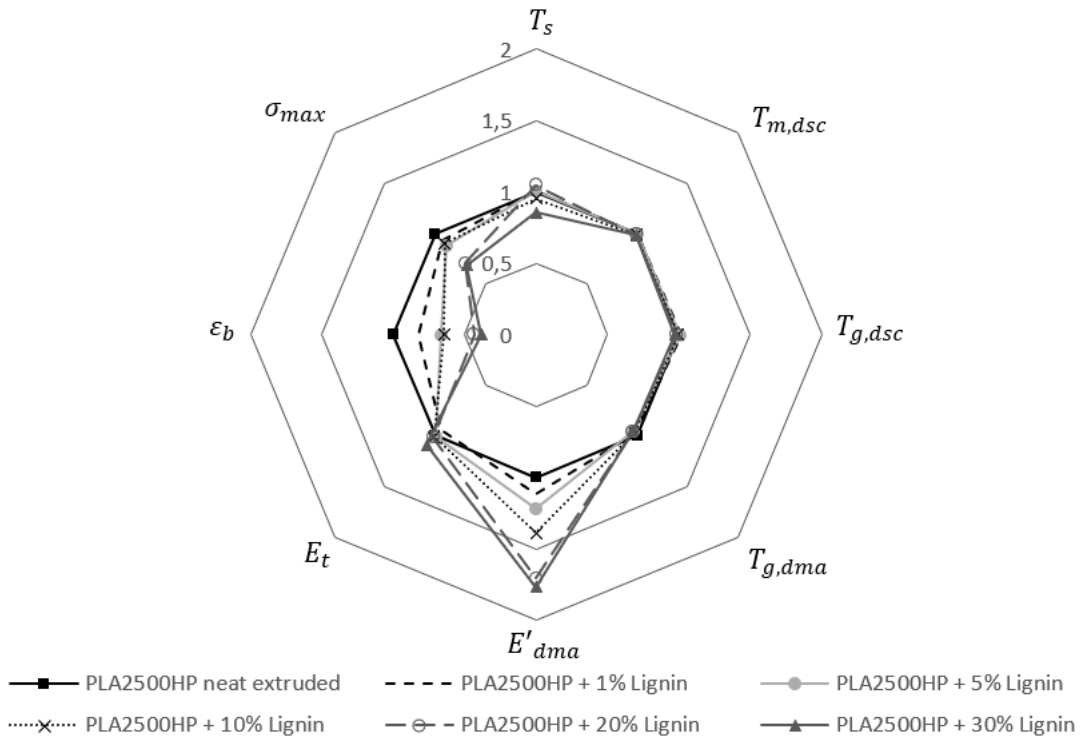

Figure 5.1: Comparative plot of the main properties of the modified semi-crystalline PLA relative to the values for the reference material.

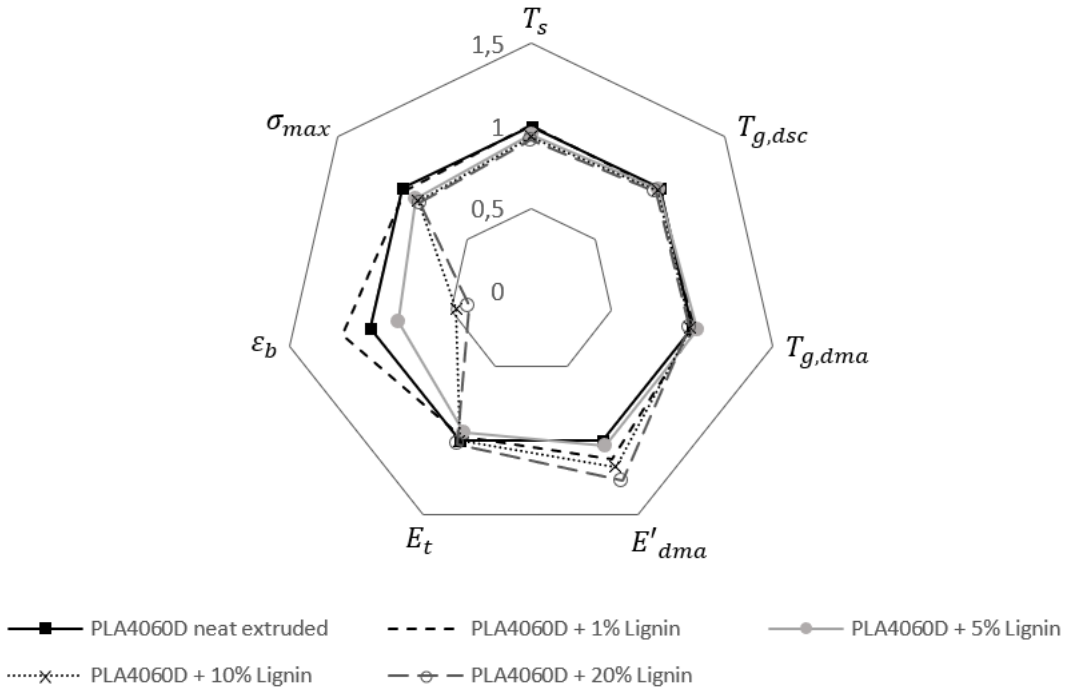

Figure 5.2: Comparative plot of the main properties of the modified amorphous PLA relative to the values for the reference material.

Perspectives

To go further in this research, SEM analysis should be performed for all types of nanocomposites: on neat PLA's (semi-crystalline and amorphous) and PLA's with all percentages of lignin. A metallic coating should be deposited on the surface of the sample to avoid damages and prevent charge effects because the material is not conductive. The metallic coating should allow to zoom on spherulites formed in the semi-crystalline PLA. The SEM observation of the different PLA2500HP (semi-crystalline) - Lignin blends could allow to see if lignin particles really act as nucleating agents and thus if the number and size of spherulites increases with the percentage of lignin.
Compression tests could help to characterise more clearly the mechanical behavior of PLA - Lignin blends. Fracture surfaces analysis on the specimens used for tensile test could indicate interface mechanisms and reveal lignin particle's voids.

Perhaps the most important improvement step concerns the processing steps and the homogeneity of the samples. Indeed manual mixing of pellets and nano-sized powder is not optimal: powder-powder mixing or use of solvent should be considered.

Then, the second part of the work is to characterise the epoxy resin - nanocomposite blends already prepared. The methodology proposed for the realisation of the blend should be followed when the nanocomposite is made with PLA to obtain a good solubilisation of the thermoplastic nanocomposites pellets in the resin. Different mechanical tests can be performed to characterise the composite made of the thermoplastic nanocomposite and the epoxy resin to identify the enhancements obtained by adding the nanocomposite to the bio-sourced epoxy resin. As one of the main property of interest is the toughness of the composite, SENB tests should be achieved. Hardness tests and DMA analysis could also be attractive to examine hardness improvement and evolution of $E^{'}$ and $E^{''}$ with temperature. A compression test could also be performed to determine the behavior of the modified resin under a compressive load.
Fracture surfaces analysis should provide information about resulting morphology of the three-phase system and toughening mechanisms.

Percentage of lignin charges in the TP matrix and percentage of nanocomposite in the bio-sourced epoxy resin should be optimised.

To have a better idea of the profit/advantages of this modification, the results should be compare to other modifications: addition of the same or another nanocomposite made of another thermoplastic and with another charge in the epoxy resin.

The final aim of the work would be to make and characterise a real plate of composite. The plate will be formed using the RTM process which allows to make a composite plate with the epoxy resin - nanocomposite blend and long woven fibers (for example flax fibers).

Chapter 6

Appendix 1: Additional graphs

To complete the results and discussion part of this work (Chapter 4), this appendix presents graphs showing the evolution of a property measured thanks to one of the analysis in function of the lignin content (wt%).

DSC graphs

Figure 6.1(a), Figure 6.1(b), Figure 6.1(c) and Figure 6.2 present the evolution of the melting temperature T_g, degree of crystallinity χ_c and the glass transition temperature T_g of semi-crystalline PLA and T_g of amorphous PLA with the addition of lignin.
The percentage above the bars of those graphs are calculated compared to either the PLA neat and not extruded (Neat).

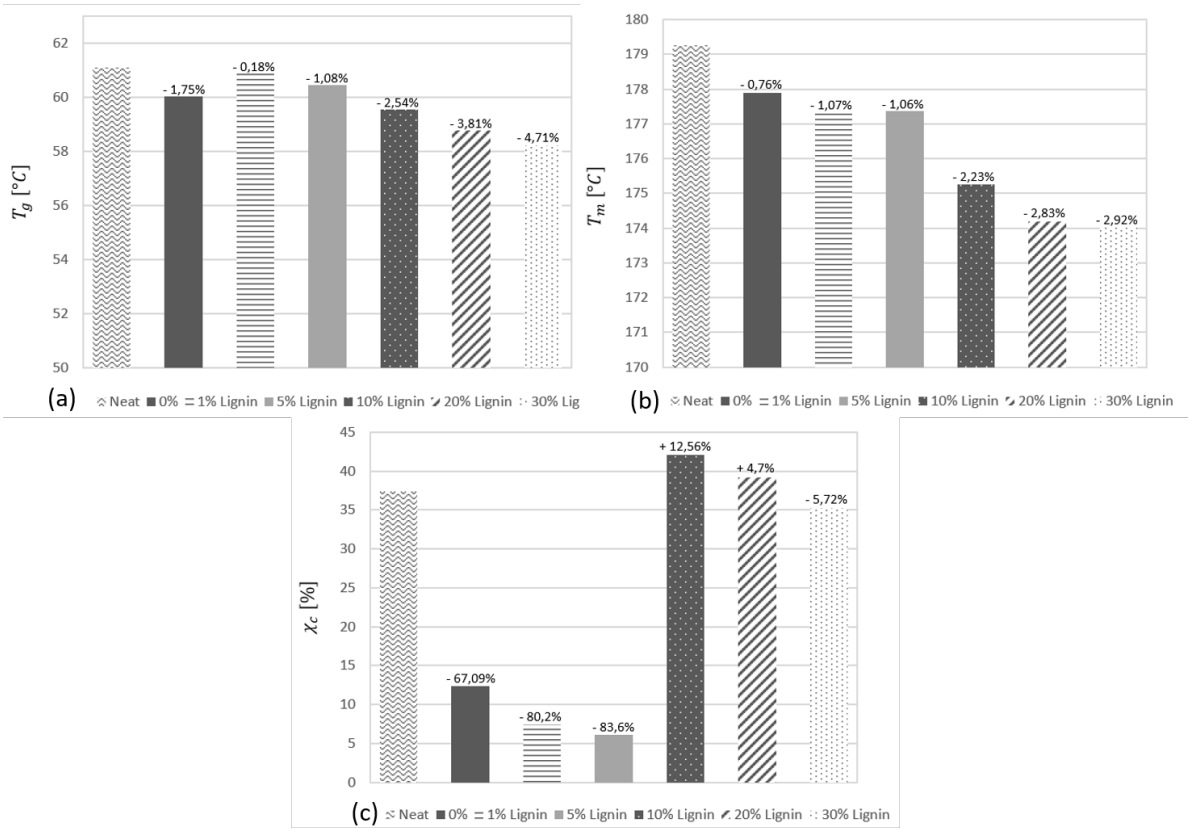

Figure 6.1: Evolution of (a) the glass transition temperature T_g, (b) the melting temperature T_m and (c) the degree of crystallinity χ_c of modified PLA2500HP with addition of lignin.

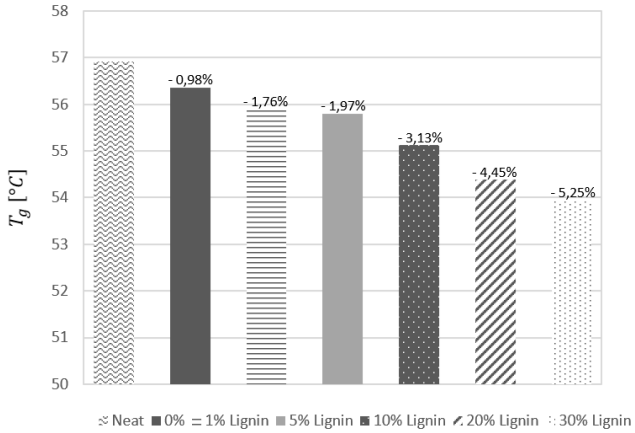

Figure 6.2: Evolution of glass transition temperature T_g of modified PLA4060D with addition of lignin.

TGA graphs

Figure 6.3(a) and Figure 6.3(b) present the evolution of the starting point of thermal degradation T_s of the semi-crystalline PLA and the amorphous PLA with the addition of lignin.
The percentage above the bars of those graphs are calculated compared to either the PLA neat and extruded (0% Lignin).

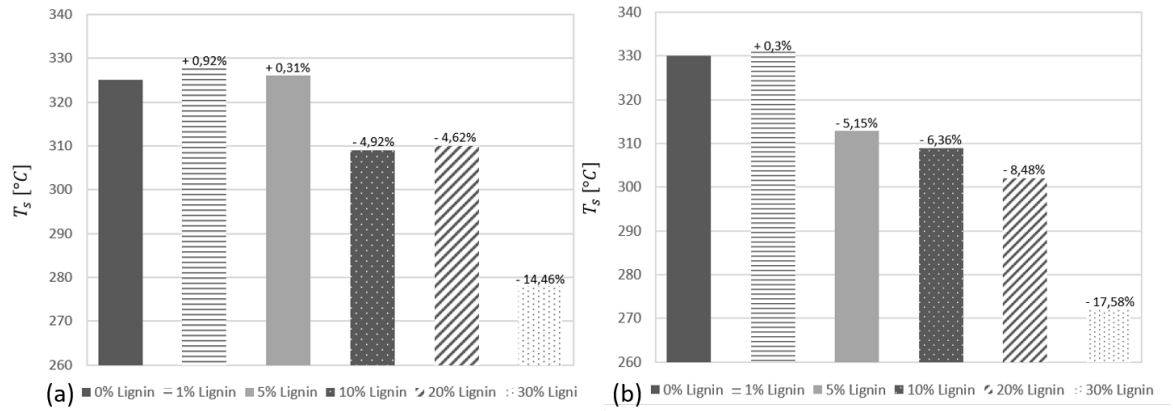

Figure 6.3: Evolution of he starting point of thermal degradation T_s of (a) modified PLA2500HP and (b) modified PLA4060D the melting temperature T_m with addition of lignin.

DMA graphs

Figure 6.4(a), Figure 6.4(b), Figure 6.4(c) and Figure 6.4(d) present the evolution of the storage modulus $E^{'}$, the loss modulus $E^{''}$, the damping factor $tan\delta$ and the glass transition temperature T_g of semi-crystalline PLA with the addition of lignin measured by DMA. Figure 6.5(a), Figure 6.5(b), Figure 6.5(c) and Figure 6.5(d) present the evolution of the storage modulus $E^{'}$, the loss modulus $E^{''}$, the damping factor $tan\delta$ and the glass transition temperature T_g of semi-crystalline PLA with the addition of lignin measured by DMA.
The percentage above the bars of those graphs are calculated compared to either the PLA neat and extruded (0% Lignin).

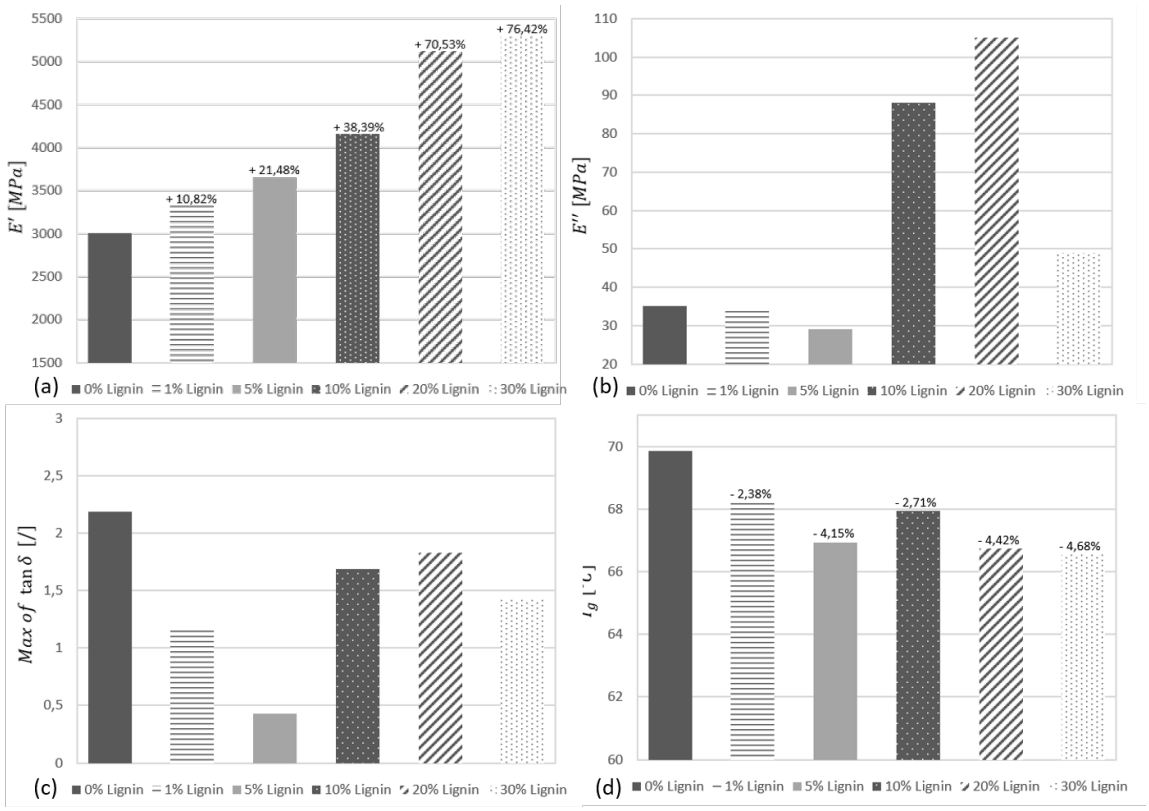

Figure 6.4: Evolution of (a) the storage modulus $E^{'}$, (b) the loss modulus $E^{''}$, (c) $tan\delta$ and (d) the glass transition temperature T_g of modified PLA2500HP with addition of lignin.

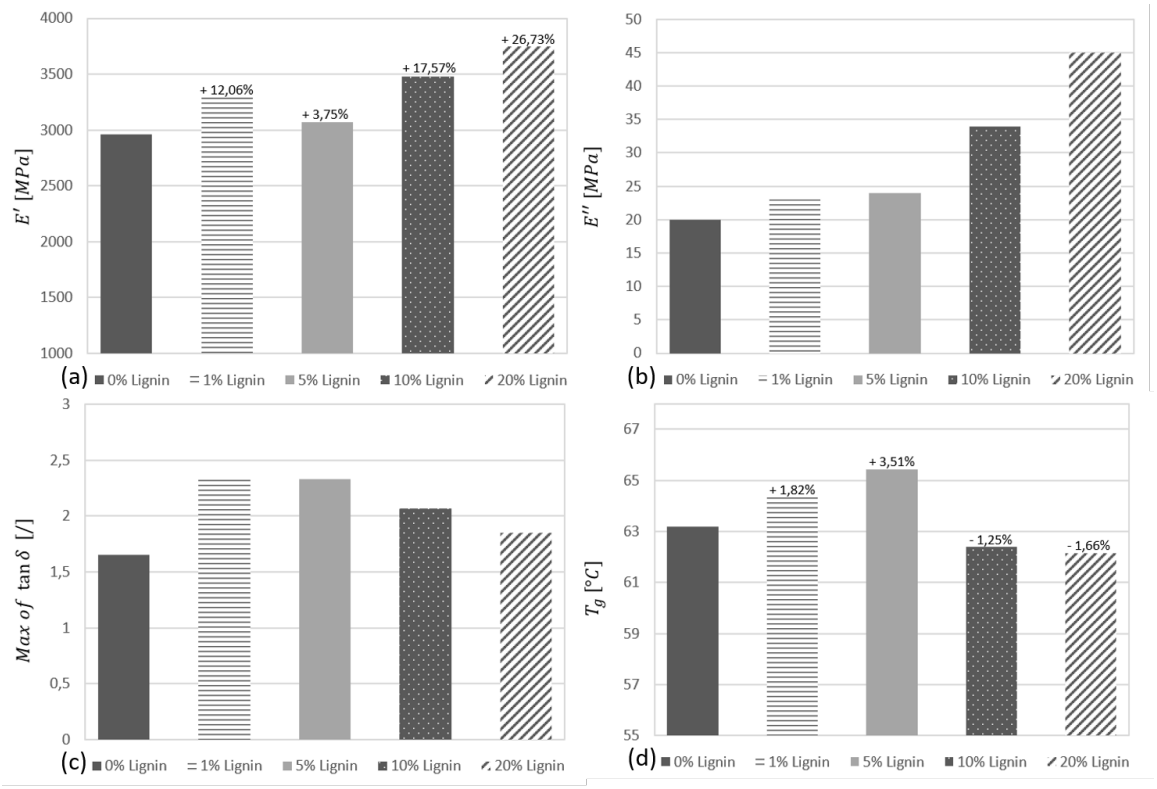

Figure 6.5: Evolution of (a) the storage modulus $E^{'}$, (b) the loss modulus $E^{''}$, (c) $tan\delta$ and (d) the glass transition temperature T_g of modified PLA4060D with addition of lignin.

Tensile test graphs

Stress-strain curves for each PLA/Lignin blends used for tensile test drawn using Matlab are displayed in Figure 6.6, Figure 6.7, Figure 6.8, Figure 6.9, Figure 6.10, Figure 6.11, Figure 6.12, Figure 6.13, Figure 6.14, Figure 6.15 and Figure 6.16. The curves are drawn after averaging the data on at least 3 tests for the same blend because the injection moulding cylinder contains enough material to make several samples. The last sample made with a single charge of material inside the cylinder therefore spent more time in the heating cylinder than the first one. The properties of the different specimens from the same blend can thus be different.

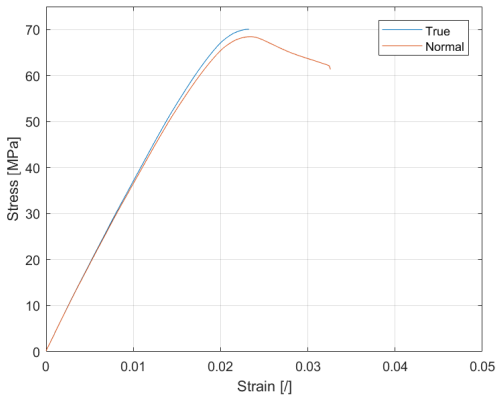

Figure 6.6: Stress-strain curves for PLA2500HP neat extruded.

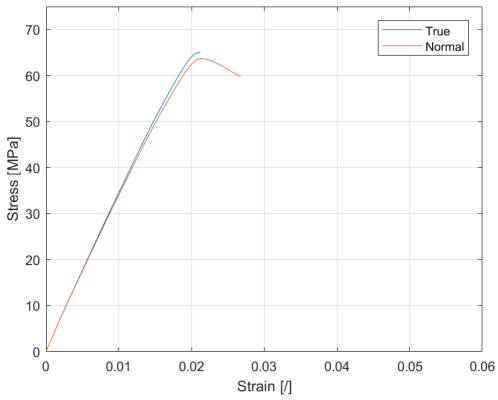

Figure 6.7: Stress-strain curves for PLA2500HP - 1wt%Lignin blend.

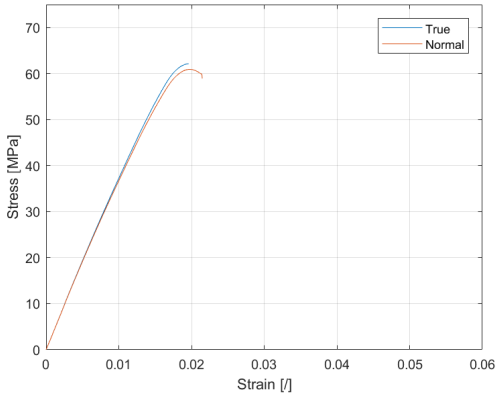

Figure 6.8: Stress-strain curves for PLA2500HP - 5wt%Lignin blend.

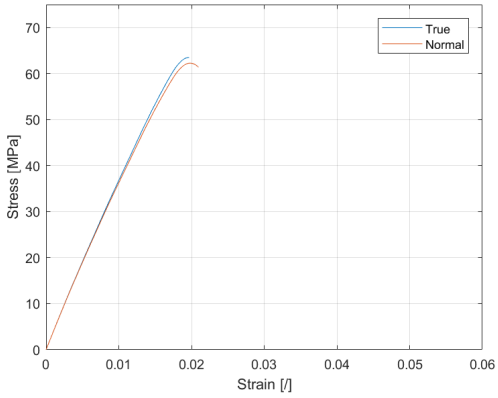

Figure 6.9: Stress-strain curves for PLA2500HP - 10wt%Lignin blend.

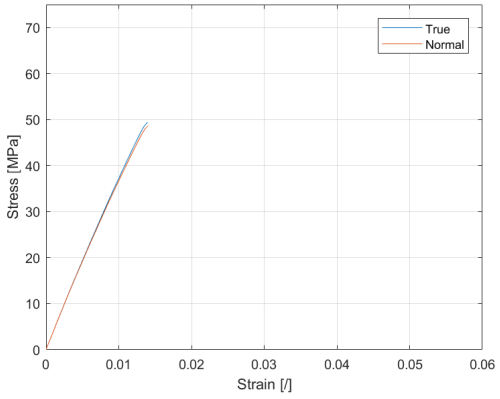

Figure 6.10: Stress-strain curves for PLA2500HP - 20wt%Lignin blend.

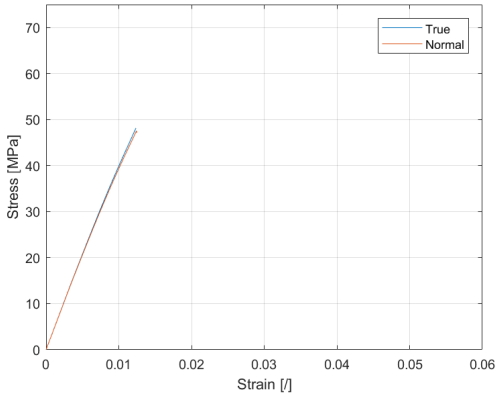

Figure 6.11: Stress-strain curves for PLA2500HP - 30wt%Lignin blend.

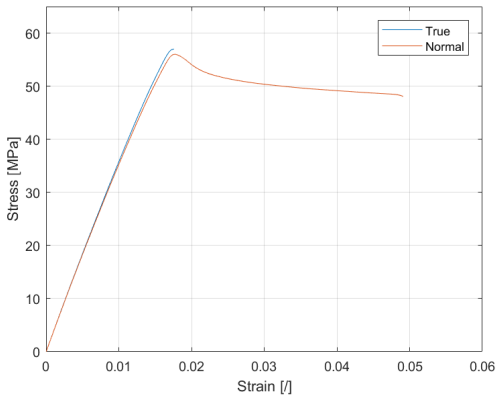

Figure 6.12: Stress-strain curves for PLA4060D neat extruded.

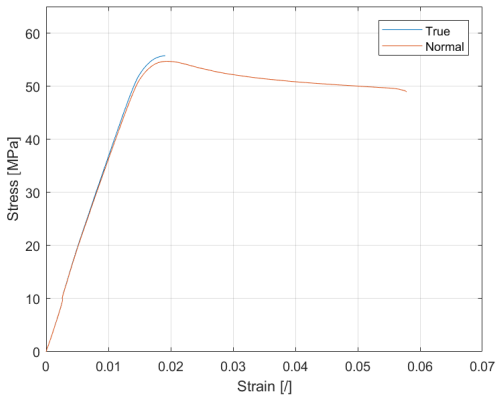

Figure 6.13: Stress-strain curves for PLA4060D - 1wt%Lignin blend.

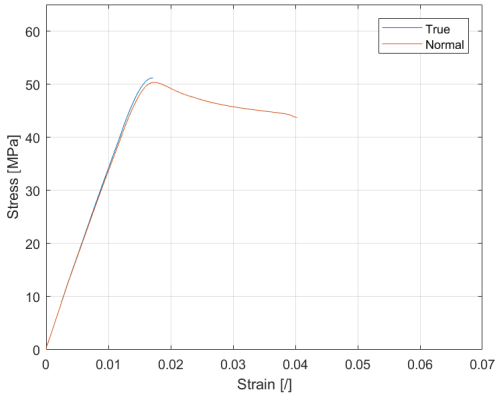

Figure 6.14: Stress-strain curves for PLA4060D - 5wt%Lignin blend.

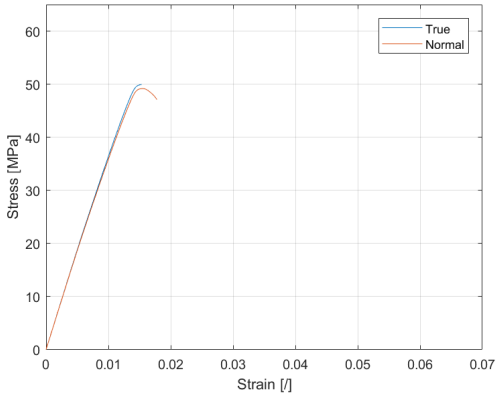

Figure 6.15: Stress-strain curves for PLA4060D - 10wt%Lignin blend.

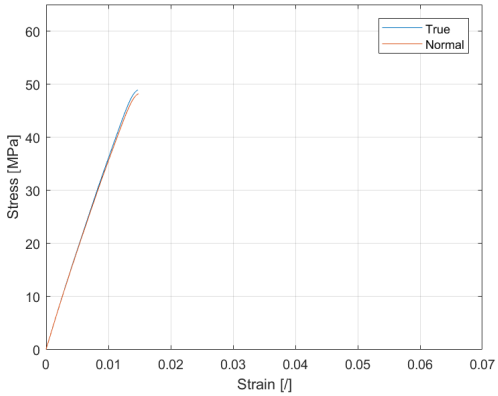

Figure 6.16: Stress-strain curves for PLA4060D - 20Lwt%Lignin blend.

Bibliography

[1] Sylvain Caillol, Bernard Boutevin, and Jean-Pierre Pascault. Biosourced epoxy resins. pages 441–468, 2017.

[2] Maria Laura Di Lorenzo. Calorimetric Analysis of the Multiple Melting Behavior of Poly(L-lactic acid). *Journal of Applied Polymer Science*, 100:3145–3151, 2005.

[3] L.-T. Lim, Auras R., and Rubino M. Processing technologies for poly(lactic acid). *Progress in Polymer Science (Oxford)*, (33):820–852, 2008.

[4] Shady Farah, Daniel G. Anderson, and Robert Langer. Physical and mechanical properties of PLA, and their functions in widespread applications — A comprehensive review. *Advanced Drug Delivery Reviews*, 107:367–392, 2016.

[5] R.A. Venditti R.D. Gilbert A.L. Compere c W. Griffith J.F. Kadla, S. Kubo. Lignin-based carbon fibers for composite fiber applications. *Carbon*, 40:2913–2920, 2002.

[6] B. S. Panigrahy, A. Rana, P. Chang, and S. Panigrahi. Overview of Flax Fiber Reinforced Thermoplastic composites. *The Canadian Society for Bioengineering (CSBE)*, 2006.

[7] Jiang Li and Chin Seng Chua. Thermal and mechanical properties of biodegradable blends of poly(l-lactid acid) and lignin. *Polymer International*, 52:949–955, 2003.

[8] NatureWorks. Ingeo$_{\text{TM}}$ biopolymer 2500hp technical data sheet. `https://www.natureworksllc.com/~/media/Files/NatureWorks/Technical-Documents/Technical-Data-Sheets/TechnicalDataSheet_2500HP_extrusion_pdf.pdf`. Accessed on 17/10/2019.

[9] NatureWorks. Ingeo$_{\text{TM}}$ biopolymer 4060d technical data sheet. `https://www.natureworksllc.com/~/media/Files/NatureWorks/Technical-Documents/Technical-Data-Sheets/TechnicalDataSheet_4060D_films_pdf.pdf`. Accessed on 23/10/2019.

[10] Sicomin. Sr infugreen 810 / sd 882x sd 477x - technical datasheet. `http://www.sicomin.com/datasheets/product-pdf1167.pdf`, 2017. Accessed on 27/01/2020.

[11] Matthieu Aressy. *Etude et modélisation de la cristallisation du Polylactide (PLA) en vue de l'optimisation du procédé de rotomoulage*. PhD thesis, Ecole Nationale Supérieure d'Arts et Métiers, 2013.

[12] Michael Ashby. *Materials and Sustainable Development - Chapter 8: Scaling Up Biopolymer Production*. Elsevier, 2016.

[13] Stefania Bertella and Jeremy S. Luterbacher. Lignin functionalization for the production of novel materials. 2020.

[14] Chao Wang, Stephen S. Kelley, and Richard A. Venditti. Lignin-based thermoplastic materials. *ChemSusChem*, 9:770–783, 2016.

[15] Lei Hu. *Utilisation des lignines industrielles comme renfort dans les composites à base de polyéthylène*. PhD thesis, Université de Laval, Québec, Canada, 2014.

[16] Haiping Yang, Rong Yan, Hanping Chen, Dong Ho Lee, and Chuguang Zheng. Characteristics of hemicellulose, cellulose and lignin pyrolysis. *Fuel*, 86:1781–1788, 2007.

[17] Ali Amiri, Chad A. Ulven, and Shanshan Huo. Effect of chemical treatment of flax fiber and resin manipulation on service life of their Composites using time-temperature superposition. *Polymers*, 7:1965–1978, 2015.

[18] Fan-Long Jin, Xiang Li, and Soo-Jin Park. Synthesis and application of epoxy resins: A review. *Journal of Industrial and Engineering Chemistry*, 29:1–11, 2015.

[19] C. Barrère and F. Dal Maso. Résines époxy réticulées par des polyamines : Structure et propriétés. *Revue de l'Institut Francais du Petrole*, 52(3):317–335, 1997.

[20] Epoxidation of vegetable oils: a review. *Int. J. Adv. Eng. Technol*, 2(Iv):491–501, 2011.

[21] Elyse A Baroncini, Santosh Kumar Yadav, Giuseppe R Palmese, and Joseph F Stanzione. Recent advances in bio-based epoxy resins and bio-based epoxy curing agents. *Journal of Applied Polymer Science*, 2016.

[22] Christian Bailly. Morphology and properties of multiphasic polymer systems., 2019.

[23] O. Saray, S.K. Bhullar, and A.O. Güney. Tensile testing: Experiment sheet, 2015. Bursa Technical University, Faculty of Natural Sciences, Architecture and Engineering, Department of Mechanical Engineering, Mechanical Engineering Laboratory.

[24] Polymer Properties Database. Stress-strain behvior of polymers, 2015.

[25] Morio Kojima. Stress whitening in crystalline propylene-ethylene block copolymers. *Journal of Macromolecular Science, Part B: Physics*, 19:523–541, 1981.

[26] Josef Jancar. Structure-property relationships in thermoplastic matrices. *Advances in Polymer Science*, 139, 1999.

[27] Thomas Pardoen. Lmapr2481: Deformation and fracture of materials, 2018.

[28] American Society for Testing and Materials. Standard test methods for plane-strain fracture toughness and strain energy release rate of plastic materials : D5045-14, 1999.

[29] J. Li, Y. He, and Y. Inoue. Study on thermal and mechanical properties of biodegradable blends of poly(-caprolactone) and lignin. *Polymer Journal*, 33:336–343, 2001.

[30] Raymond A. Pearson and Albert F. Yee. Toughening mechanisms in thermoplastic-modified epoxies: 1. modification using poly(phenylene oxide). *Polymers*, 34:3658–3670, 1993.

[31] Zotti Aldobenedetto, Zuppolini Simona, Zarrelli Mauro, and Borriello Anna. *Adhesives - Applications and Properties extensively, Chapter 10: Fracture Toughening Mechanisms in Epoxy Adhesives*. 2016.

[32] A. F. YEE B. J. CARDWELL. Toughening of epoxies through thermoplastic crack bridging. *Journal of Materials Science*, 33:5473 – 5484, 1998.

[33] P. Van Velthem W. Ballout, J. Horion. Toughening of epoxy resins. influence of toughening agents on resulting morphologies and mechanical properties.

[34] Ana M. Díez-Pascual. Mechanical properties of epoxy/thermoplastic blends. *Handbook of Epoxy Blends*, pages 743 – 774, 2017.

[35] Anne-Christine Baudouin Florian J. Stadler Christian Bailly Fangfang Tao, Dietmar Auhl. Influence of multiwall carbon nanotubes trapped at the interface of an immiscible polymer blend on interfacial tension. *Macromolecular Chemistry and Physics*, 214:350–360, 2013.

[36] Sarah Gabriel. Effet de synergie entre du phénoxy et des csrs sur la ténacité d'une résine époxy hautement réticulée. 2017.

[37] Melter Toledo. Differential scanning calorimetry - poster, 2015.

[38] Melter Toledo. Thermogravimetry - poster, 2015.

[39] James H. Wittke. 2.1. effects of electron bombardment. `https://www.cefns.nau.edu/geology/malabs/Microprobe/Interact-Effects.html`, 2006. Accessed on 07/02/2020.

[40] Melter Toledo. Dynamic mechanical analysis - poster, 2015.

[41] Alain Jonas. LMAPR2019A - Polymer Science and Engineering A: Physics. 2017.

[42] Michael F. Ashby and David R. H. Jones. *Engineering Materials 2 - An Introduction to Microstructures, Processing and Design*. Elsevier, 3 edition, 2006.

[43] Zhang Yi, Ben Jar P.-Y., Xue Shifeng, and Li Lin. Quantification of strain-induced damagein semi-crystalline polymers: a review. *Journal of Materials Science*, 54:62–82, 2019.

[44] Macobio. `https://uclouvain.be/en/research-institutes/imcn/bsma/macobio.html`, accessed on 8th October 2019.

[45] G Thibaut. *Elaboration et caractérisation de matériaux multiphasiques à base de polylactide (PLA) et de polyhydroxyalcanoates (PHA)*. PhD thesis, 2013.

[46] Sudipta andHoque-Md Enamul Sharif, Ahmedand Mondal. Polylactic acid (pla)-based nanocomposites: Processing and properties. *Bio-based Polymers and Nanocomposites*, pages 233–254, 2019.

[47] M. Arnoult, E. Dargent, and J.F. Mano. Mobile amorphous phase fragility in semi-crystalline polymers: Comparison of PET and PLLA. *Polymer*, 48:1012–1019, 2007.

[48] A. J. Müller, M. Ávila, G. Saenz, and J. Salazar. *RSC Polymer Chemistry Series - Chapter 3 : Crystallization of PLA-based materials*. Number 12. 2015.

[49] Martin Borůvka1 and Luboš Běhálek. Crystallization and thermal degradation of green nanocomposites based on lignin coated cellulose nanocrystals and poly(lactic acid). *Key Engineering Materials*, 737, 2017.

[50] J. Puiggali, Y. Ikada, H. Tsuji, L. Cartier, T. Okihara, and B. Lotz. Epitaxial crystallization and crystalline polymorphism of polylactides. *Polymer*, 41:8921, 2000.

[51] B. Wunderlich. Reversible crystallization and the rigid–amorphous phase in semicrystalline macromolecules. *Progress in Polymer Science*, 28:383–450, 2003.

[52] R. Anderosch and B. Wunderlich. The link between rigid amorphous fraction and crystal perfection in cold-crystallized poly(ethylene terephthalate). *Polymer*, 46:12556–12566, 2005.

[53] J.-M. Raquez, Y. Habibi, M. Murariu, and P. Dubois. Polylactide (pla)-based nanocomposites. *Progress in Polymer Science*, 38:1504–1542, 2013.

[54] Sanghamitra Sen, Shradha Patil, and Dimitris S. Argyropoulos. Thermal properties of lignin in copolymers, blends, and composites: a review. *The Royal Society of Chemistry*, pages 4862–4887, 2015.

[55] Xi-Luan Wang Tong-Qi Yuan Wei Fang, Sheng Yang and Run-Cang Sun. Manufacture and application of lignin-based carbon fibers (lcfs) and lignin-based carbon nanofibers (lcnfs). *The Royal Society of Chemistry - Green Chemistry*, 19:1794–1827, 2017.

[56] Mihai Brebu and Cornelia Vasile. Thermal degradation of lignin - a review. *Cellulose chemistry and technology*, 44:353–363, 2010.

[57] Laura Aliotta, Vito Gigante, Maria Beatrice Coltelli, Patrizia Cinelli, Andrea Lazzeri, and Maurizia Seggiani. Thermo-mechanical properties of PLA/short flax fiber biocomposites. *Applied Sciences (Switzerland)*, 9, 2019.

[58] Sarah Boughouil. *Influence d'un alliage TP/TP sur la ténacité d'une résine époxy*. PhD thesis, Ecole polytechnique de Louvain, Université catholique de Louvain, 2017.

[59] Lancelot de Halleux. *Analyse des propriétés physico-chimiques de résines époxy biosourcées*. PhD thesis, Ecole polytechnique de Louvain, Université catholique de Louvain, 2019.

[60] Jyotishkumar Parameswaranpillai, Nishar Hameed, Jürgen Pionteck, and Eamor M. Woo. *Handbook of EPoxy Blends*. Springer, springer reference edition, 2017.

[61] Bisphenol a. `https://en.wikipedia.org/wiki/Bisphenol_A`. Accessed on 09-02-20.

[62] Sudheer Kumar, Sushanta K Samal, Smita Mohanty, and Sanjay K Nayak. Recent development of biobased epoxy resins: a review. *Polymer-Plastics Technology and Engineering*, 57(3):133–155, 2018.

[63] Fiche technique : Les polymères biodégradables.

[64] J. P. PASCAULT H. SAUTEREAU E. GIRARD – REYDET, V. VICARD. Polyetherimide-modified epoxy networks: Influence of cure conditions on morphology and mechanical properties. *Journal of Applied Polymer Science*, 65, 1997.

[65] J.R. David. *Tensile Testing*. ASM International, second edition, 2004.

[66] Tensile test of polymers, 2015. Budapest University of Technology and Economics, Faculty of Mechanical Engineering, Department of Polymer Engineering.

[67] International Organization for Standardization. *ISO 527-1 : Plastics - Determination of tensile properties - Part 1: General principles*. February 2012.

[68] PerkinElmer. Dynamic mechanical analysis (dma) - a beginner's guide, 2008-2013.

[69] Alan T. Zehnder. *Fracture Mechanics*. 2011.

[70] Boniface J. Tiimob, Vijaya K. Rangari, and Shaik Jeelani. Effect of reinforcement of sustainable $\beta - casio_3$ nanoparticles in bio-based epoxy resin system. *Journal of Applied Polymer Science*, 131:1–10, 2014.

[71] S. Yan, J. Yin, Y. Yang, Z. Dai, J. Ma, and X. Chen. Surface-grafted silica linked with l-lactic acid oligomer: a novel nanofiller to improve the performance of biodegradable poly(l-lactide). *Polymer*, 48:1688–1694, 2007.

[72] X. Wen, K. Zhang, Y. Wang, L. Han, C. Han, and H. et al Zhang. Study of the thermal stabilization mechanism of biodegradable poly(l[U+2010]lactide)/silica nanocomposites. *Polymer International*, 60:202–210, 2011.

[73] K. Oksman, AP. Mathew, D. Bondeson, and I. Kvien. Manufacturing process of cellulose whiskers/polylactic acid nanocomposites. *Composites Science and Technology*, 66:2776–2784, 2006.

[74] M. Jonoobi, J. Harun, AP. Mathew, and K. Oksman. Mechanical properties of cellulose nanofiber (cnf) reinforced polylactic acid (pla) prepared by twin screw extrusion. *Composites Science and Technology*, 70:1742–1747, 2010.

[75] AN. Nakagaito, A. Fujimura, T. Sakai, Y. Hama, and H. Yano. Production of microfibrillated cellulose (mfc)-reinforced polylactic acid (pla) nanocomposites from sheets obtained by a papermaking-like process. *Composites Science and Technology*, 69:1293–1297, 2009.

[76] Jin Huang, Shiyu Fu, and Lin Gan. *Lignin Chemistry and Applications - Chapter 5: Lignin-Modified Thermoplastic Materials*. Elsevier Inc., 2019.

[77] Gordobil O., I. Egüés, R. Llano-Ponte, and J. Labidi. Physicochemical properties of pla - lignin blends. *Polymer Degradation and Stability*, 108:330–338, 2014.

[78] I. Spiridon, K. Leluk, A. M. Resmerita, and R. N. Darie. Evaluation of pla–lignin bioplastics properties before and after accelerated weathering. *Composites: Part B*, 69:342–349, 2015.

[79] J. H. Hodgkin, G. P. Simon, and R. J. Varley. Thermoplastic toughening of epoxy resins: A critical review. *Polymers for Advanced Technologies*, 9:3–10, 1998.

[80] I. K. Partridge C. B. Bucknall. Addition of polyethersulfone to epoxy resins. *British polymer journal*, 15:71–75, 1983.

[81] I. K. Partridge C. B. Bucknall. Phase separation in epoxy resins containing poly- ethersulphone. *Polymer*, 24:634–644, 1983.

[82] P. T. McGrail A. J. MacKinnon, S. D. Jenkins and R. A. Pethrik. Cure and physical properties of thermoplastic modified epoxy resins based on polyethersulfone. *Journal of Applied Polymer Science*, 58:2345–2355, 1995.

[83] A. J. Kinloch R. D. Brooker and A. C. Taylor. The morphology and fracture properties of thermoplastic-toughened epoxy polymers. *The Journal of Adhesion*, 86:726–741, 2010.

[84] C. B. Bucknall and A. H. Gilbert. Toughening tetrafunctional epoxy resins using polyetherimide. *Polymer*, 30:213–217, 1989.

[85] Ooishi K. Yoshiki T. Saitoo M. Watanabe O. Murakami A., Saunders D. and Takezawa M. Fracture-behavior of thermoplastic modified epoxy resins. *The Journal of Adhesion*, 39:227–242, 1992.

[86] Nagpal A. Kandpal J., Yadaw S.B. Mechanical properties of multifunctional epoxy resin/glass fiber reinforced composites modified with poly(etherimide). *Advanced Materials*, 4:241–249, 2013.

[87] Swiss-compagny. Fiche de données de sécurité sr infugreen 810. `https://www.swiss-composite.ch/pdf/s-sicomin-sr-infugreen-810-f.pdf`, 2018. Accessed on 27/01/2020.

[88] Wikipedia. Extrusion. `https://fr.wikipedia.org/wiki/Extrusion`. Accessed on 24/11/2019.

[89] Wikipedia. Injection moulding. `https://en.wikipedia.org/wiki/Injection_moulding`. Accessed on 24/11/2019.

[90] Michael E. Brown. *Introduction to Thermal Analysis: Techniques and Applications*. Kluwer Academic Publishers, 2001.

[91] Wikipedia. Tensile testing. `https://en.wikipedia.org/wiki/Tensile_testing`. Accessed on 12-02-20.

[92] Dhanya Moorkoth and Kesavan Madhavan Nampoothiri. Production and characterization of polyhydroxy butyrate-co-valerate (phbv) by a novel halotolerant mangrove isolate. *Bioresource Technology*, 2015.

[93] J.P. Mofokenga and A.S. Luyt. Dynamic mechanical properties of pla/phbv, pla/pcl, phbv/pcl blends and their nanocomposites with tio_2 as nanofille. *Thermochimica Acta*, 613:41–53, 2015.

[94] Polymer additives and mechanical properties, 2003.

[95] Anne Serine Ognedal. Large-deformation behaviour of thermoplastics at various stress states. 2012.

[96] Steven Nahm. Use of dynamic mechanical analysis in thermoset resin development (for composites applications). 2001.

[97] Glenn Sime. A closer look: Techniques for obtaining glass transition temperature of polymeric materials, 2013.

[98] Kevin P. Menard. *DYNAMIC MECHANICAL ANALYSIS - A Practical Introduction*. CRC Press LLC, 1999.

[99] Michael F. Ashby. *Materials Selection in Mechanical Design*. Elsevier, 2011.

[100] Maria Raimo. Growth of spherulites: foundation of the dsc analysis of solidification. *ChemTexts*, 2015.

[101] Gránásy László, Pusztai Tamás, Tegze György, Warren James A., and Douglas Jack F. Growth and form of spherulites. *Physical review*, 72, 2005.

[102] Current progress on bio-based polymers and their future trends. *Progress in Biomaterials*, 2(1):8, 2013.

[103] Maurizio Avella, Aleksandra Buzarovska, Maria Emanuela Errico, Gennaro Gentile, and Anita Grozdanov. Eco-challenges of bio-based polymer composites. *Materials*, 2(3):911–925, 2009.

[104] Clement Gourier. *Contribution à l'étude de matériaux biocomposites à matrice thermoplastique polyamide-11 et renforcés par des fibres de lin*. PhD thesis, Université de Bretagne Sud, 2016.

[105] INRS. Plastiques , Risque et Analyse ThermIQue - Polyamide 11.

[106] Plastiques Biosourcés : Étude De Leur Performance Environnementale Comparativement Aux Plastiques Pétrochimiques. page 111, 2013.

[107] József Karger-Kocsis, Ákos Kmetty, László Lendvai, Stavros X. Drakopoulos, and Tamás Bárány. Water-assisted production of thermoplastic nanocomposites: A review. *Materials*, 8:72–95, 2015.

[108] Mohamed Habib Mohamedou Isselmou. Applications des méthodes de l ' analyse thermique à l ' étude du vieillissement des polymères Mohamedou Isselmou Mohamed Habib To cite this version : HAL Id : tel-01544592. page 217, 2017.

[109] Abderrahim Boudenne, Laurent Ibos, Yves Candau, and Sabu Thomas. *Handbook of Multiphase Polymer Systems*, volume 1. John Wiley & Sons, 2011.

[110] Magdalena Urbaniak and Karol Grudziñski. Time-temperature-transformation (TTT) cure diagram for EPY ® epoxy system. 2007.

[111] Naïma Sallem-Idrissi, Michel Sclavons, and Jacques Devaux. Synthesis of polymer nanocomposites by water-assisted extrusion. *Synthesis Techniques for Polymer Nanocomposites*, pages 179–210, 2014.

[112] B. Lecouvet, M. Sclavons, S. Bourbigot, J. Devaux, and C. Bailly. Water-assisted extrusion as a novel processing route to prepare polypropylene/halloysite nanotube nanocomposites: Structure and properties. *Polymer*, 52:4284–4295, 2011.

[113] L. H. Sperling. *Introduction to physical polymer science*, volume 78. John Wiley & Sons, fourth edi edition, 2006.

[114] Naeun Lee and Sangmook Lee. Water-assisted extrusion of bio-based PETG/clay nanocomposites. *Korea Australia Rheology Journal*, 30:47–53, 2018.

[115] J. W. Barlow. Polymer blends and alloys. *Makromolekulare Chemie. Macromolecular Symposia*, 70-71(1), 1993.

[116] Dimitri D.J. Rousseaux, Naïma Sallem-Idrissi, Anne Christine Baudouin, Jacques Devaux, Pierre Godard, Jacqueline Marchand-Brynaert, and Michel Sclavons. Water-assisted extrusion of polypropylene/clay nanocomposites: A comprehensive study. *Polymer*, 52:443–451, 2011.

[117] G. Stoclet, M. Sclavons, B. Lecouvet, J. Devaux, P. Van Velthem, A. Boborodea, S. Bourbigot, and N. Sallem-Idrissi. Elaboration of poly(lactic acid)/halloysite nanocomposites by means of water assisted extrusion: Structure, mechanical properties and fire performance. *RSC Advances*, 4(101):57553–57563, 2014.

[118] Makara Lay, Nuur Laila Najwa Thajudin, Zuratul Ain Abdul Hamid, Arjulizan Rusli, Muhammad Khalil Abdullah, and Raa Khimi Shuib. Comparison of physical and mechanical properties of pla, abs and nylon 6 fabricated using fused deposition modeling and injection molding. *Composites Part B: Engineering*, 176(August):107341, 2019.

[119] Julien Arbellini, Sébastien Jean-Louis, and Milino Sébatien Kerowgodage. L'acide Polylactique : PLA. 2017.

[120] Ramesh P Babu, Kevin O'Connor, and Ramakrishna Seeram. Current progress on bio-based polymers and their future trends. *Progress in Biomaterials*, 2(1):8, 2013.

[121] Justin B. Hooper and Kenneth S. Schweizer. Theory of phase separation in polymer nanocomposites. *Macromolecules*, 39(15):5133–5142, 2006.

[122] Penwarat Sennan and Jantrawan Pumchusak. Improvement of mechanical properties of poly(lactic acid) by elastomer. *Malaysian Journal of Analytical Sciences*, 18(3):669–675, 2014.

[123] Department of Polymer Engineering. Tensile Test of Polymers. *Tensile Test of Polymers*, (February):1–9, 2015.

[124] Helmut Fahrenholz. The 2012 version of ISO 527 Plastics : Determination of tensile properties Zwick/Roell. (October), 2018.

[125] Enic Quero, Alejandro J. Müller, Francesca Signori, Maria Beatrice Coltelli, and Simona Bronco. Isothermal cold-crystallization of PLA/PBAT blends with and without the addition of acetyl tributyl citrate. *Macromolecular Chemistry and Physics*, 213(1):36–48, 2012.

[126] Seyedmohammadkazem Fehri, Patrizia Cinelli, Maria-Beatrice Coltelli, Irene Anguillesi, and Andrea Lazzeri. Thermal Properties of Plasticized Poly (Lactic Acid) (PLA) Containing Nucleating Agent. *International Journal of Chemical Engineering and Applications*, 7(2):85–88, 2016.

[127] Process Details. Ingeo ™ Biopolymer 4060D Technical Data Sheet For Heat Seal Layer in Coextruded Oriented Film. 201:1–4, 2005.

[128] Extrusion Applications. Ingeo ™ Biopolymer 2500HP Technical Data Sheet. (4):1–5.

[129] Jean-Luc Wertz. Polymères biobasés : amidon, PLA, PHA, PE et PET. (1):1–54, 2016.

[130] C. Schick. Differential scanning calorimetry (DSC) of semicrystalline polymers. *Analytical and Bioanalytical Chemistry*, 395(6):1589–1611, 2009.

[131] Waël Ballout, B. Coulon, Y.-A. Janssens, Pascal Van Velthem, M. Sclavons, Denis Magnin, Thomas Pardoen, and Christian Bailly. Quantitative Characterization of Interdiffusion at the Resin-Resin and Resin-Prepreg Interphases of Epoxy Systems Processed by Model SQ-RTM. *Polymer Engineering & Science*, 47:21–25, 2016.

[132] Amir Bahrami, François Cordenier, Pascal Van Velthem, Waël Ballout, Thomas Pardoen, Bernard Nysten, and Christian Bailly. Synergistic local toughening of high performance epoxy-matrix composites using blended block copolymer-thermoplastic thin films. *Composites Part A: Applied Science and Manufacturing, Elsevier*, 2016.

[133] P. Van Velthem, W. Ballout, D. Daoust, M. Sclavons, F. Cordenier, E. Henry, D. Dumont, V. Destoop, T. Pardoen, and C. Bailly. Influence of thermoplastic diffusion on morphology gradient and on delamination toughness of RTM-manufactured composites. *Composites Part A: Applied Science and Manufacturing*, 72:175–183, 2015.

[134] P. Van Velthem, W. Ballout, J. Horion, Y. A. Janssens, V. Destoop, T. Pardoen, and C. Bailly. Morphology and fracture properties of toughened highly crosslinked epoxy composites: A comparative study between high and low Tg tougheners. *Composites Part B: Engineering*, 101:14–20, 2016.

[135] W. Ballout, P. Van Velthem, D. Magnin, E. Henry, M. Sclavons, T. Pardoen, and C. Bailly. Specific influence of polyethersulfone functionalization on the delamination toughness of modified carbon fiber reinforced polymer processed by resin transfer molding. *Polymer Engineering and Science*, 59(5):996–1009, 2019.

[136] P. Van Velthem, W. Ballout, D. Dumont, D. Daoust, M. Sclavons, F. Cordenier, T. Pardoen, J. Devaux, and C. Bailly. Phenoxy nanocomposite carriers for delivery of nanofillers in epoxy matrix for resin transfer molding (RTM)-manufactured composites. *Composites Part A: Applied Science and Manufacturing*, 76:82–91, 2015.

[137] João ítalo Lopes Amaro. *Study and Optimisation of Flax Fibers Reinforced Bio-Sourced Epoxy Resin Composites Interfacial Adhesion and Compatibility*. PhD thesis, Ecole polytechnique de Louvain, Université catholique de Louvain, 2019.

[138] James E. Mark. *Physical Properties of Polymers Handbook*, volume 199. Springer, second edi edition, 2006.

[139] Edwin Klompen. *Mechanical properties of solid polymers : constitutive modelling of long and short term behaviour*. PhD thesis, Technische Universiteit Eindhoven, 2005.

[140] Maximilian. Lackner. *Bioplastics - Biobased plastics as renewable and/or biodegradable alternatives to petroplastics*. 2015.

[141] Jeffrey Gotro. Characterization of thermosets part 20: Tensile testing part one. `https://polymerinnovationblog.com/characterization-thermosets-part-20-tensile-testing-part-one/`, 2017. Accessed on 12-02-20.

[142] S. Chaudhary, S. Parthasarathy, D. Kumar, C. Rajagopal, and P. Roy. Simple toughening of epoxy thermosets by preformed thermoplastics. *Society of plastics engineers*, pages 1–3, 2014.

[143] GreenValue Enterprises LLC.

UNIVERSITÉ CATHOLIQUE DE LOUVAIN
École polytechnique de Louvain
Rue Archimède, 1 bte L6.11.01, 1348 Louvain-la-Neuve, Belgique | **www.uclouvain.be/epl**